2004-03-02

Mechanical Behavior Analysis of a Carbon-Carbon Composite for Use in a Polymer Electrolyte Fuel Cell

Dara S. Flynn
Worcester Polytechnic Institute

Table of Contents

List of Figures

List of Tables

Introduction

The focus of this project is the mechanical behavior of a carbon – carbon composite layer for use in Proton Exchange Membrane (PEM) fuel cells. Specified stack geometries and a range of pressures for a one cell setup will be the scope of this testing. Carbon – carbon composites are used as gas diffusion layers in PEM fuel cells. These layers serve three main purposes; deliver anode and cathode gases to the reaction sites, deliver waste products out of the reaction area, and conduct electrons.

Much electrochemical and thermodynamic data has been researched and collected but mechanical properties have been mostly overlooked. Mechanical properties of these layers will have a large impact on overall performance due to contact areas, void composition, breakage of layers, and deformation of layers. The goal of this project is to obtain data concerning mechanical properties of a fuel cell setup. Data will be collected in the form of impingement of the gas diffusion materials into the gas flow channels, thicknesses of gas diffusion layer – membrane electrode assembly setups, and bipolar plate thicknesses. Microstructural characterization will assist in characterizing gas diffusion layers in these setups.

Literature Research

Fuel Cell Technology

The first fuel cell was invented in 1839 by a man named William Grove. Current technology includes hydrogen fueled and metal fueled fuel cells. Six types of hydrogen fuel cells exist today; Alkaline Fuel Cells (AFC), Proton Exchange Membrane Fuel Cells (PEMFC), Direct Methanol Fuel Cells (DMFC), Phosphoric Acid Fuel Cells (PAFC), Molten Carbonate Fuel Cells (MCFC), and Solid Oxide Fuel Cells (SOFC). Metal fuel cell technology replaces hydrogen with a metal, such as zinc, as the power source. This research focuses on Proton Exchange Membrane Fuel Cell technology and Solid Oxide Fuel Cell technology.

Fuel cells are galvanic cells that take advantage of the reduction and oxidation reactions to produce electrical power. The anode reaction is either oxidation of hydrogen or methanol; the cathode reaction is an oxygen reduction reaction. Hydrogen is split into two positive hydrogen ions (H^+) and two electrons (e^-) by the anode catalyst. H^+ ions travel through the electrolyte material to the cathode while the electrons are forced through a specified path in which electrical energy is harnessed. At the cathode oxygen molecules are broken apart into oxygen ions (O^{2-}) and then combined with the H^+ and the electrons to form water. Water is the waste product of these fuel cells. Figure 1 depicts a general fuel cell configuration.

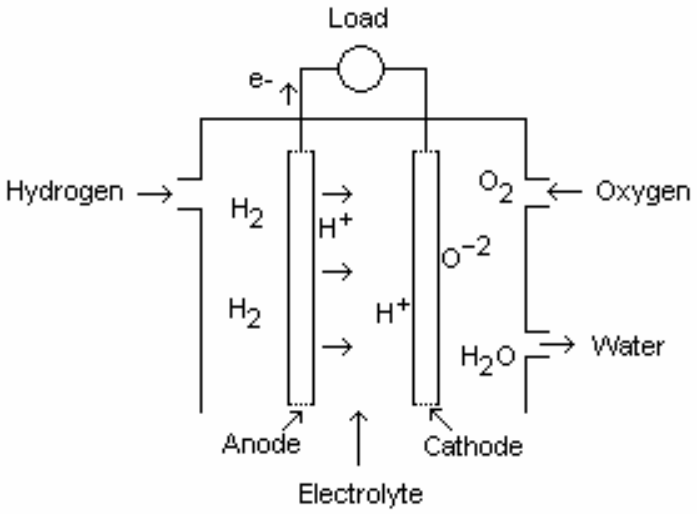

Figure 1: General Fuel Cell Configuration.

Only half of the current fuel cells utilize H^+ ions as the charge carrier in the electrolyte. OH^-, CO_3^{2-}, and O^{2-} are also used as charge carriers in AFC, MCFC, and SOFC technologies respectively. Each type of cell has a specific range of operating temperatures. Low temperature fuel cells are the AFC, PEMFC, DMFC, and PAFC. These operate between 60ºC and 220ºC. High temperature fuel cells are the MCFC and SOFC operating between 600ºC and 1000ºC. Power generation varies from 5 kilowatts to 11 megawatts depending on the type of fuel cell and the size of the configuration. Each type of fuel cell has been developed for use in different industries. For instance AFCs, PEMFCs, and DMFCs have been pushed towards usage in space exploration, energy storage and military applications while PAFCs, MCFCs, and SOFCs have been pushed towards combined heating and power generation units (Carrette, Friedrich, Stimming 10).

Fuel Cell Designs

The most common fuel cell design for PEM fuel cells is a stack structure. The stack consists of layers of sandwich – like structures referred to as cells. Cells consist of five basic layers:

- a plate
- the anode
- the electrolyte
- the cathode
- another plate.

Metal plates act as flow channels, electrical conductors, and structural components. These plates are shaped such that they contain channels for gas flow and waste flow through the cell. Electrodes contain the catalyst for oxidation and reduction. The electrolyte acts as an ion conductor between electrodes. Some designs incorporate the GDL into the anode and cathode layers while others have a separate layer for gas diffusion. Another variation is to incorporate the anode and cathode layers into the electrolyte layer and have separate layers for gas diffusion. Gas flows can be one of three different configurations, co-flow, counter-flow, or cross-flow. Co-flow is gas flow in the same direction for both anode and cathode gasses. Counter-flow is defined as gas flow that is rotated 180 degrees relative to each stream. Cross-flow is defined as gas flow that is rotated 90 degrees relative to each stream. Different gas flow configurations will give different channel configurations. Cells also have configurations unique to the type of fuel cell. One cell does not produce enough power to be usable on a large scale so individual cells are stacked in series to produce a usable amount of energy. Some stacks use plates that are monopolar while others use plates that

are bipolar (Carrette, Friedrich, Stimming 26). Larminie and Dicks or Hoogers provide thorough descriptions of cell and stack designs.

Electrolyte material can be made from an ion conducting polymer, a solid oxide, a carbonate salt, phosphoric acid, or aqueous potassium hydroxide. Most of the specifics of these materials are restricted to proprietary information. In PEM fuel cells the electrolyte is made from an ion conducting polymer formed into a thin pliable sheet, referred to as a membrane. These membranes are usually made of a sulphonated flouropolymer material such as fluoroethelyne, known widely by the brand name Nafion (made by Dupont). The flouroethelyne structure usually used is polytetraflouroethelyne also known as PTFE. The structure of PTFE is shown in Figure # below.

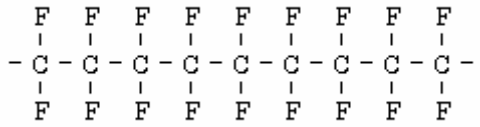

Figure 2: Chemical Structure of Polytetraflouroethelyne (PTFE).

To be used as an ion conductor this polymer chain is sulphonated and the structure becomes something similar to Figure #. Sulphonation can result in different molecular structures other than the one shown from different processing methods. Actual sulphonated polymer structures are kept as proprietary information in most cases. This structure is also referred to as perflourosulphonic acid PTFE coplymer.

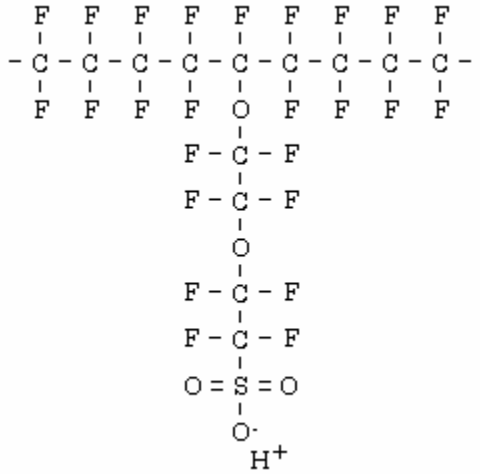

Figure 3: Sulphonated Flouroethelyne.

According to Larminie and Dicks the HSO_3 group is ionically bonded so the end of the chain is actually an SO_3^- ion. Thus a strong mutual attraction from the opposite ions of each molecule occurs resulting in a

clustering effect from the side chain molecules. Sulphonic acid is highly hydrophyllic while flouroethelyne is highly hydrophobic. This produces a molecule that is generally hydrophobic with hydrophyllic regions throughout. In use this creates pockets of water within the material which hydrogen ions can easily move through.

Gas diffusion media can vary in composition as well as microstructure. Some designs use gas diffusion media that is made of spherical particles of a polymer backed with a carbon composite, such as poly-tetrafluoroethelyne (PTFE), or simply a porous fiber composite such as carbon fiber paper. In a PTFE layer the spherical particles hold the catalysts for the cell and are backed with a carbon fiber paper for support (Carrette, Friedrich, Stimming 13). PTFE spheres must also allow for gas diffusion to the catalyst particles thus the overall material must have a very porous structure. Carbon fiber papers can vary in microstructure from a very ordered weave type structure to a randomly oriented fiber structure. Carbon fiber papers utilized in PEM fuel cell technology usually have a randomly oriented fiber structure in a carbon matrix. This structure allows for more porosity as compared to the ordered weave structure.

Proton Exchange Membrane Fuel Cells

A Proton Exchange Membrane Fuel Cell (PEMFC) is also known as a polymer electrolyte fuel cell. These fuel cells have platinum anode and cathode materials and utilize a polymer electrolyte. The operating temperatures are between 60ºC and 100ºC (Carrette, Friedrich, Stimming 11). The electrodes are usually porous gas diffusion layers (GDL) made out of a carbon fiber paper (CFP) or cloth imbedded with the catalyst material. Some systems utilize a gas diffusion layer without the catalyst particles contained within. The production methods of this layer are very delicate and have to be very precise to ensure proper function. The proton conducting polymer membrane, as discussed above, is a composite of polymers usually perflourocarbonic sulfonic acid membranes with polytetraflouroethylene (PTFE) (Carrette, Friedrich, Stimming 12).

Setup of PEM fuel cells consists of metal bipolar or monopolar plates surrounding gas diffusion layers, the anode and cathode materials, and the ion conducting membrane. The containment layer backs the first and last cells in the stack configuration. This layer is to provide protection for the stack from any contaminants. Figure # shows a common polymer electrolyte fuel cell setup.

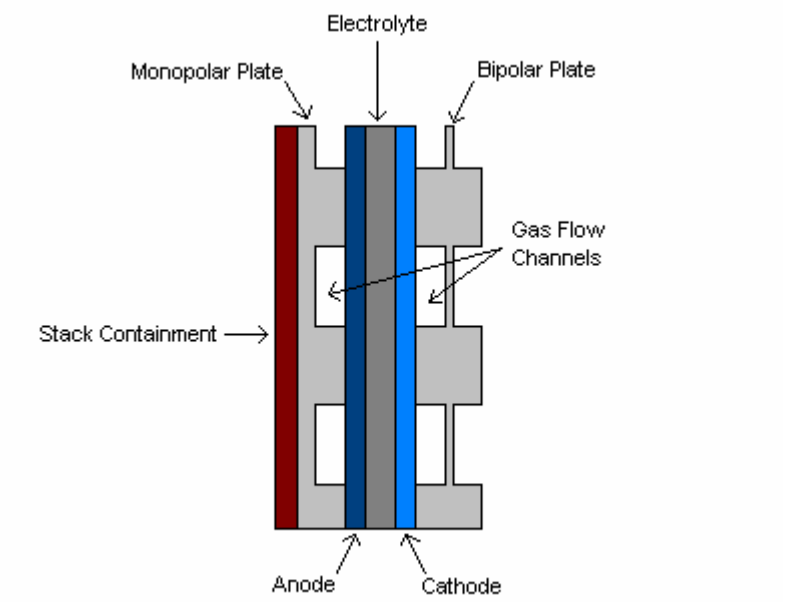

Figure 4: Polymer Electrolyte Configuration.

PEM fuel cells follow the oxidation and reduction reactions with hydrogen and oxygen. At the anode hydrogen in the form of H_2 is broken into H^+ ions and electrons according to

$$H_2 = 2H^+ + 2e^-.$$

Electrons follow the load path, across the bipolar plates, to the cathode and ions are conducted through the electrolyte to the cathode. Oxygen is delivered to the cathode in the form of O_2, which combines with the hydrogen ions and the electrons to form H_2O according to

$$O_2 + 4H^+ + 4e^- = 2H_2O.$$

Some problems with this type of fuel cell are water management, hydrogen management, and carbon monoxide poisoning of the catalyst. Carbon monoxide poisoning occurs when CO molecules are absorbed onto the active sites of the platinum. CO can be removed by converting to CO_2 which releases the molecules from the active sites. A reformer is often connected to this type of fuel cell to convert the liquid methane, or other raw fuel, into usable hydrogen. CO is released when the raw fuel is converted to hydrogen gas. The CO released in the reformer can be converted to CO_2 by adding steam to the gas mixture before it reaches the fuel cell stack.

Carbon

According to Kinoshita carbon is found in many forms such as carbon blacks, graphite, active carbon, glassy carbon, carbon fibers, and diamond. Processing of carbon into the many forms varies depending on the type of carbon being made and the desired material properties of the final product. Some precursors commonly used to produce carbon materials are rayon, polyacrylonitrile (PAN), hydrocarbons, petroleum coke, furfuryl alcohol resin, or phenol formaldehyde resin.

The microstructure of carbon can be either diamond, graphite, or amorphous. Diamond has a cubic crystal structure with 4 tetrahedral sites filled; two tetrahedral sites on opposite diagonals.

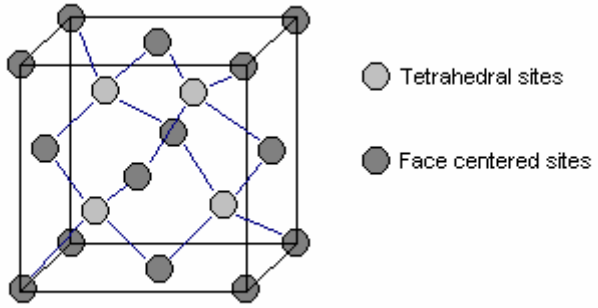

Figure 5: Diamond Crystal Structure.

Graphite is a hexagonal form of carbon. According to Kinoshita carbon spacing within the hexagonal planes is 1.42Å, interplanar spacing is 3.354Å, electrical resistivity in the planes is 10^{-4} Ω-cm, and electrical resistivity in the perpendicular direction is 10^{-2} Ω-cm. Covalent bonding is found in the hexagonal planes but only van der Waals bonding is found between layers. This attests for the electromechanical properties of graphite.

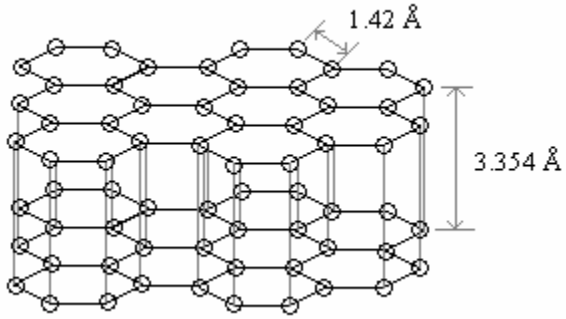

Figure 6: Graphite Crystal Structure.

Amorphous carbon is considered to have regions of hexagonal planes surrounded by unordered regions. A range of amorphous carbon can be made depending on processing and treatments (Kinoshita 23).

Carbon blacks are commonly found as either spherical particles or interlinked in a chainlike structure. Microstructure can be diamond, graphite, or amorphous. Blacks are usually incorporated into other materials to create usable electrochemical devices or enhance electrochemical properties. Processes to make carbon blacks are the channel process, oil furnace process, or the thermal process. Sizes and shapes of carbon blacks depend on the processing method and processing parameters. Particle sizes can range from 100Å to 800Å with corresponding surface areas of less than $10m^2/g$ to over $500m^2/g$ (Kinoshita 6). Active carbons are defined as high surface area, high porosity carbon produced by thermal activation or chemical activation. Raw materials include sawdust, coconut shells, and black ash among others.

Glassy carbon is typically a hard solid carbon (Kinoshita 6) . It has a black glassy look and it shows fracture behavior similar to that of actual glasses. It is manufactured by thermal degredation of selected organic polymers. Physical properties of the piece depend on the maximum temperature of heat treatment during fabrication, which is typically in the 1800°C range. This type of fabrication will produce a piece with extremely low permeability to gasses with a low density due to a significant volume of closed pores. Microstructure consists of long, randomly oriented, intertwined microfibrils. Mechanical properties compared to graphite are as such: tensile and compressive strengths are typically higher, electrical resistivity is higher, thermal conductivity is lower, and the coefficient of thermal expansion is comparable.

Carbon Fibers

Carbon fibers are a different form of carbon from any mentioned above. Carbon fibers are used for supports for composites, including tennis rackets and golf clubs, structural components in aircrafts, and drive shafts, pushrods, and hinges for the automotive industry. Carbon fibers are also used in the electrochemical industry in carbon – carbon composites for gas diffusion layers, as plain carbon fibers for electrodes, and as structural components for electrodes in batteries and fuel cells.

Carbon fibers are fabricated using a number of different methods and precursors. Precursors include polyacrylonitrile (PAN), petroleum pitch, and mesophase pitch. Methods include melt spinning and vapor deposition growth. According to Buckley and Edie 90% of all commercial carbon fibers are

produced from a PAN precursor. Commercially produced continuous fibers are produced in tows or yarns. Yarns are twisted bundles of continuous fibers and tows are untwisted bundles of continuous fibers (Chung 10). Microstructures of fibers differ depending on the precursor used and the processing methods. Microstructural configuration can affect mechanical properties of fibers also. Commercial carbon fibers are placed into three main categories, general purpose fibers, high performance fibers, and activated carbon fibers. General purpose fibers have an amorphous and isotropic structure, low tensile strength, low modulus, and low cost. High performance fibers have high strength and modulus and activated carbon fibers have a large number of open micropores that act as absorption sites (Chung 5).

Acrylic precursors in the form of polyacrylonitrile (PAN) are polymers containing a predominant amount of the monomer acrylonitrile (C_3H_3N) (Peebles 7). Figure # shows the structure of an acrylonitrile monomer.

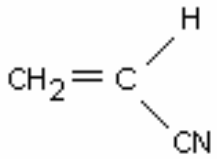

Figure 7: Acrylonitrile Monomer.

PAN is copolymerized with a small amount of other monomer to lower the glass transition temperature of the material. Some monomers used are acrylic acid, itaconic acid, methyacrylic acid, methyl acrylate, and vinyl acetate. A polymer solution of about 15 to 30 weight percent monomer to 85 to 70 weight percent PAN is used in solution spinning. The polymer mixture is heated until it forms a fluid like substance that can be pushed through a spinneret. The fluid like solution exits the spinneret into a hot gas environment or a coagulation bath. A coagulant helps to extract the solvent from the polymer, while a hot gas environment helps the solvent to evaporate (Buckley and Edie 21). According to Buckley and Edie, "the rate at which the solvent is extracted from the polymer as it passes through the coagulation bath governs the final cross-sectional shape of the fiber". Rapid extraction of the solvent results in a kidney bean or dog bone shape due to the different solidification rates of the inner and outer portions of the fiber. Circular cross-sections can be achieved by controlling the rate of solvent extraction or evaporation. The next step is to stretch the fibers to align the polymer chains and ultimately the carbon microstructure (Buckley and Edie 22).

Mesophase pitch precursor fibers have some advantages over PAN based fibers. The largest advantages include; high availability of the material, low cost for raw pitch, a closer initial structure to graphite which leads to less processing for a similar output, and mesophase pitch contains less non-carbon elements than PAN which leads to a higher percentage yield. Mesophase pitch fibers are produced by thermal or catalytic polymerization of petroleum or coal tar pitch (Buckley and Edie 27). The thermal process includes heating raw pitch to about 400 to 450°C for approximately 40 hours. During this time about 45 to 60 percent will transform from an isotropic material to a mesophase or liquid crystal. Catalytic polymerization consists of using solvents to extract some isotropic material. Insolubles can be converted to anisotropic pitch by heating to 230 to 400°C for less than 10 minutes. The anisotropic phase is stacked polynuclear hydrocarbons that are disc shaped with an average molecular weight of about 1000. Upon heating small spheres of mesophase form and grow to the point of collision to create a nematic liquid crystal structure. Mesophase precursors soften over a range of temperatures and orient under an applied stress. Mesophase products used for melt spinning are comprised of high molecular weight molecules with a small number of side groups present. Molecules with no side groups present will tend to melt instead of becoming liquid enough to flow (Buckley and Edie 28).

Melt spinning of Mesophase pitch consists of melting, extrusion, and quenching. Precursor material is melted and filtered of solid objects then forced through a spinneret into air and wound up. An initial orientation takes place as the material exits the spinneret, combined with the winding process this produces a highly oriented fiber. Fiber diameters can vary if the temperature of the spinneret is not carefully controlled; a ±3.5°C change in temperature can change the diameter ±15% (Buckley and Edie 28).

After spinning, from either precursor, the fibers go through an oxidation process. Pan based fibers go through oxidation to secure the molecular orientation and maximize the mechanical properties of the fibers. Pitch based fibers undergo oxidation because they are otherwise uninfusable. PAN oxidation occurs in a temperature range of 220 to 270 °C under tension for 30 minutes to 7 hours. Time and temperature depends on the composition and diameter of the precursor fiber. Primary reactions that occur are cyclization of the nitrile groups, dehydration of saturated carbon-carbon bonds, and oxidation. Mesophase precursor fibers are oxidized at 300°C for 30 minutes to 2 hours (Buckley and Edie 31). After oxidation the fibers go through the carbonization or graphitization process. During carbonization the fibers

are heated in an inert atmosphere to temperatures that range from 1000 to 2800°C (Buckley and Edie 25). Carbonization drives off most of the non-carbon elements leaving a fiber that is almost pure carbon. Graphitization is a process that starts with the carbonized fiber and forms a carbon fiber that is mostly graphite. This process consists of heat treating in an inert atmosphere to temperatures ranging from 2500 to 3000°C (Chung 23). The level of graphitization depends on the time and temperature of the graphitization heat treatment. Another secondary operation done before fiber use is sizing. Sizing is done to improve handle-ability and could enhance the bonds between fibers or fiber and matrix.

Carbon fibers can also be fabricated using a vapor growth process. This process is used to create only short, discontinuous fibers. A catalyst is placed in a heated hydrocarbon atmosphere to grow carbon filaments, diameter as small as 0.1μm, which then grow into fibers. A common catalyst is a solid iron particle. The hydrocarbons used are usually low molecular weight compounds such as acetylene. With the correct carbon potential in the chamber fiber can grow to be as large as 10μm in diameter (Buckley and Edie 33, Chung 9).

Microstructure of carbon fibers can range from completely graphitic to completely amorphous. Important aspects that effect material properties are, degree of crystallinity, interlayer spacing, coherent lengths parallel and perpendicular to the layers, any preferred orientation of the layers, curvature of the layers, domain structure, and volume fraction, spacing, and shape of microvoids. High tensile modulus, low electrical resistivity, and high thermal conductivity are typical of a high degree of crystallinity, low interlayer spacing, large crystallite size, strong parallel texture, and low density of defects in the fiber. Fibers with a high tensile strength usually contain a weak perpendicular texture, small layer curvature values, large perpendicular coherent lengths, and a small amount of defects. A number of correlations can be drawn between heat treat temperature and microstructural properties (Chung 55). More information pertaining to the relationship between processing and microstructure of fibers can be found in the writings of Chung or Buckley and Edie.

Microstructures of fibers differ depending on the processing method and precursor used. PAN based fibers have a macrostructure that is fibrillar, this consists of ribbon like undulations that are highest in the center and lowest in the surface, therefore modulus of these fibers varies with depth into the fiber. Layer planes of PAN based carbon fibers have no regular three dimensional order. Skin regions and layer

planes that are roughly parallel to the surface show needle shaped voids between crystallites while folded regions found near the core have angles around 180 degrees. Average crystallite thickness is 6.2 nm and average layer spacing was 0.3434 nm in the 002 crystallographic direction. PAN based carbon fibers are comprised of extensively folded and interlinked turbostratic layers with an interlinking spacing considerably larger than true graphite (Buckley and Edie 47).

Pitch based fibers can show a variety of microstructures depending on the spinning conditions. Preferred microstructures are random, flat layers, or radial structures. Flat layers and radial structures are shown as large flat plates extending down the fiber axis arranged in a geometric order across the cross section. The random microstructure has small flat plates oriented parallel to the fiber axis but randomly distributed in the cross section (Buckley and Edie 48).

Carbon – Carbon Composites

Carbon – carbon composites consist of carbon fibers in a carbon matrix. According to Buckley and Edie "carbon – carbon composites are fabricated by infiltrating a carbon precursor into a preform of carbon fibers". Carbon matrices are derived from similar precursor materials as the fibers themselves, pitch, resin, or a carbonaceous gas. Fabrication of carbon – carbon composites can be one of four methods; liquid phase impregnation, hot isostatic pressure impregnation carbonization, hot pressing, or chemical vapor infiltration. The first step in the first three processes includes preparation of a prepeg, wet winding continuous fibers with pitch or resin or wetting woven fibers with pitch or resin. The next step is pyrolization or carbonization. This includes heating the wet fibers to 350 to 850°C. Matrix material shrinks substantially during heat treatment and thus more is added to compensate for this loss during processing. This also creates pores and cracks in the structure; the rate of shrinkage has a large impact on the density of these defects. Differences in thermal expansion also create internal stresses and stress cracks throughout the composite. After the carbonization process more precursor material is forced into the composite using vacuum impregnation or some other technique, until the desired density is obtained. This step can be repeated up to six times to reach the density desired.

According to Chung the chemical vapor deposition processes include impregnation of carbon by a gas phase hydrocarbon and then heat treatment at temperatures in the range of 700 to 2000°C. The mechanism for deposition of carbon is cracking of the gas which deposits pyrolytic carbon in the open

pores and surface of the preform. There are three different methods for this type of process; isothermal, temperature gradient, and pressure gradient methods. Carbon fiber preforms are either carbonized or graphitized carbon fabric prepegs or dry wound carbon fibers. In the isothermal method "the gas and sample are kept at a uniform temperature" (Chung 152). The temperature gradient methods uses an induction furnace and the sample is supported by an inductively heated susceptor so the inside surface of the sample will be at a higher temperature than the outside surface of the sample. This temperature gradient causes the deposition to occur on the inside surface first. The pressure gradient method consists of hydrocarbon gas impinging on the inside surface of the sample so the gas pressure is higher at the inside surface than the outside surface. Thermal gradient and pressure gradient methods can only process one sample at a time while the isothermal method can process several samples at once (Chung 152).

The quality of the finished composite depends on the quality of the precursor as well as the initial carbon fiber used. For instance pitch based material can bubble during carbonization and lead to expulsion of matrix material, polymer based material can pool and cause excessive shrinkage in the area of pooling. Highly graphitized fibers are preferred because their thermal stability reduces part warpage during processing. Circular diameter fibers are preferred over non-circular fibers because there are fewer stress points in the matrix associated with circular diameter fibers. Microcrack initiation is more likely to occur at a fiber corner, if there are no corners then fewer microcracks will appear (Chung 154).

Oxidation is a very large problem with carbon – carbon composites. Oxidation can take place at a very low oxygen partial pressure because the reaction in air is:

$$C + O_2 \rightarrow CO_2$$

and this reaction has a very negative free energy associated with it. Oxidation starts first at the fiber – matrix interfaces which weakens the fiber bundles and causes the unoxidized material to fail catastrophically.

Methods

Compression properties and microstructural characterization of the carbon fiber paper were obtained using optical microscopy and scanning electron microscopy. Microstructural characteristics were found using unaltered carbon fiber paper and also hot mounted carbon fiber paper. Four pressure levels were used to determine compression characteristics, 100, 200, 300, and 400psi. Preliminary testing was done using 400psi and this was found to be too great a pressure, thus 400psi was dropped from further testing.

Bipolar plates, carbon fiber paper, and electrolyte material were cut into rectangular pieces having dimensions of 0.57 x 1.25 inches, 0.7125in^2 (1.4478 x 3.175 cm, 4.5968 cm^2). Bipolar plates were cut with a 0.0015 inch thick aluminum oxide blade on a bench top cutting wheel; gas diffusion layer (GDL) and membrane electrode assembly (MEA) materials were cut using a razor blade. Three sample configurations were studied in a one cell setup. These sample configurations utilized different sections of the bipolar plates to simulate actual cell reactions in a fuel cell stack. Table 1 is a summary of the sample configurations.

Table 1: Sample Configurations.

Configuration Number	Bipolar plate configuration
1	parallel aligned channels
2	perpendicular channels
3	offset parallel channels

Sample configuration 1 is a parallel channel arrangement. Bipolar plates in this configuration are aligned such that gas flow channels (GFC) run parallel to each other. Samples were aligned as closely to actual plate alignment as possible.

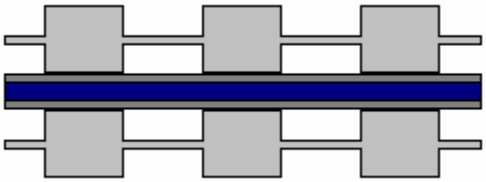

Figure 8: Sample Configuration 1.

Sample configuration 2 is a perpendicular channel arrangement. The bipolar plates are aligned such that gas flow channels run perpendicular to each other.

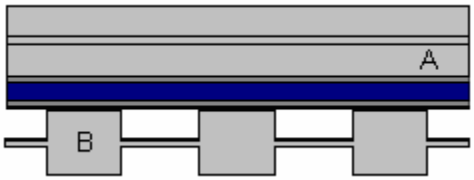

Figure 9: Sample Configuration 2.

Sample configuration 2 has 2 positions, open and closed. Open position refers to the samples that have been cut in the middle of the land area of plate A from Figure 9 above. This creates a sample that looks like Figure 10 below. Closed position refers to a sample that was cut in the flow area of plate A to obtain a sample that looks like that of Figure 11 below.

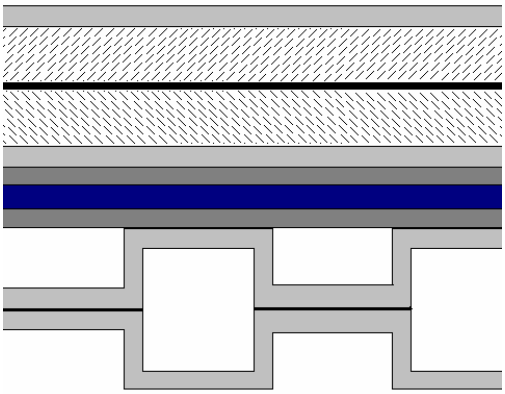

Figure 10: Open Position of Sample Configuration 2.

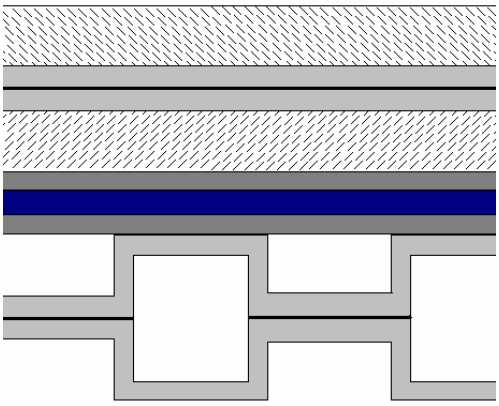

Figure 11: Closed Position of Sample Configuration 2.

Sample configuration 3 is a parallel channel offset arrangement. The bipolar plates are aligned such that gas flow channels run parallel to each other in the longitudinal direction but have an offset in the transverse direction.

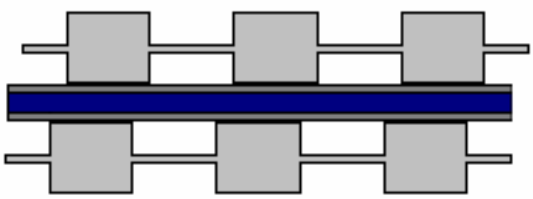

Figure 12: Sample Configuration 3.

Each sample was clamped using a 4 screw clamping system. ¼ inch ground flat stock was used as the clamp plates. The top plate contained 4, 4-40 through holes located at each corner and 2 through holes for 1/8 inch dowel pins to slide along located between the screw holes on the longer side. The bottom plate contained 4 tapped 4-40 through holes and 2 press fit dowel pin holes. An extensometer was used in conjunction with a compression test machine to obtain specified pressures. Force needed to obtain specified pressures was calculated using clamp plate area (0.7125 in^2) not contact area of the plates. This value was used because it better parallels the force applied to a stack setup. Total cell area is used when calculating force for stack compression rather than contact area. Table 2 shows the force needed to clamp each sample.

Table 2: Clamping Forces.

Pressure (psi)	Force (lb)
100	71.25
200	142.5
300	214.75

After clamping, measurements were taken at four points on the sample to insure parallel clamp plates. Measurements were taken inside the screw points to get accurate readings. Appendix A includes the measurement data for this step. Samples were then mounted using Buehler's Epothin Epoxy cold mount. The procedure for casting consisted of dripping epoxy onto one side of the sample in the mold until the mold started to fill. At this point the rest of the mold was filled with epoxy and the sample was placed into a vacuum chamber for approximately 10 minutes at a vacuum level of 20mg Hg. More epoxy was dripped on top of the sample and the sample was placed back into the vacuum. This step was repeated until no bubbles formed. Mounted samples were left to cure between 18 and 24 hours. After mounting, samples were cut using a 1.0025 inch thick aluminum oxide (Al_2O_3) cutting wheel, ground with silicon carbide papers, and polished using alumina slurries of 1μm and 0.5μm. Analysis was done with Polaroid and digital photography using a stereomicroscope, a Scanning Electron Microscope (SEM), and an optical

microscope. MicroGOP analysis software was used to map impingement of the GDL into the GFC. A reference line was drawn at the end of the bipolar plates and measurements were taken from the reference line to the end of the gas diffusion layer at an increment of 40 micrometers. Figure 13 shows the setup and measurement points for each sample. An arbitrary zero point was chosen where the reference line intersects the edge of the bipolar plate.

Figure 13: Measurement Positions.

Thicknesses of the three layers, GDL-MEA-GDL layers, were measured as well. An increment of 40 µm was used because it provided enough information about the features of the layers without creating too many data points. Microstructural analysis of the CFP was done using the SEM. Each sample was cut to expose two different faces within each sample. On each face four GFCs were measured for impingement, two on the anode side and two on the cathode side.

Results

Microstructural analysis shows that the carbon fiber paper has fibers that are no longer than 0.635 cm (0.25 in) in length and approximately 6μm in diameter. It was observed in handling that these materials tend to break rather than deform when bending force is applied. There was no orientation of properties observed for any specific direction in the longitudinal plane of the materials. No testing was done to compare longitudinal and transverse properties for these materials. When setups were created and GDL-MEA setups were clamped to 100, 200, 300, and 400psi breakage occurred in the 400psi and 300psi samples. This breakage was observed at the edge of the bipolar plate land areas that were in contact with the gas diffusion material. 400psi samples showed breakage of the MEA as well as the GDL materials. 300psi samples showed no breakage of the MEA but some deformation. 200psi samples showed some deformation and indications of breakage of the GDL materials but no visible sign of permanent deformation or breakage of the MEA layer. 100psi samples showed some deformation and slight indications of breakage of the GDL. Figure 14 shows an SEM image of one side of the anode side of GDL 2 at 20x magnification. The complete set of images of each side of each gas diffusion layer is included in Appendix B. Carbon fibers are held in a carbon matrix which produces a semi rigid body. These papers have randomly oriented fibers that produce a very porous structure. Pore sizes and shapes vary due to the orientation of the fibers. There are few if any closed pores in the structure. Much of the mechanical behavior of the gas diffusion layers can be attributed to the large amount of porosity in the papers. Figure 14 and Figure 15 show little variation in fiber diameter. Figure 15 below shows the cross section of a carbon fiber. The diameter of this fiber is approximately 6μm, thus most fibers in the papers are roughly 6μm in diameter.

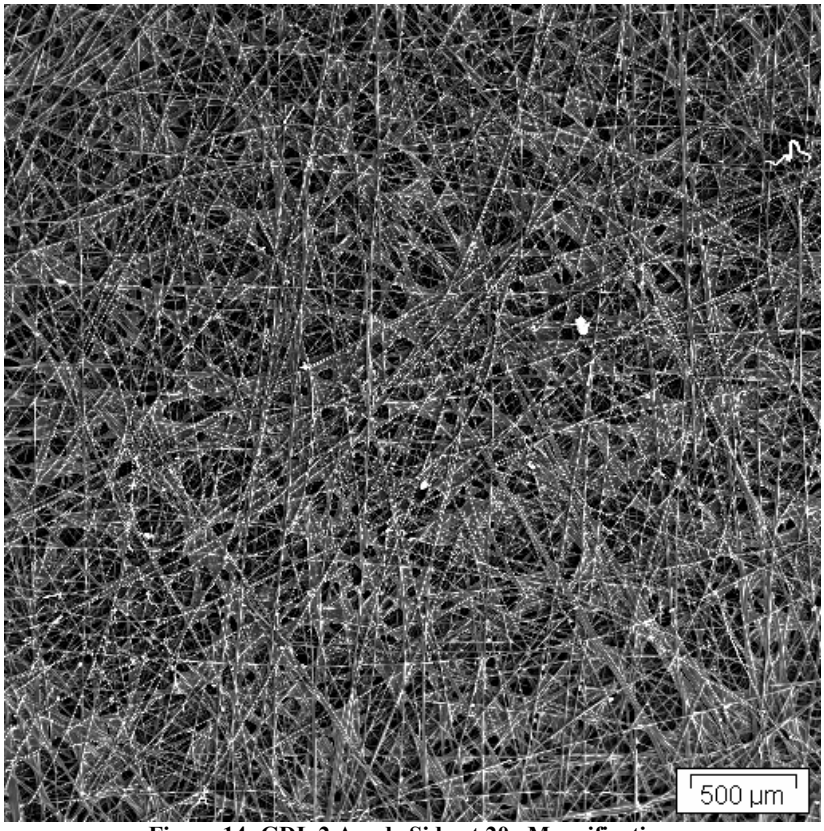

Figure 14: GDL 2 Anode Side at 20x Magnification.

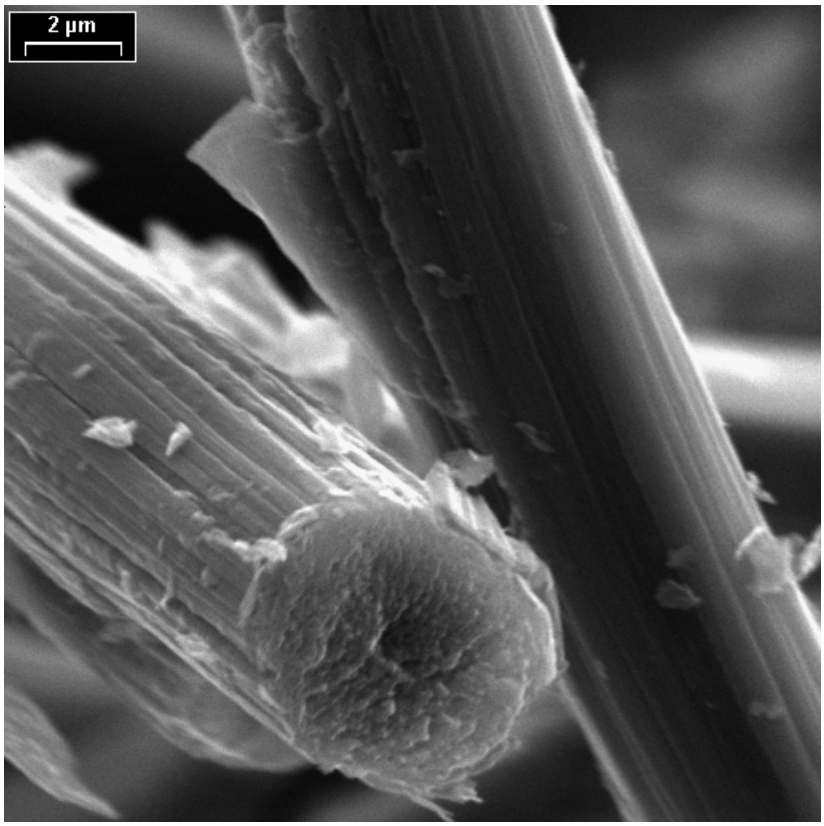

Figure 15: Fiber Cross-Section.

Images of transverse sections of each paper show that the thickness of all 4 papers is roughly the same, approximately 190µm. GDL 2 papers were observed to be approximately 10µm thicker than GDL 1 papers. GDL 2 papers were identical on both cathode and anode sides; one side of each paper was coated and the other not. GDL 1 had two distinct papers for anode and cathode sides. Cathode papers of GDL 1 were coated on one side only, anode papers were not coated.

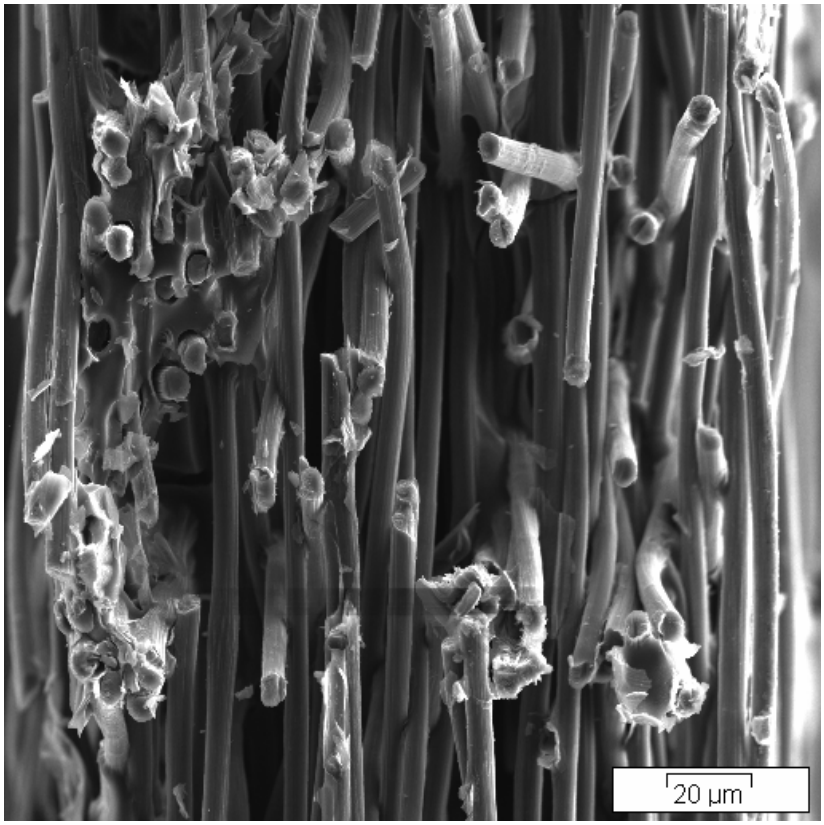

Figure 16: GDL 1 Anode Point 1 400x.

Extensometer data was collected and shown in the graphs below. This data shows the extension versus load for each sample that was clamped. The load was recorded from the load cell in the machine and extension data was collected from the extensometer displacement. Samples were loaded at a rate of 0.1 inch per minute. Figure 17 below shows the trend curves for each sample class. Samples loaded evenly with only some samples lying outside of the trend. Each pressure level results in the same distribution of sample configurations with the exception of 2 samples.

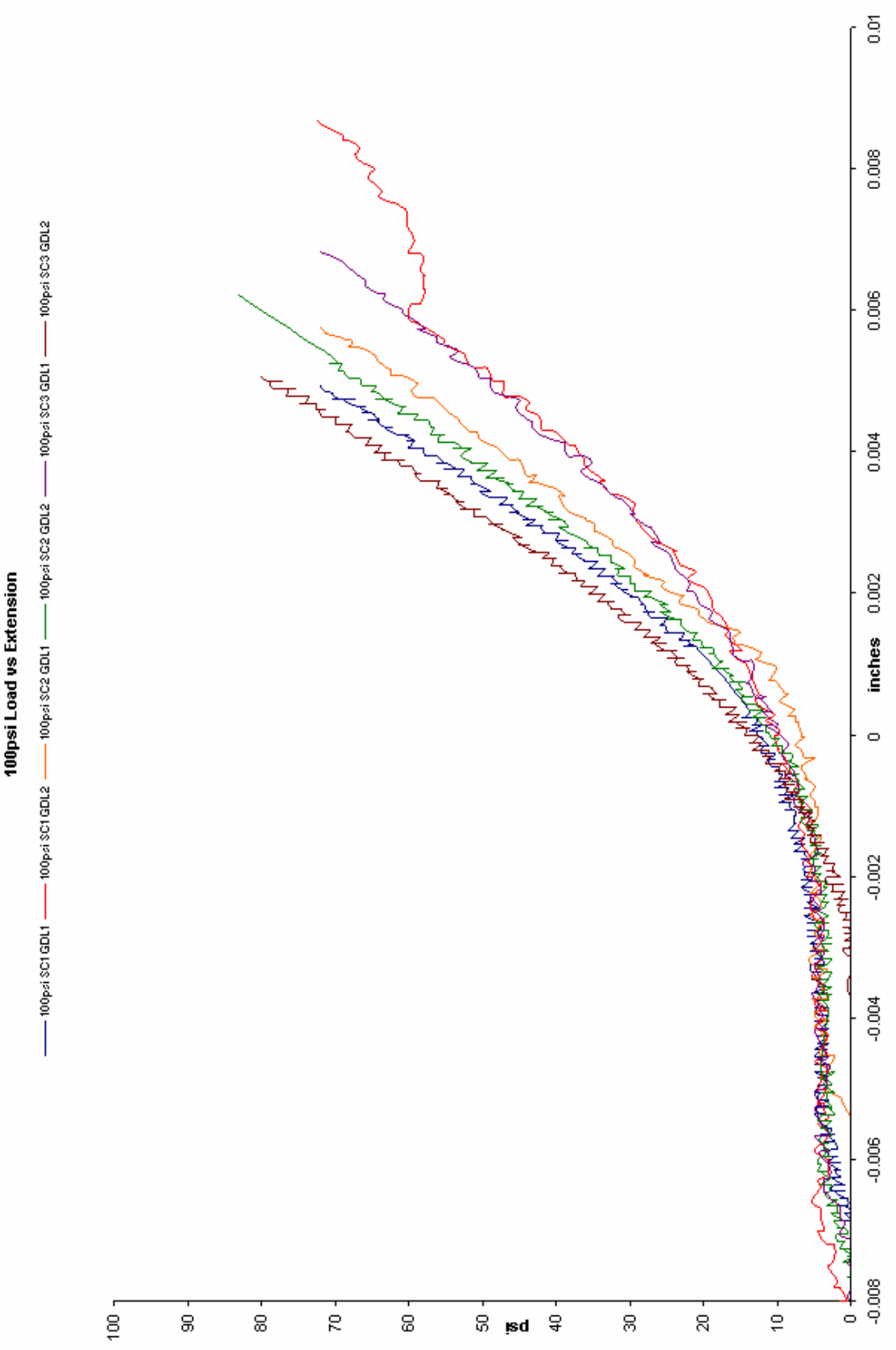
100psi Load vs Extension
100psi SC1 GDL1
100psi SC1 GDL2
100psi SC2 GDL1
100psi SC2 GDL2
100psi SC3 GDL1
100psi SC3 GDL2
psi
inches
100
90
80
70
60
50
40
30
20
10
0
-0.008
-0.006
-0.004
-0.002
0
0.002
0.004
0.006
0.008
0.01

(a)


200psi Load vs Extension
200psi SC1 GDL1
200psi SC1 GDL2
200psi SC2 GDL1
200psi SC2 GDL2
200psi SC3 GDL1
200psi SC3 GDL2
psi
inches
200
180
160
140
120
100
80
60
40
20
0
-0.008
-0.006
-0.004
-0.002
0
0.002
0.004
0.006
0.008
0.01

(b)

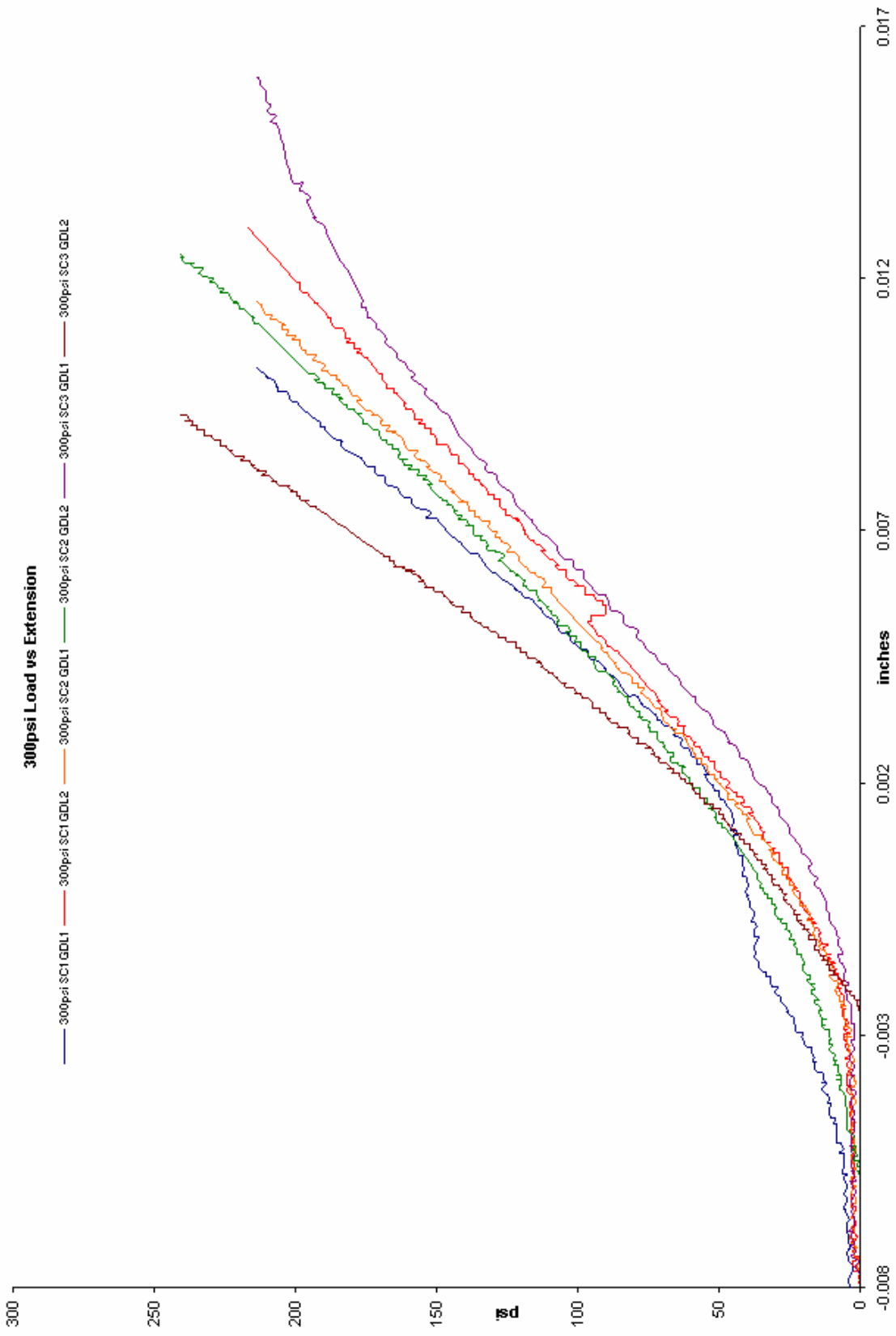

(c)

Figure 17: Extension vs Load Data for Clamped Samples.

Sample maps and data tables were produced using collected data. Figure 18 shows the method of obtaining the change in bipolar plate thicknesses. Clamping forces produce a deformation in the samples which is then measured. Δt_0 and Δt_2 are known from measured values and therefore $2\Delta t_1$ can be calculated using the equation below. $2\Delta t_1$ is the value represented in the Table 5. Sample configuration 3 does not differentiate the GDL-MEA setup from the bipolar plate set because thicknesses of the GDL-MEA setups alone were not taken. Only overall change in thickness of each cell setup is shown.

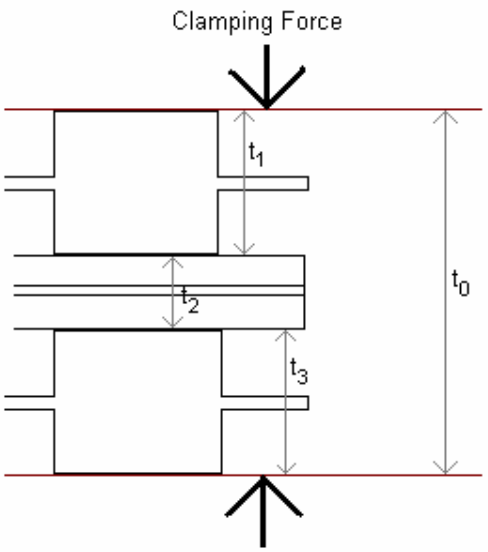

$$\Delta t_0 = \Delta t_1 + \Delta t_2 + \Delta t_3$$
$$2\Delta t_1 = \Delta t_1 + \Delta t_3$$
$$\Delta t_0 = 2\Delta t_1 + \Delta t_2$$

Δt_2 = Change in GDL-MEA Thicknesses

Δt_1, Δt_3 = Change in Bipolar Plate Thicknesses

Δt_0 = Change in Overall Thickness

Figure 18: Thickness Equations.

Table 3 shows the thickness of the GDL-MEA setups between the bipolar plates for each sample. This data shows the measurements for only the GDL-MEA setup and does not take into consideration the bipolar plate thickness. Sample configuration 3 thicknesses were not measured. Table 4 shows the amount of deformation in the GDL-MEA setup for each sample. Original thicknesses are measurements of the unloaded GDL-MEA set for GDL 1 and GDL 2. Measurements of original thicknesses were taken using a micrometer; all other measurements in this table were taken using the MicroGOP software system. All measurements included in the table are in micrometers.

This data is also displayed in chart form below. GDL thickness changes are, on average, larger than bipolar plate thickness changes. Sample configuration 1, GDL 2 shows almost no bipolar plate deformation at all. Bipolar plate sets show larger deformation for GDL 2 for 200psi and 300psi but larger deformation for GDL 1 for 100psi in both sample configurations. Overall the trend is for bipolar plate deformation to increase with increasing applied pressure.

Table 3: Thickness of GDL-MEA Setups After Clamping.

Thicknesses (μm)							
Sample Configuration 1	Point 1	Point 2	Point 3	Point 4	Average		
100psi GDL 1	309.3	309.8	288.7	298.6	301.6		
100psi GDL 2	237.5	242.5	242.9	238.4	240.325		
200psi GDL 1	226.2	226	265.2	255.7	243.275		
200psi GDL 2	233.4	268	265.6	x	255.6667		
300psi GDL 1	193	186.4	195.2	192.2	191.7		
300psi GDL 2	252.4	235.9	228.5	205.4	230.55		
Sample Configuration 2	Open		Closed		Average		
	Point 1	Point 2	Point 1	Point 2	Open	Closed	Total
100psi GDL 1	367	358.8	379.4	363.7	362.9	371.55	367.225
100psi GDL 2	289.5	261.4	292.5	303.1	275.45	297.8	286.625
200psi GDL 1	258.1	270.5	x	x	264.3	x	264.3
200psi GDL 2	384.3	355.5	287.8	290.6	369.9	289.2	329.55
300psi GDL 1	201.2	197.9	262.3	264.7	199.55	263.5	231.525
300psi GDL 2	239.2	240.8	242.4	254.6	240	248.5	244.25

Table 4: Change in Thicknesses of GDL-MEA Setup.

Change of Thicknesses (μm)							
Original Thicknesses							
GDL-MEA setup for GDL 1	404						
GDL-MEA setup for GDL 2	438						
Change in Thickness							
Sample Configuration 1	Point 1	Point 2	Point 3	Point 4	Average		
100psi GDL 1	94.7	94.2	115.3	105.4	102.4		
100psi GDL 2	200.5	195.5	195.1	199.6	197.675		
200psi GDL 1	177.8	178	138.8	148.3	160.725		
200psi GDL 2	204.6	170	172.4	x	182.3333		
300psi GDL 1	211	217.6	208.8	211.8	212.3		
300psi GDL 2	185.6	202.1	209.5	232.6	207.45		
Sample Configuration 2	Open		Closed		Average		
	Point 1	Point 2	Point 1	Point 2	Open	Closed	Total
100psi GDL 1	37	45.2	24.6	40.3	41.1	32.45	36.775
100psi GDL 2	148.5	176.6	145.5	134.9	162.55	140.2	151.375
200psi GDL 1	145.9	133.5	x	x	139.7		139.7
200psi GDL 2	53.7	82.5	150.2	147.4	68.1	148.8	108.45
300psi GDL 1	202.8	206.1	141.7	139.3	204.45	140.5	172.475
300psi GDL 2	198.8	197.2	195.6	183.4	198	189.5	193.75

Table 5: Change in Thicknesses of Bipolar Plates.

Change in Thicknesses of One Cell Setups (μm)		
	Original Thickness	Totals
Bipolar Plate	1327	2654
GDL-MEA setup for GDL 1	404	3058
GDL-MEA setup for GDL 2	438	3092
Sample Configuration 1		Bipolar Plates
100psi GDL 1	2892.11	63.49
100psi GDL 2	2892.74	1.58
200psi GDL 1	2819.72	77.56
200psi GDL 2	2823.21	86.46
300psi GDL 1	2746.06	99.64
300psi GDL 2	2747.01	137.54
Sample Configuration 2		
100psi GDL 1	2888.62	132.61
100psi GDL 2	2912.43	28.20
200psi GDL 1	2823.53	94.77
200psi GDL 2	2745.90	237.65
300psi GDL 1	2744.15	141.37
300psi GDL 2	2740.66	157.59
Sample Configuration 3		Whole Cell
100psi GDL 1	2904.49	153.51
100psi GDL 2	2921.00	171.00
200psi GDL 1	2826.07	231.93
200psi GDL 2	2818.13	273.87
300psi GDL 1	2692.08	365.92
300psi GDL 2	2678.11	413.89

A comparison of this data in the form of stress – strain curves is shown below. The stress – strain curves for change in thickness of the GDL setups have smaller slopes than for the bipolar plates which means less stress is needed to create a larger strain. This means that the GDLs are more likely to deform first. The most likely event is for the fibers to deform and fill open pores within the papers.

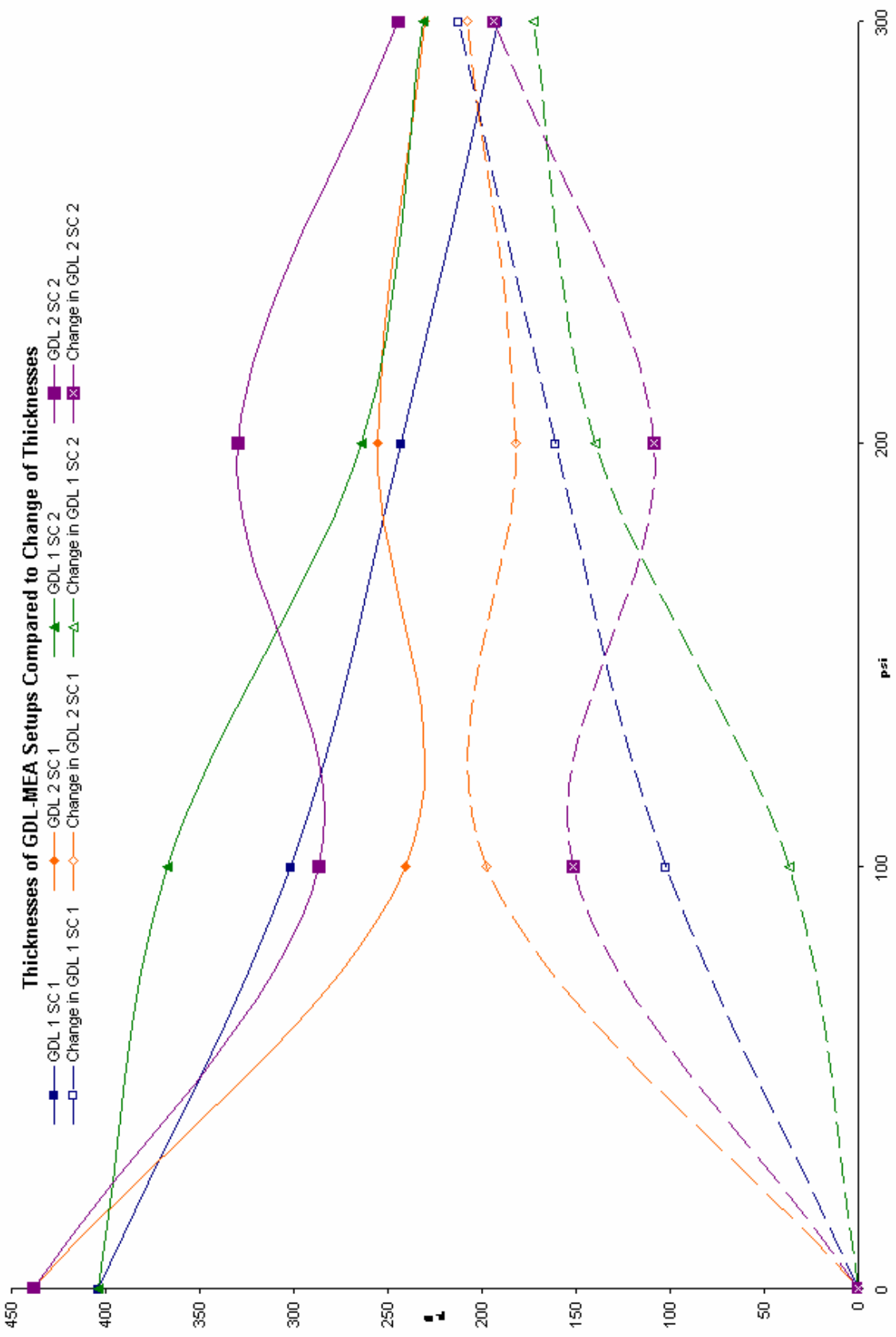

Figure 19: Impingement Data Chart 1.

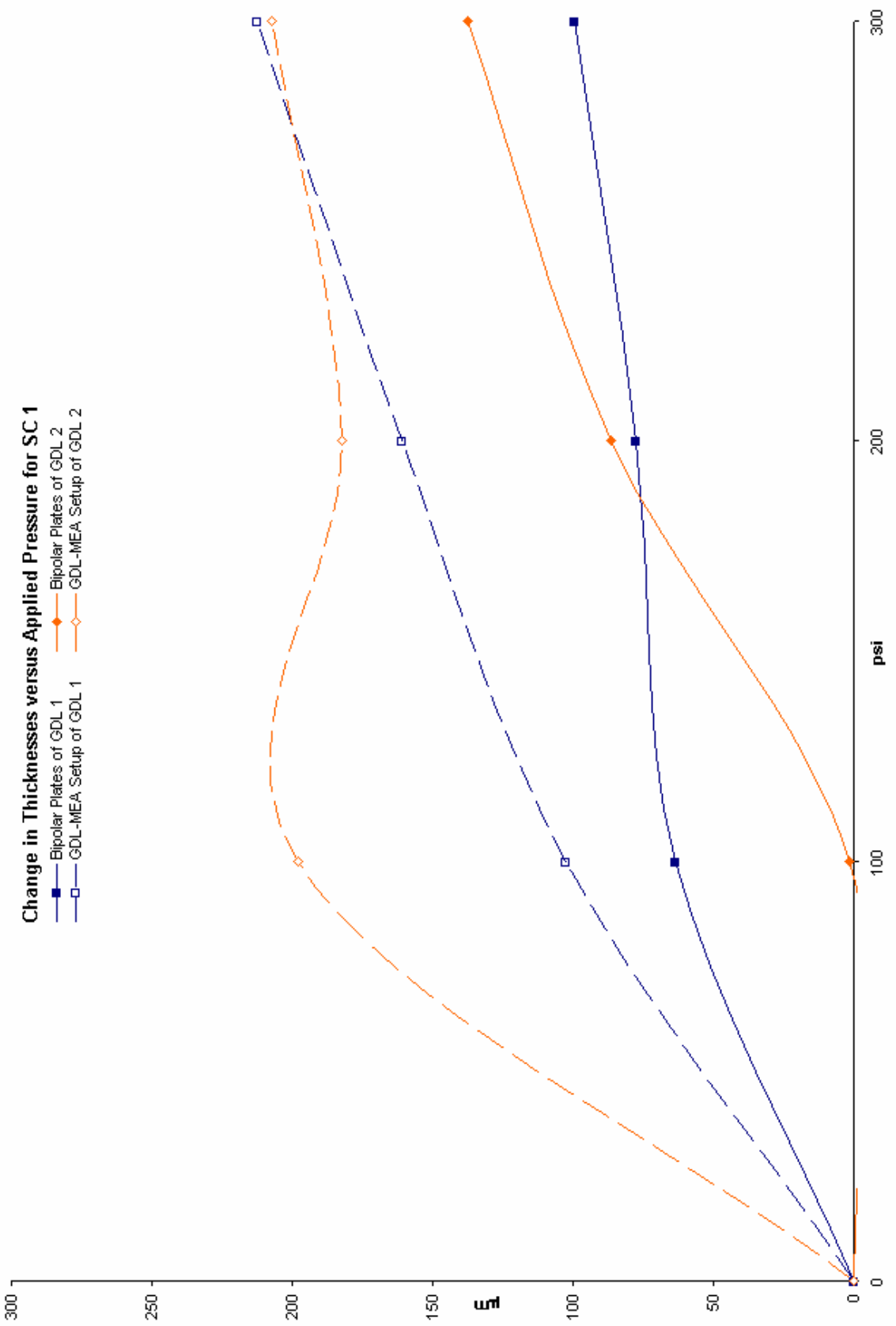

Figure 20: Impingement Data Chart 2.

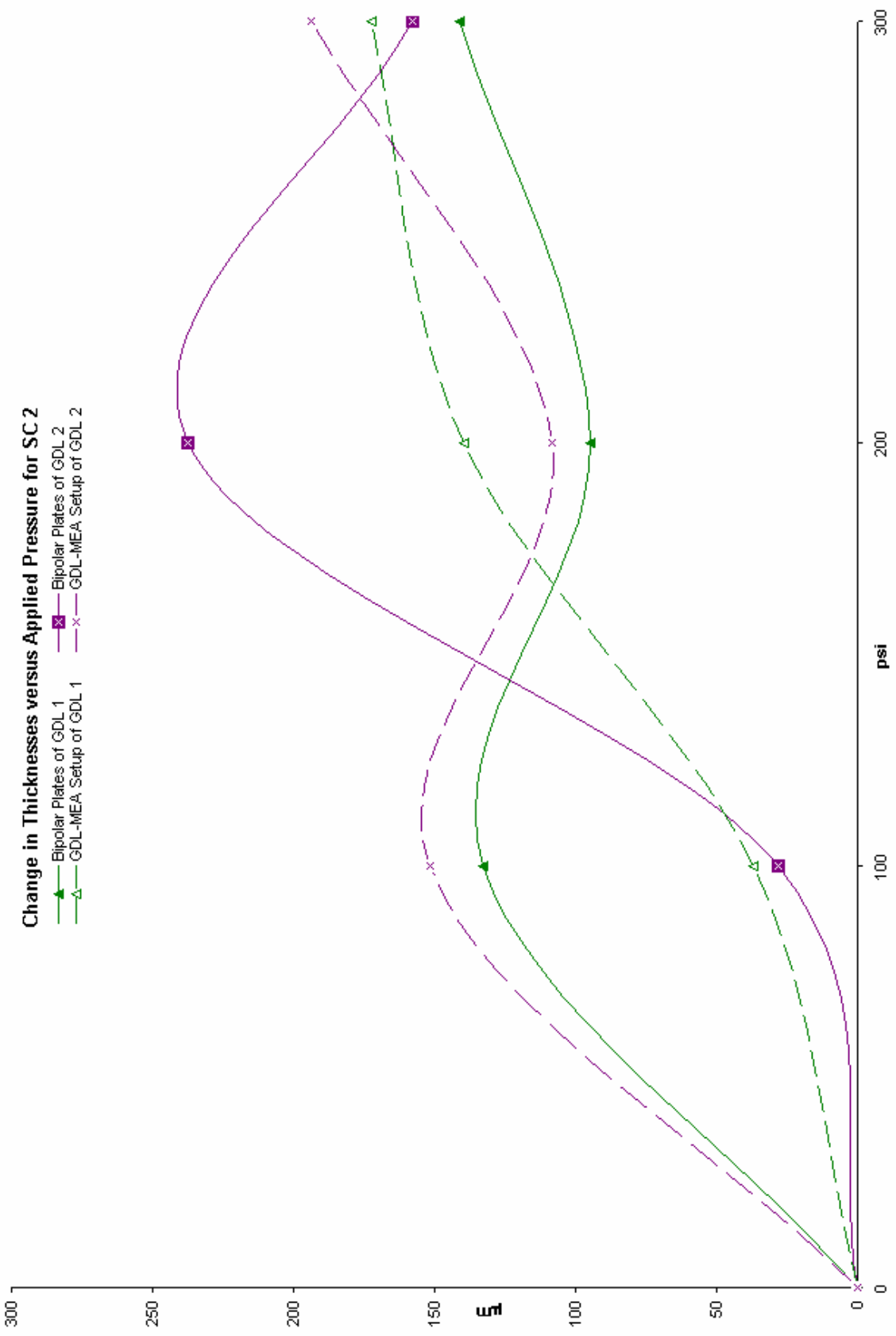

Figure 21: Impingement Data Chart 3.

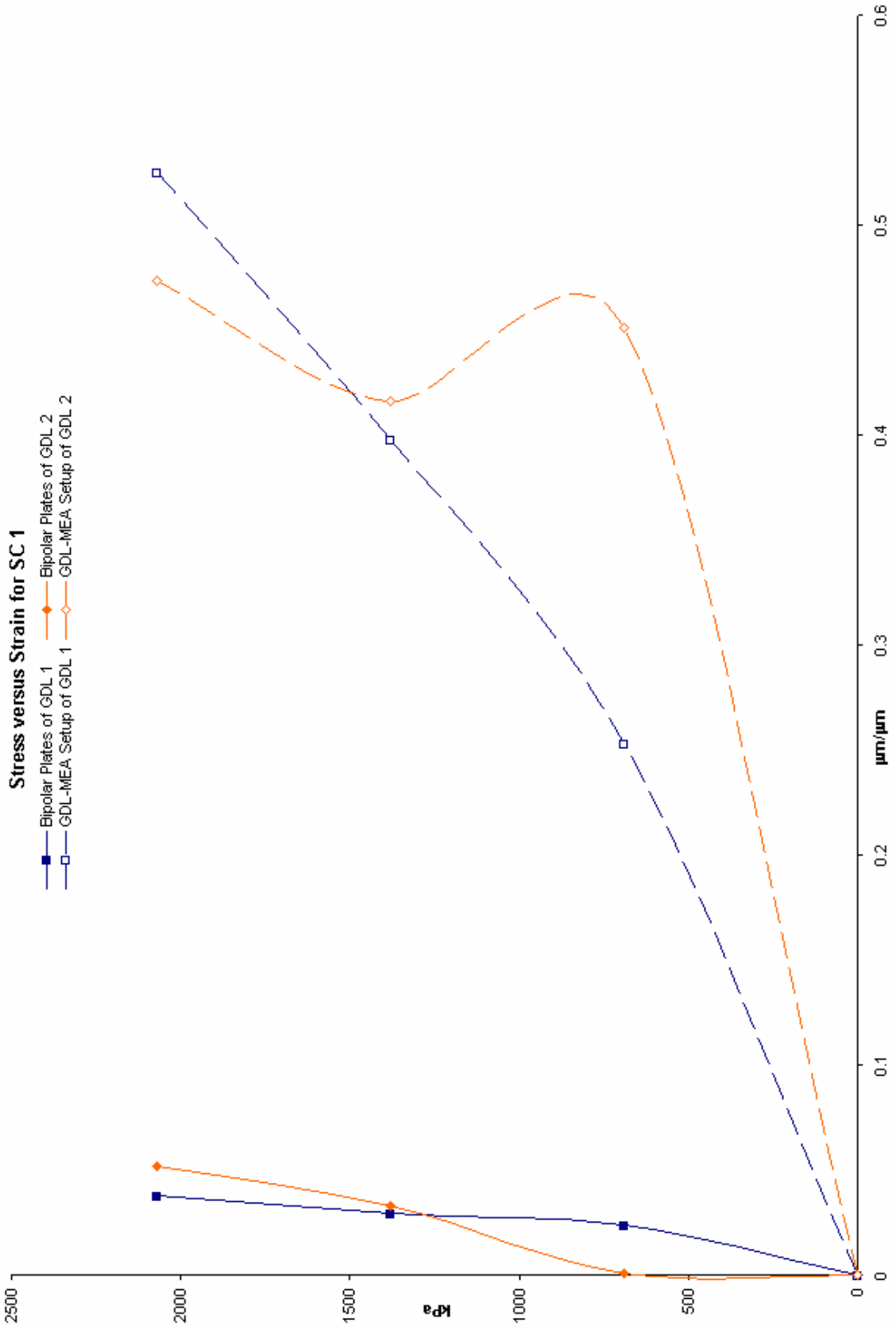

Figure 22: Impingement Data Chart 4.

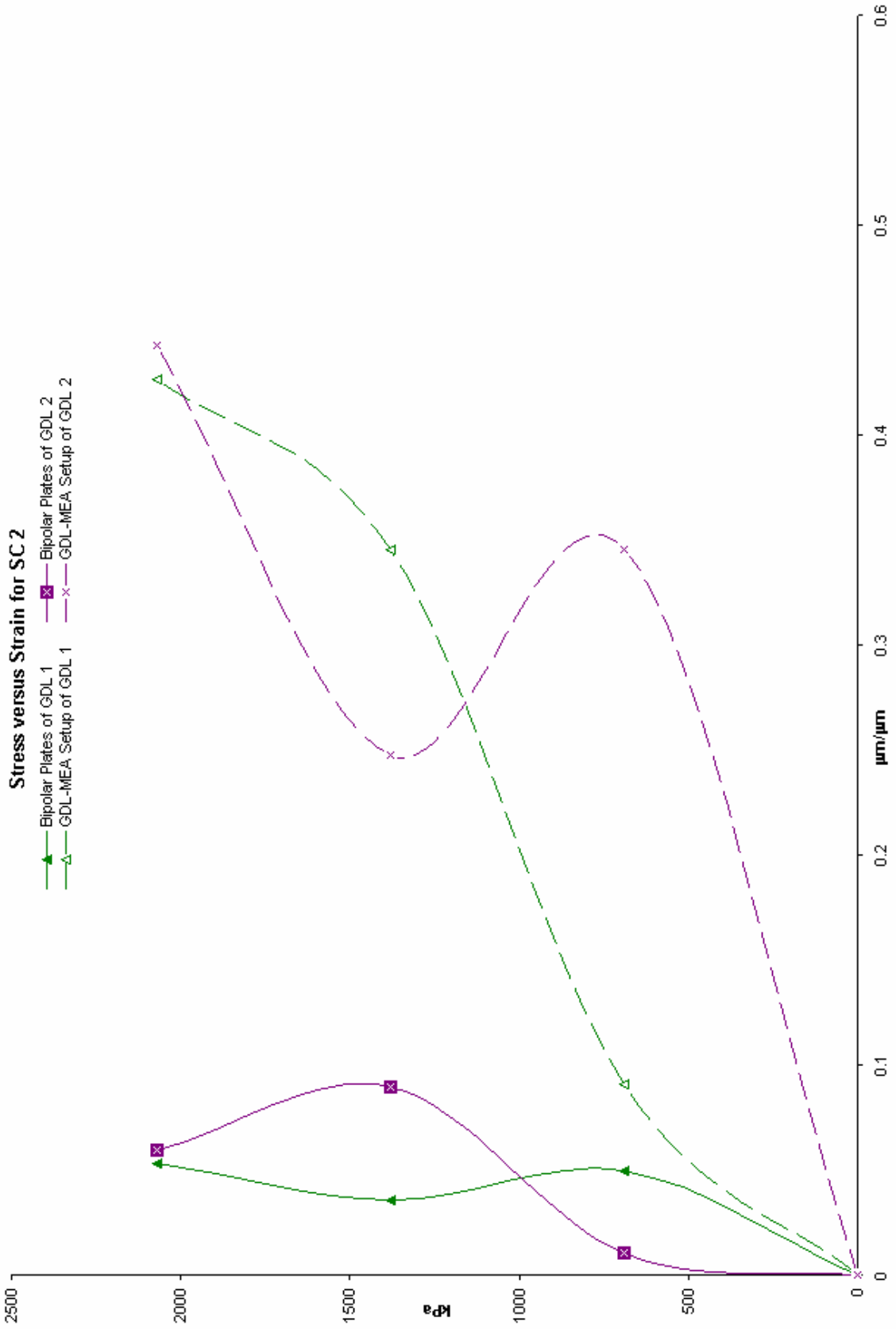

Figure 23: Impingement Data Chart 5.

Sample configuration 2 shows slightly different behavior than sample configuration 1. While both GDL-MEA setups and bipolar plates have the same distribution of points, meaning the curves have roughly the same shape and relative orientation to each other, average slopes of the curves for SC 1 differ slightly from SC 2 curve slopes. Slopes of the bipolar plate curves are slightly lower for SC 2 than SC 1, meaning that SC 2 plates deform more easily. The opposite is true of GDL-MEA setups; average curve slopes for SC 1 are slightly lower than SC 2 curve slopes. Thus it can be said that having perpendicular channel configurations can cause a slight increase in the bipolar plate deformation during clamping.

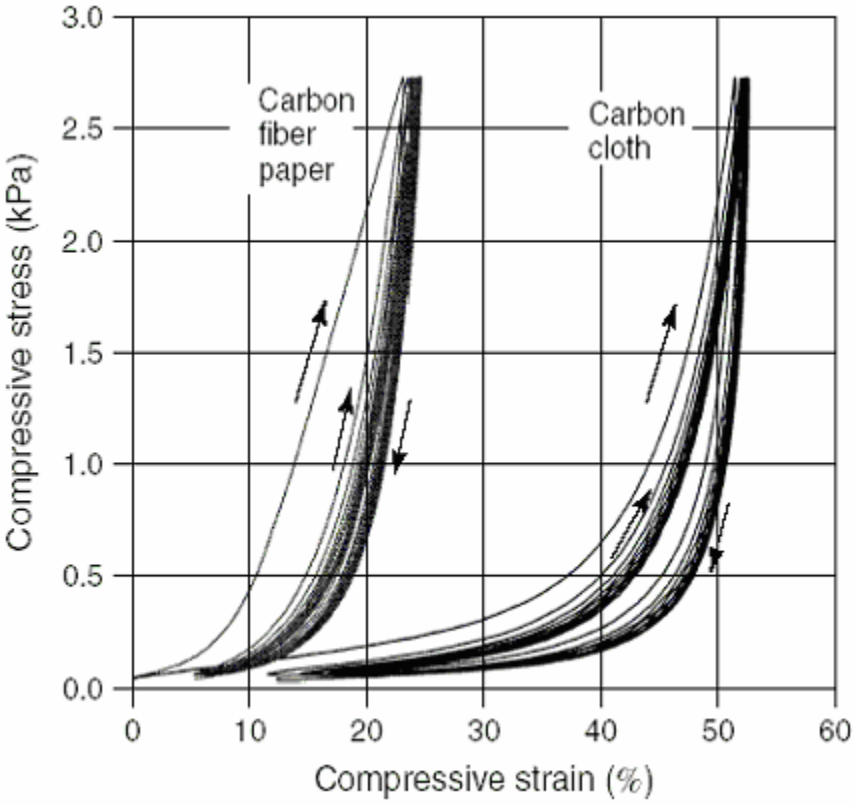

Figure 24: Compression Data for Carbon Fiber Paper and Carbon Cloth.

The data in Figure 24 correlates to data obtained in experimentation. This shows that the GDL-MEA layers react to compression in a similar manner as the GDL tested for Figure 24. Even though we have carbon fiber papers the GDL-MEA setup acts more like a carbon cloth than carbon fiber paper according to the curves above. A complete correlation can not be made because the testing was not done under the same circumstances.

Figures 25 and 26 show average maximum impingements of the cathode sides of SC 1 for both GDL sets. This data was obtained using the following formula:

$$\frac{1}{2} t_2 + \text{Average Impingement} = \text{Average Maximum Impingement}$$

GDL 2 shows larger average maximum impingement than GDL 1. A possible reason for this is the larger initial thickness of GDL 2.

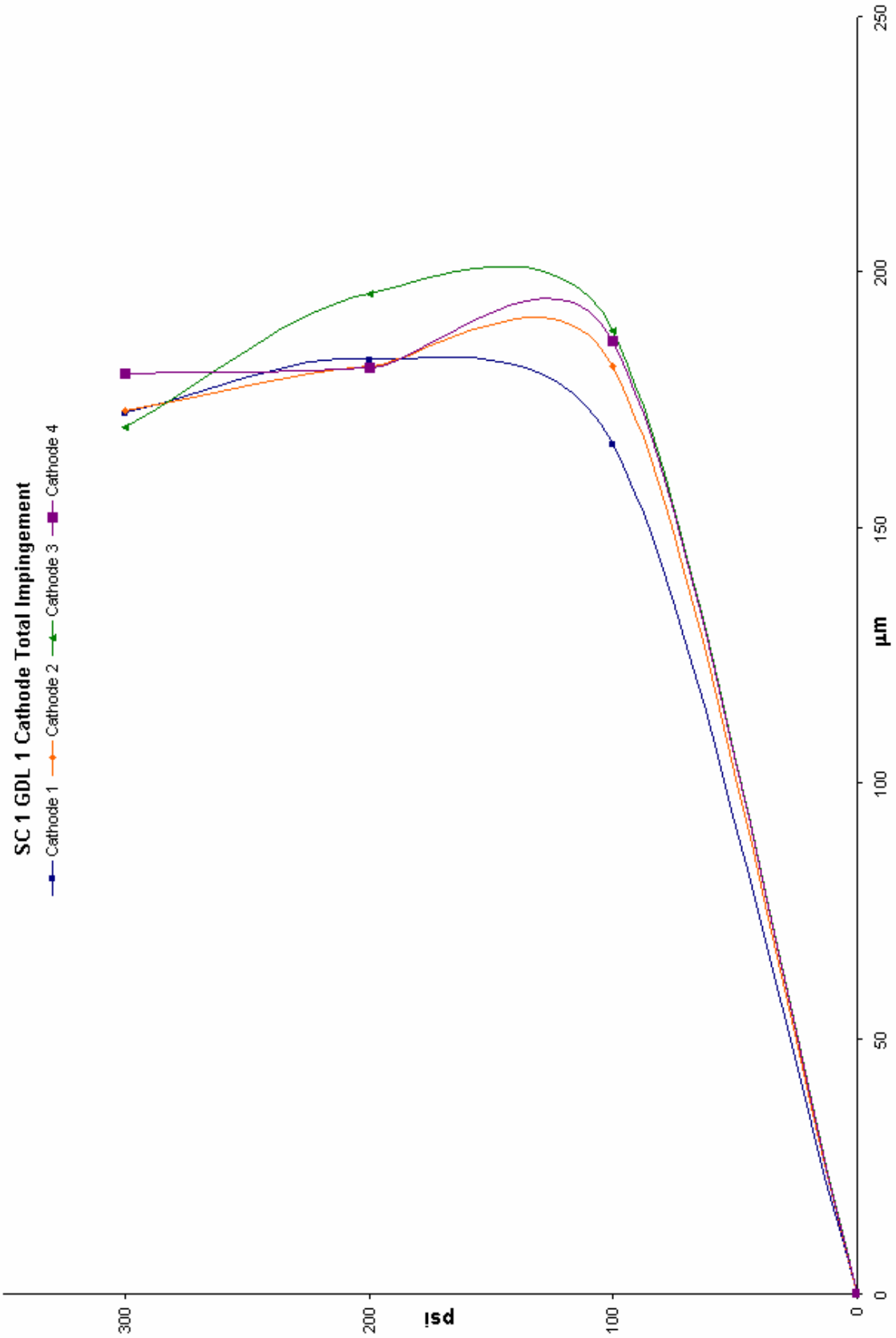

Figure 25: Impingement Data Chart 6.

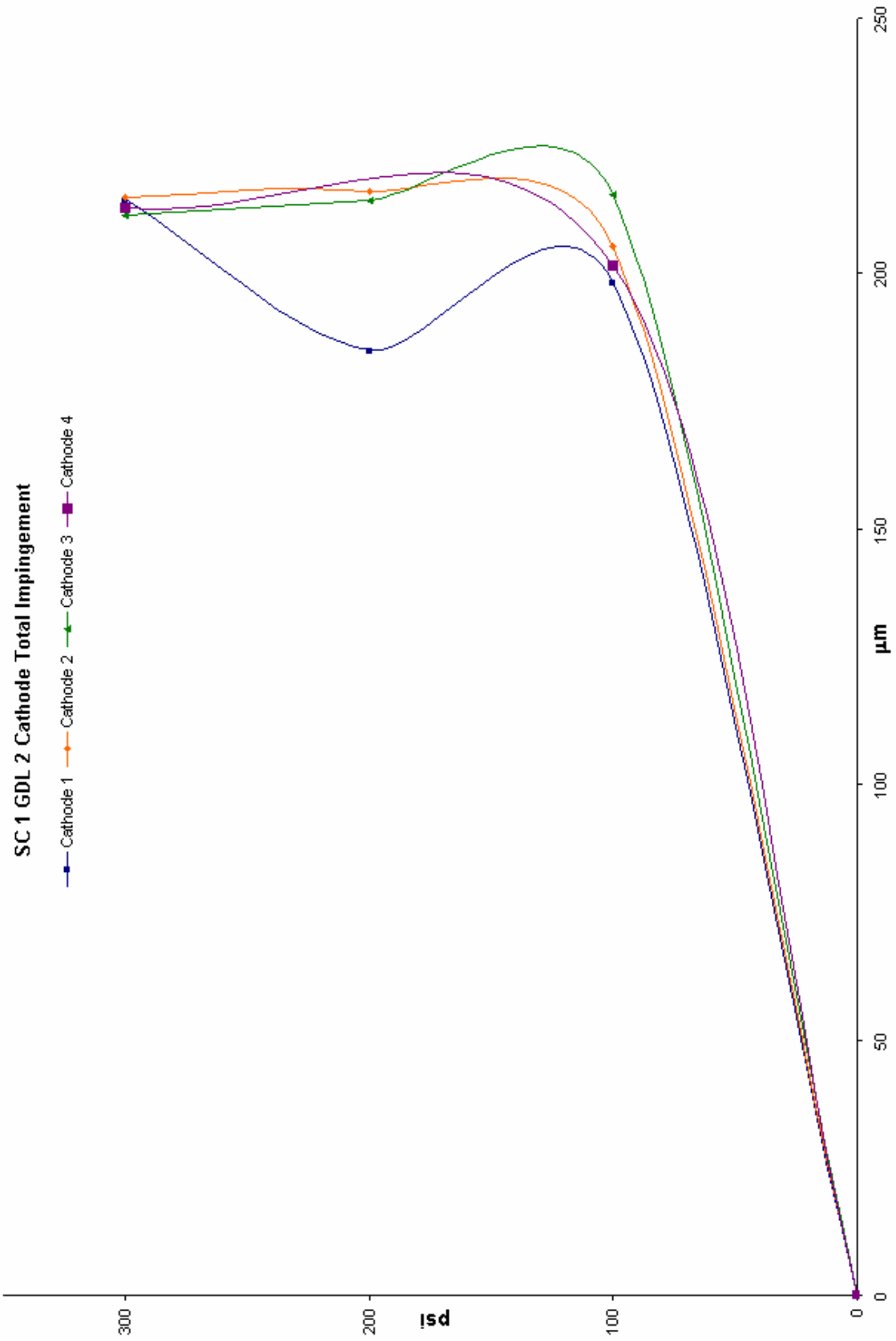

Figure 26: Impingement Data Chart 7.

Sample configuration 1 impingement maps below characterize the impingement properties of the GDL-MEA setups as a function of pressure. These charts show the impingement of the gas diffusion materials into the gas flow channels, each point corresponds to the impingement value at the distance from the arbitrary zero point specified. Each point was measured approximately 40 micrometers apart. Figures 27 and 28 show how GDL 1 reacts to increasing applied pressure. The trend is such that as applied pressure increases impingement increases. Figures 29 and 30 show how GDL 2 reacts to increasing applied pressure. The trend in the lines of Figures 27 to 30 shows that the impingement of gas diffusion material into the gas flow channels increases with increasing applied pressure. These charts show that cathode sides display larger impingements than anode sides which can be seen more clearly in Figures 35 to 38. Clamps were constructed such that one side was stationary while the other traveled during clamping. Anode gas diffusion layers were always situated on the stationary side of the clamps and cathode layers on the traveling side. This may explain why cathode sides show larger impingements than anode sides. This parallels the phenomenon found in powder pressing. One sided pressing produces packed powder with a greater density on the side of impact than the stationary side.

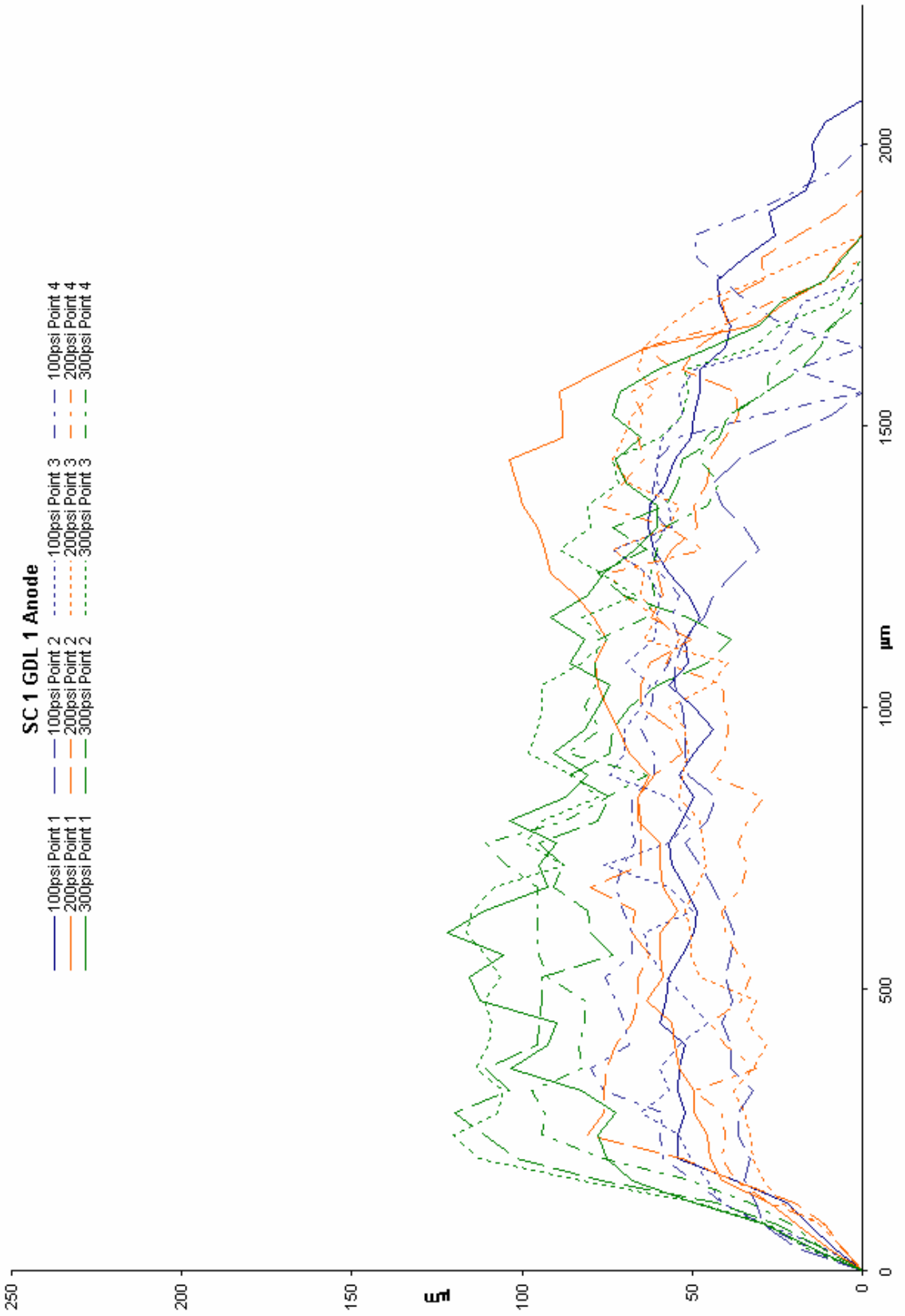

Figure 27: Impingement Data Chart 8.

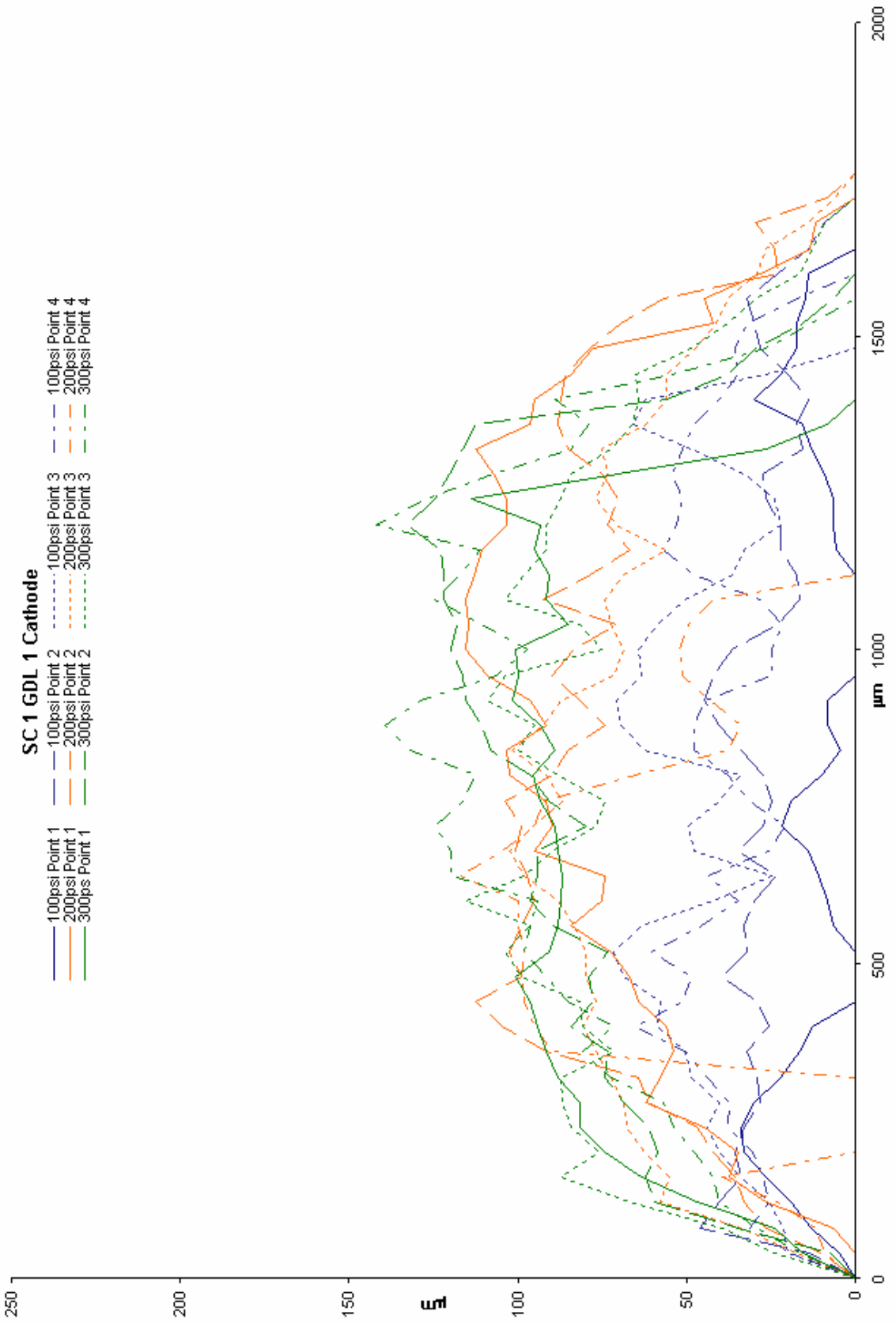

Figure 28: Impingement Data Chart 9.

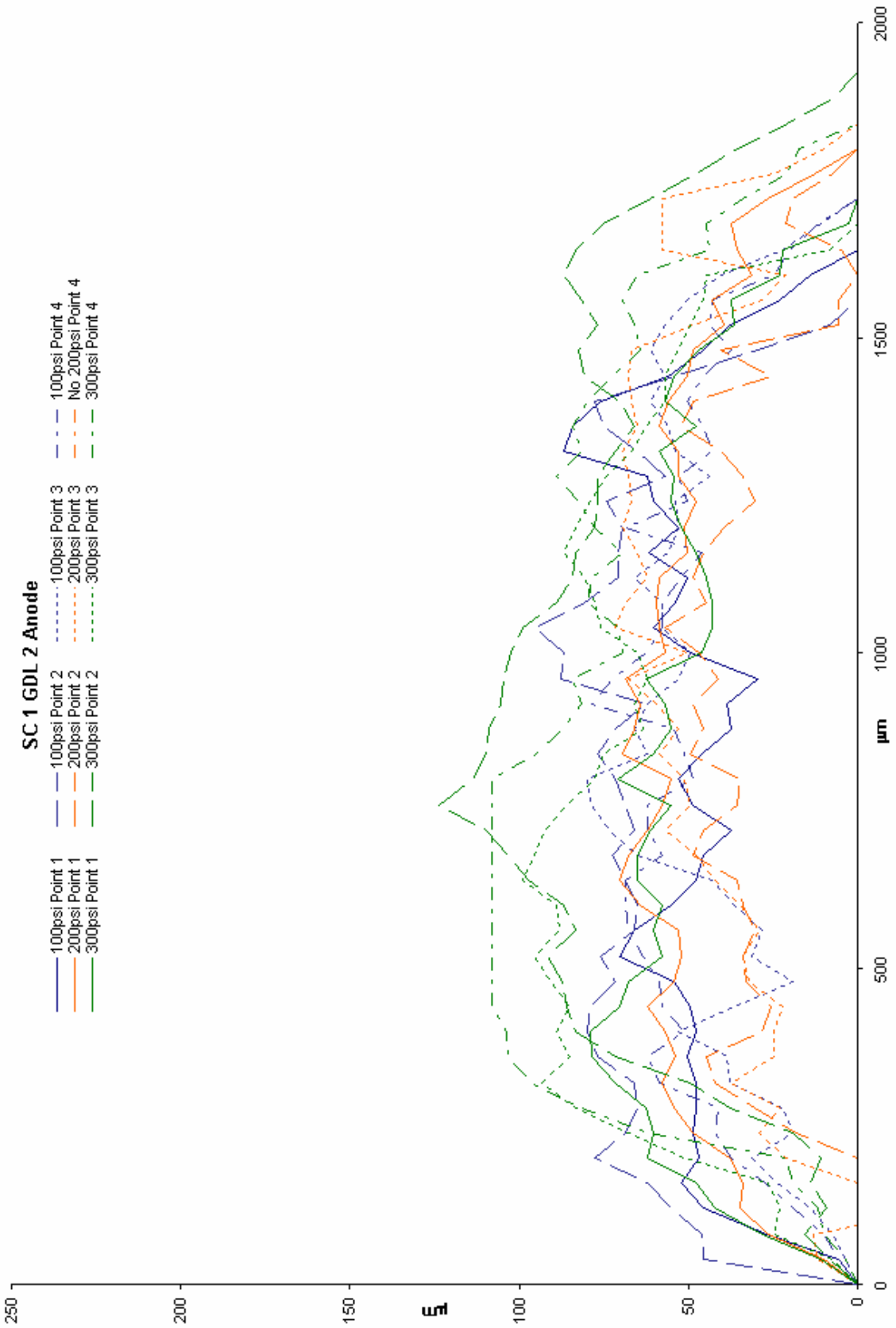

Figure 29: Impingement Data Chart 10.

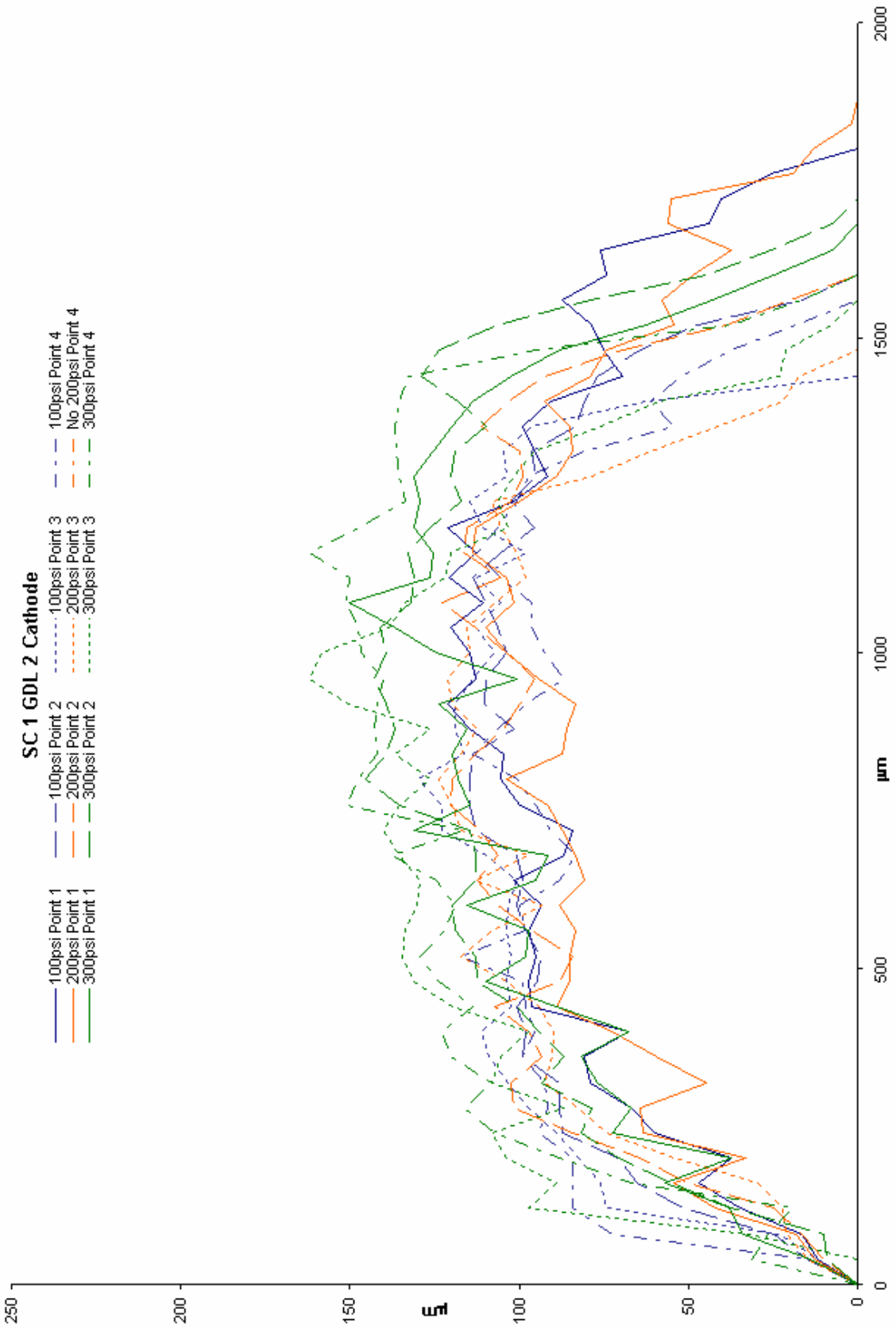

Figure 30: Impingement Data Chart 11.

GDL 1 cathode shows the largest distribution of impingement for increasing applied pressure. The coating on GDL 1 cathode papers could have penetrated the surface of the paper and changed its compression properties. Page 83 in Appendix B shows a transverse section of cathode side of GDL 1. This set of images that the coating penetrated about halfway. However, this could be due to a difference in the paper itself, disregarding any coating. This paper could have been manufactured differently from the rest, a different precursor, different oxidation temperatures, or different carbonization or graphitization temperatures or times.

GDL 2 cathode papers tend to show larger impingements than GDL 1 cathode papers for SC 1. A larger difference is seen at 100psi than 300psi for the cathode papers. This may be due, again, to the large number of pores in each paper. 200psi charts are included in Appendix C. At 100psi more deformation could be in the form of pore filling but at 300psi pores could be mostly to completely filled and deformation would have to manifest itself in a different way. Anode papers show little discernable differences in impingement between GDL 1 and 2. It is likely anode papers are more alike in microstructure and therefore in mechanical properties than cathode papers and thus show less differences in impingement.

Differences in anode and cathode impingements are more pronounced in GDL 2 as shown in Figures 35 to 37. For GDL 2 cathode sides show larger impingements than anode sides. This mostly likely has to do with the fact that the cathode sides were situated on the traveling side of the clamps because GDL 2 papers were identical. GDL 1 shows cathode papers having slightly larger impingements than anode papers except for 100psi which has anode papers showing slightly larger average impingements.

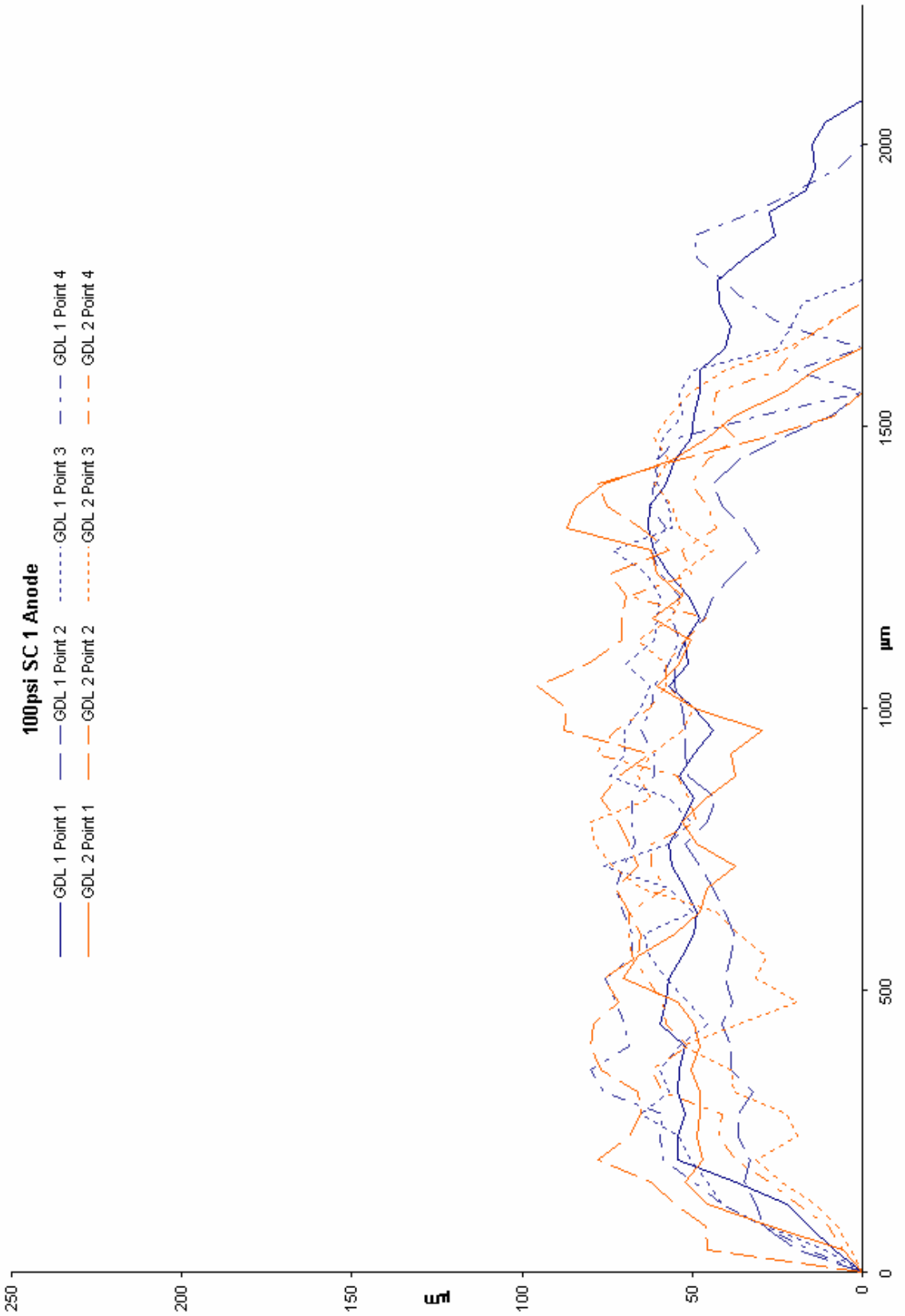

Figure 31: Impingement Data Chart 12.

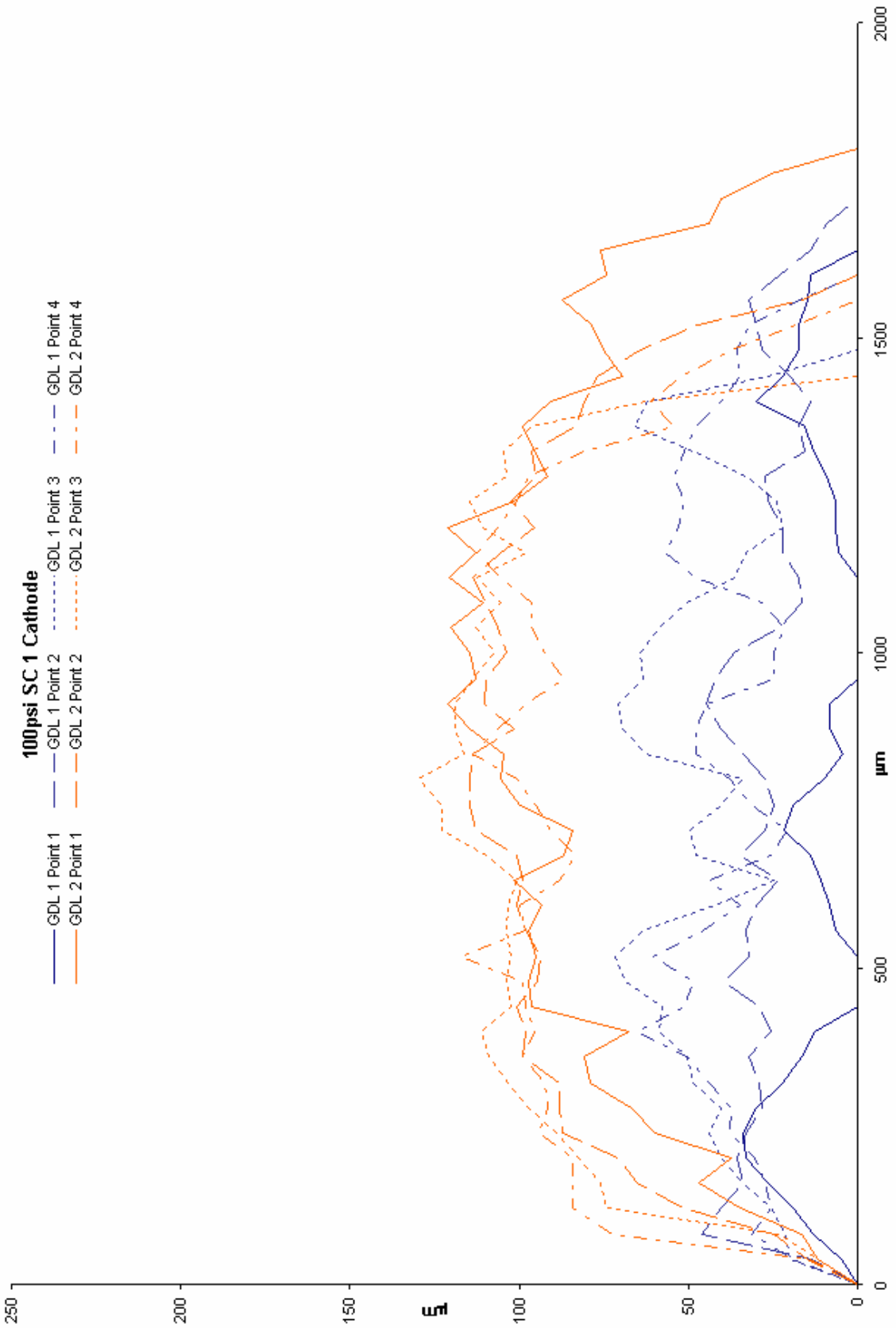

Figure 32: Impingement Data Chart 13.

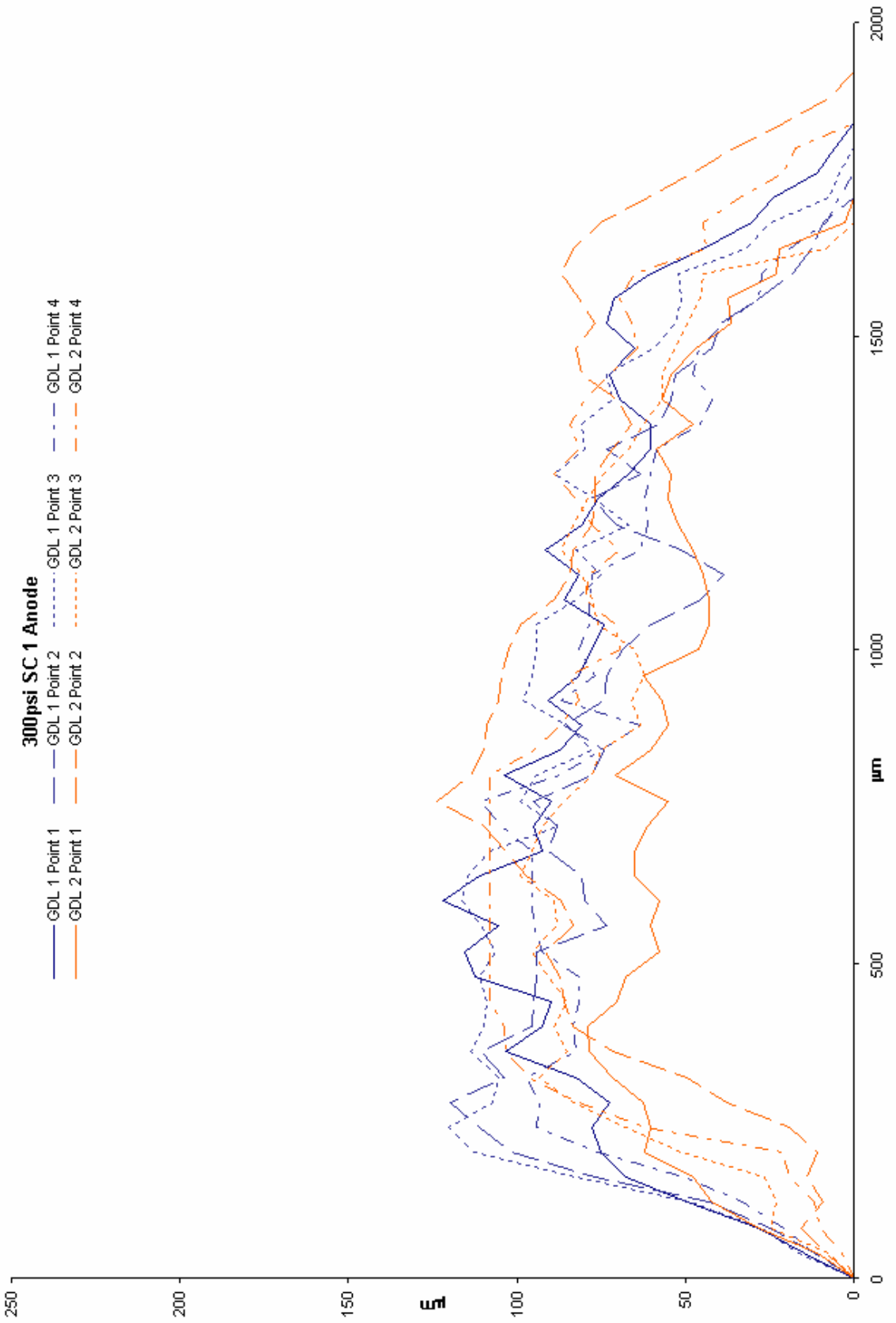

Figure 33: Impingement Data Chart 14.

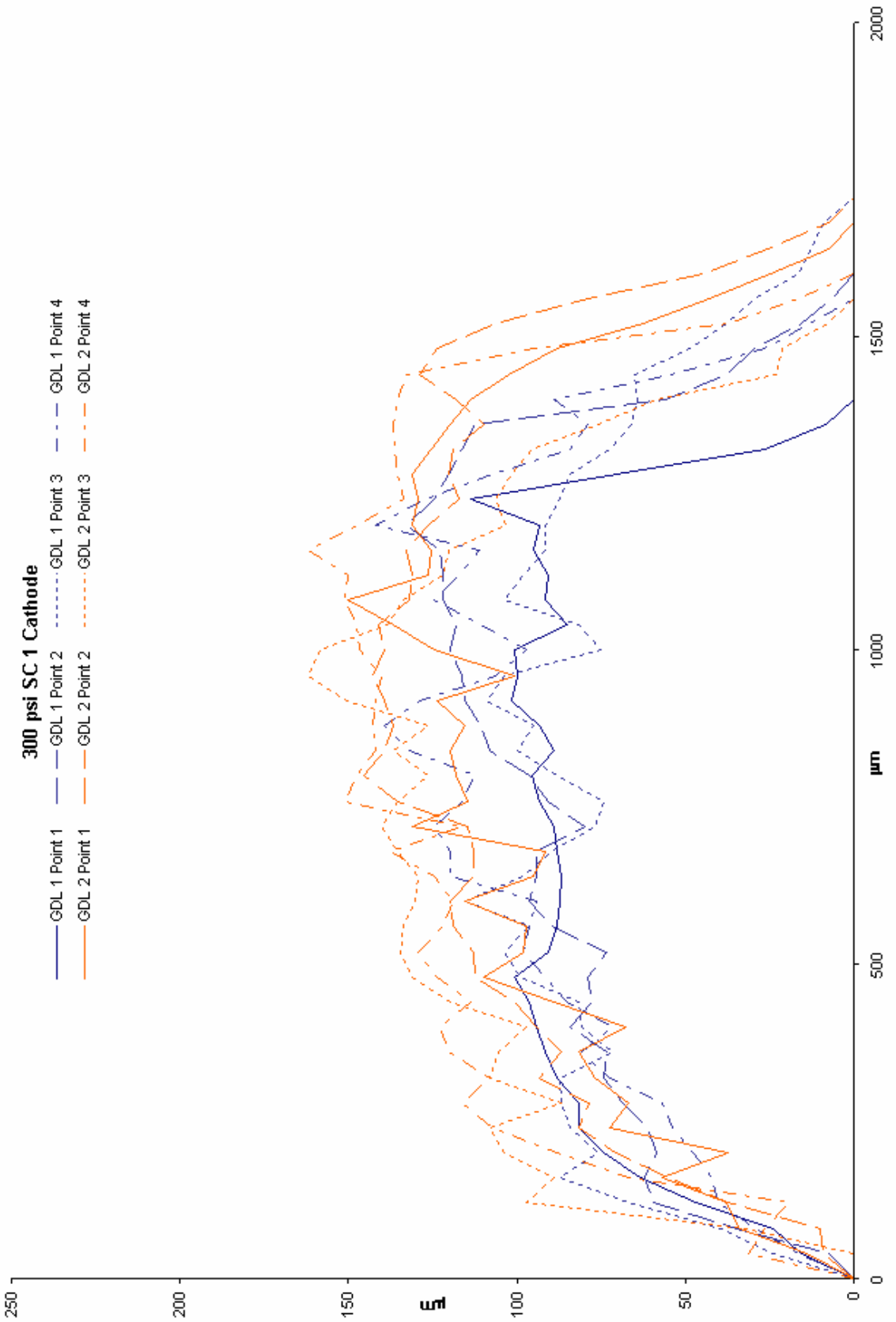

Figure 34: Impingement Data Chart 15.

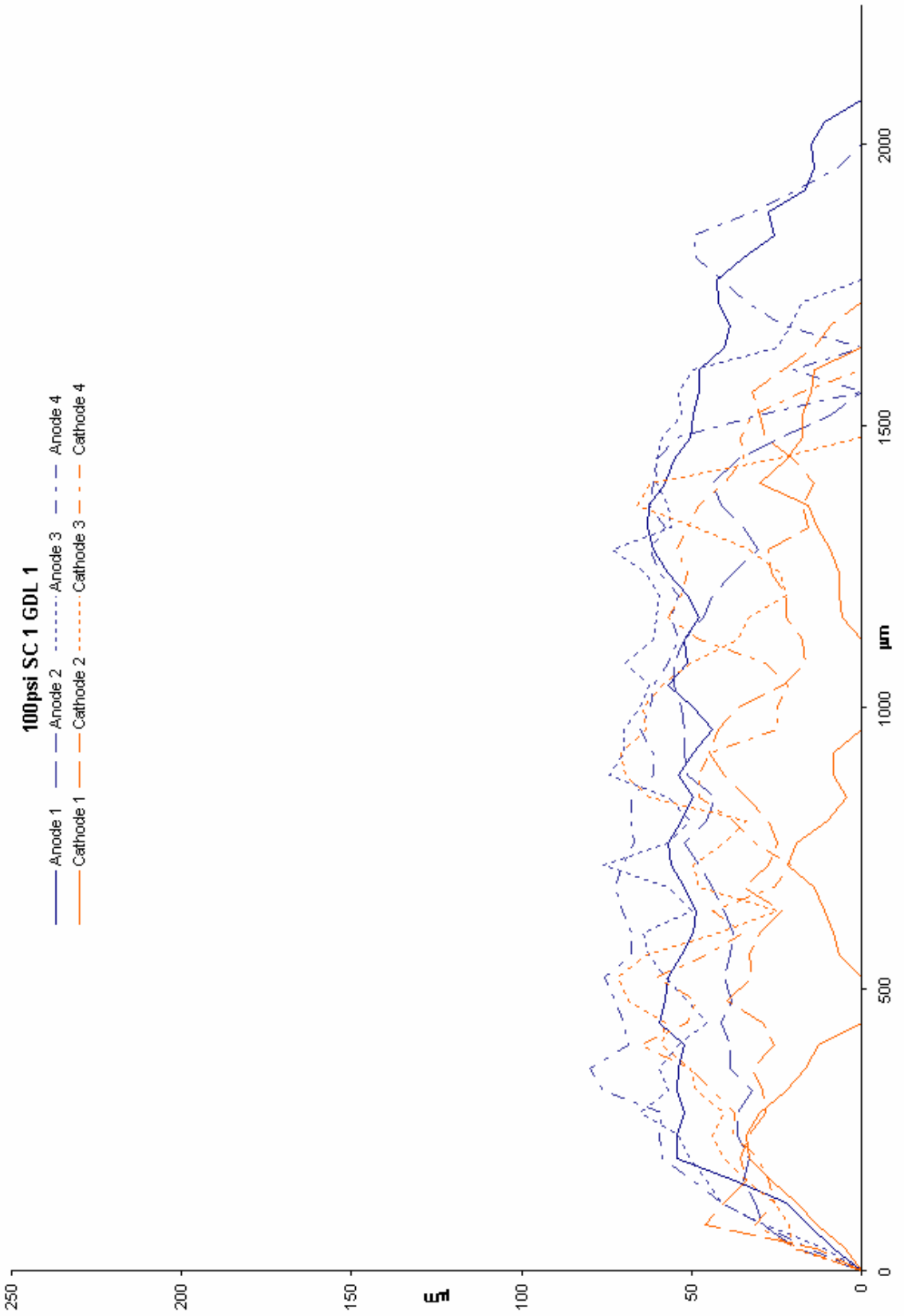

Figure 35: Impingement Data Chart 16.

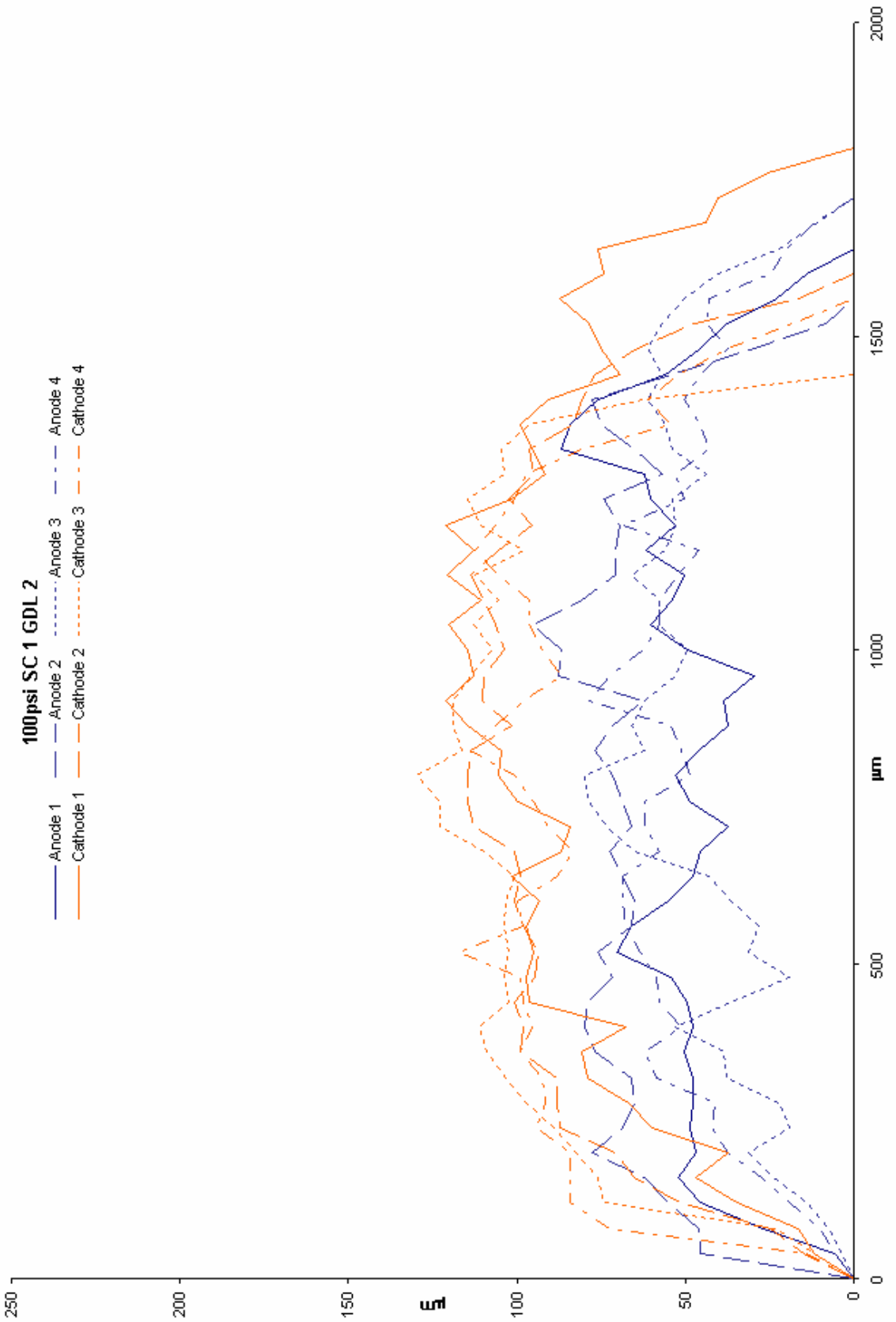

Figure 36: Impingement Data Chart 17.

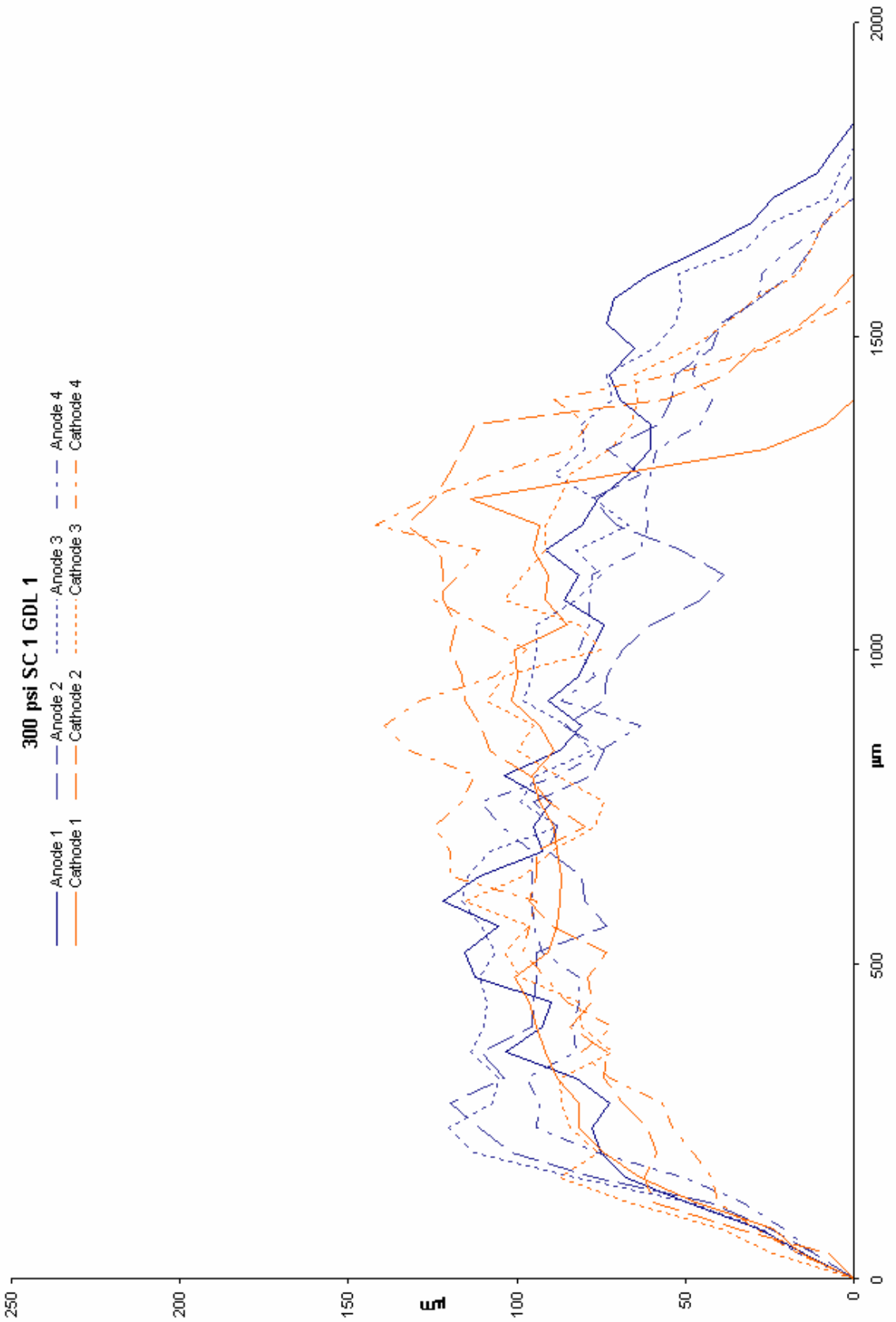

Figure 37: Impingement Data Chart 18.

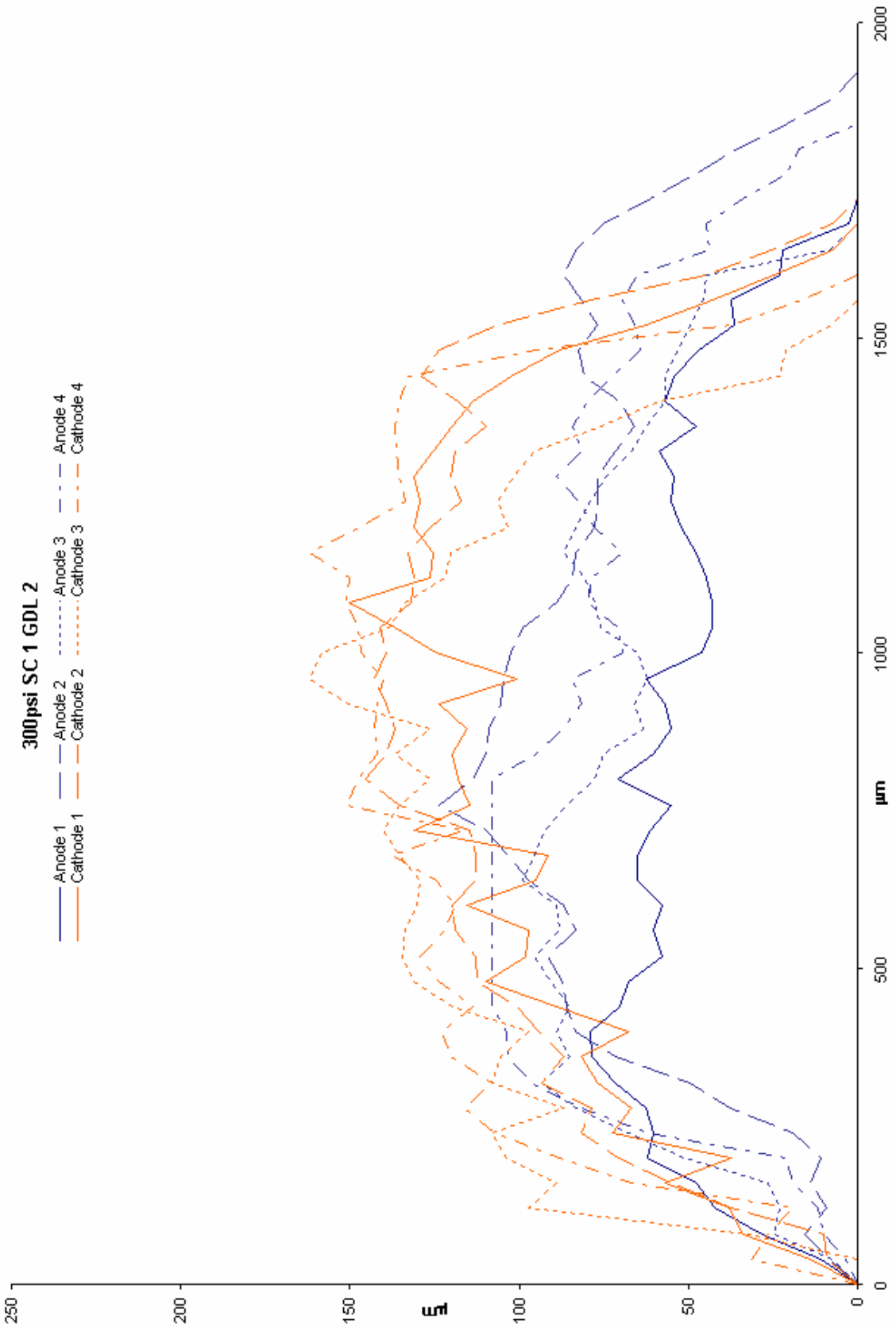

Figure 38: Impingement Data Chart 19.

Sample Configuration 2 samples have data only for anode sides of GDL-MEA setups. This is due to the orientation of the three layer setup within the samples. Cathode sides of the GDL-MEA setups were always adjacent to the perpendicularly oriented bipolar plate. This causes the cathode side of the setup to be in complete contact with the land area of the bipolar plate in the open configuration and complete non-contact in the closed position. These conditions did not allow for a point of reference for measurements thus cathode sides were not measured for impingement. Perpendicularly oriented plates were also always adjacent to the traveling side of the clamping system. Figure 39 shows a closed position in sample configuration 2. The perpendicularly oriented plate is at the top of the image. Figure 40 is an image of the open position in sample configuration 2. The closed position leaves the cathode side of the GDL with no reference point, the gas flow channel area stands between the GDL and the bipolar plate. The open position is such that the GDL is in contact with the land area of the bipolar plate along the entire edge of the cathode side.

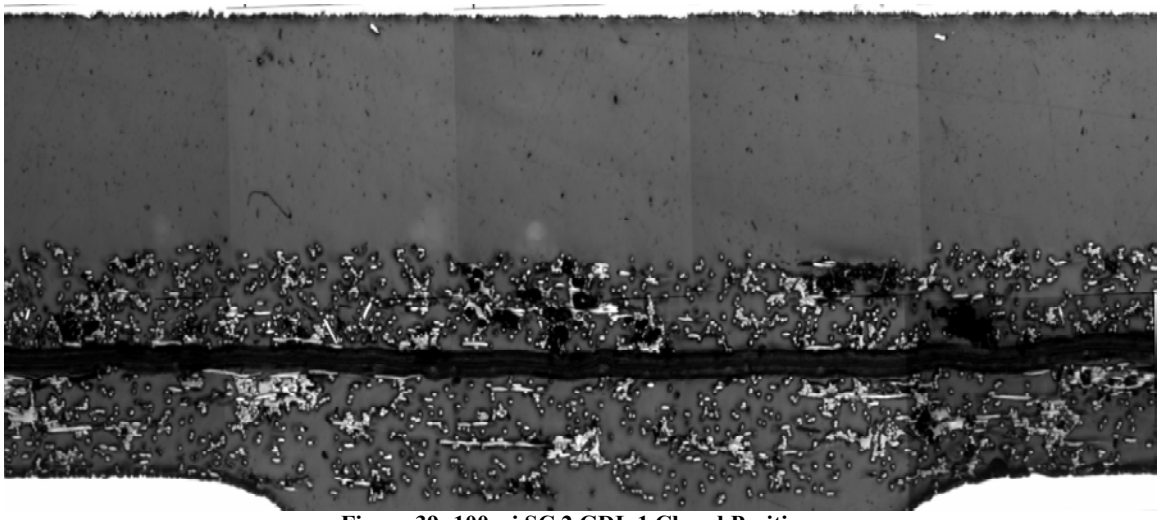

Figure 39: 100psi SC 2 GDL 1 Closed Position.

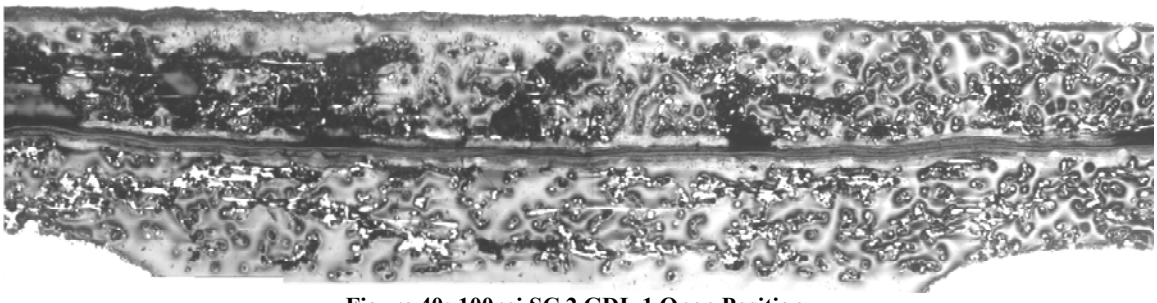

Figure 40: 100psi SC 2 GDL 1 Open Position.

In order to fully characterize SC 2 four positions must be taken into consideration, open position with channel area, open position with land area, closed position with channel area, and closed position with land area. The open and closed positions with channel area will provide information about impingement properties, open position with land area will provide information regarding thickness, and closed position with land area will provide information regarding impingement data if the proper reference point is used. Closed position with land area was not examined quantitatively in this study, open position with channel area, open position with land area, and closed position with channel area were.

Both GDL setups show similar behavior in this configuration as in SC 1. Impingement increases with increasing applied pressure. GDL 1 in the open position shows the most contrast between pressure levels. GDL 1 in the closed position follows the trend but with smaller differences in impingement. GDL 2 in both positions shows impingement for 100psi to be larger than impingement for 200psi but still less than 300psi impingement. Open positions have a larger difference in impingement than the closed positions.

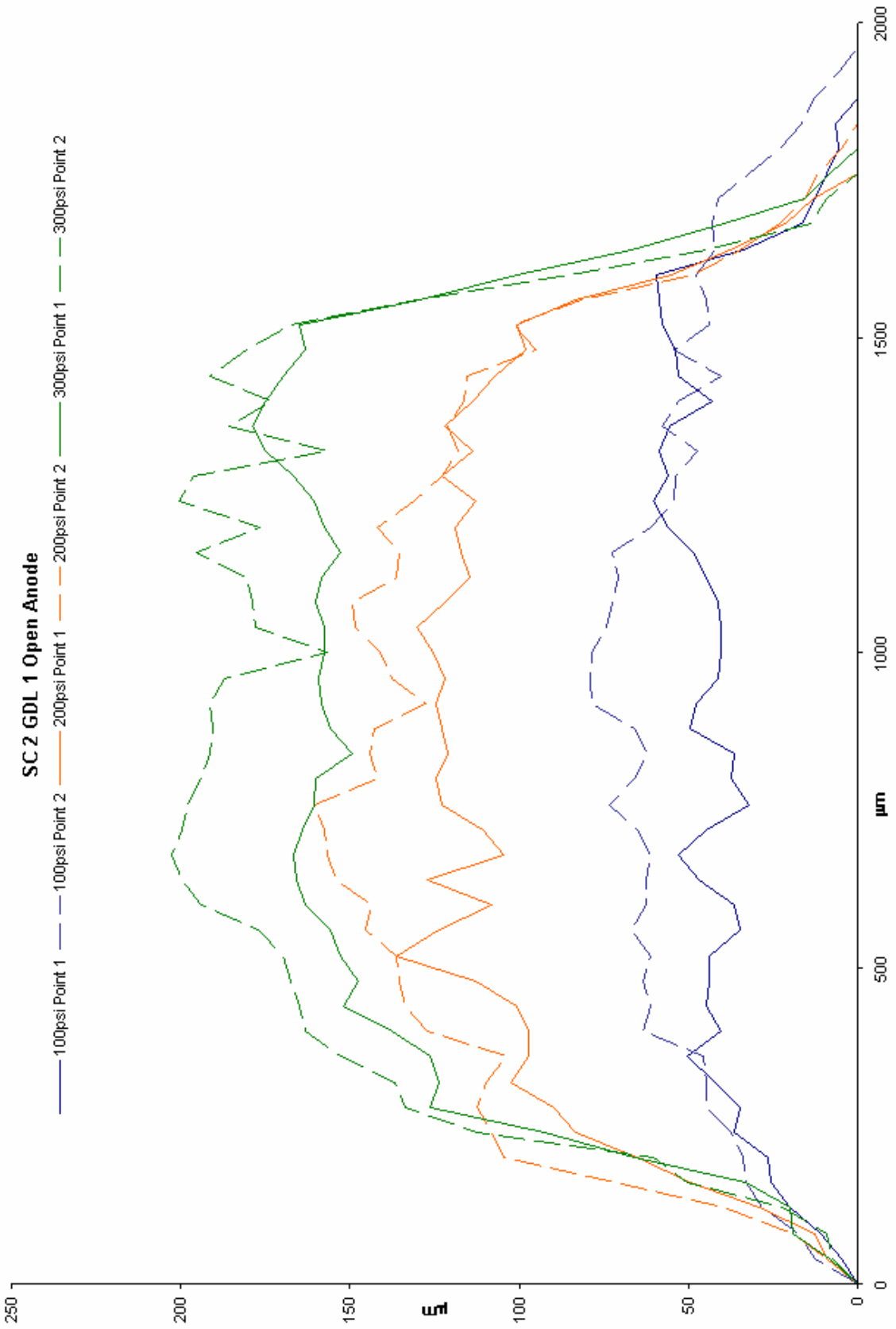

Figure 41: Impingement Data Chart 20.

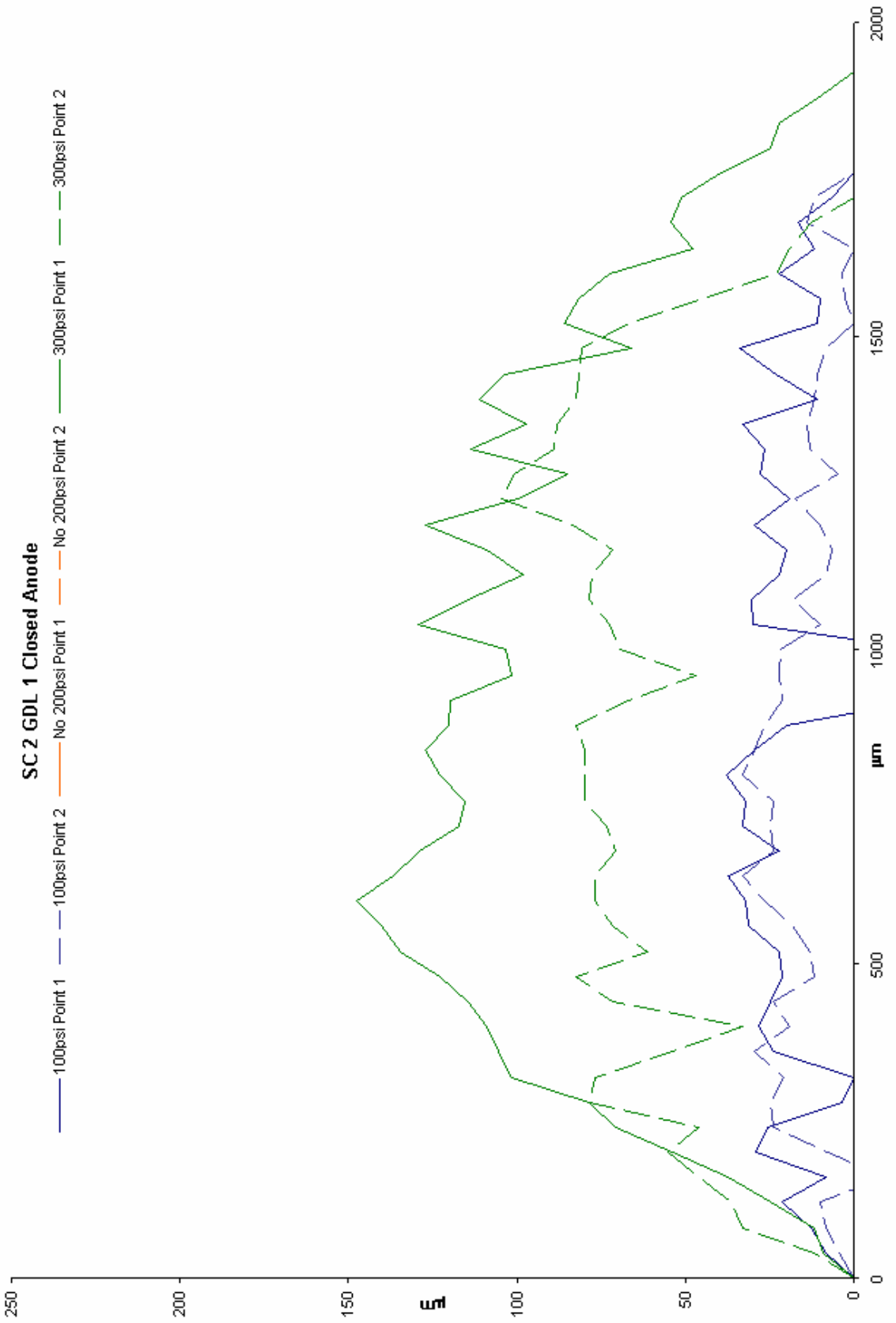

Figure 42: Impingement Data Chart 21.

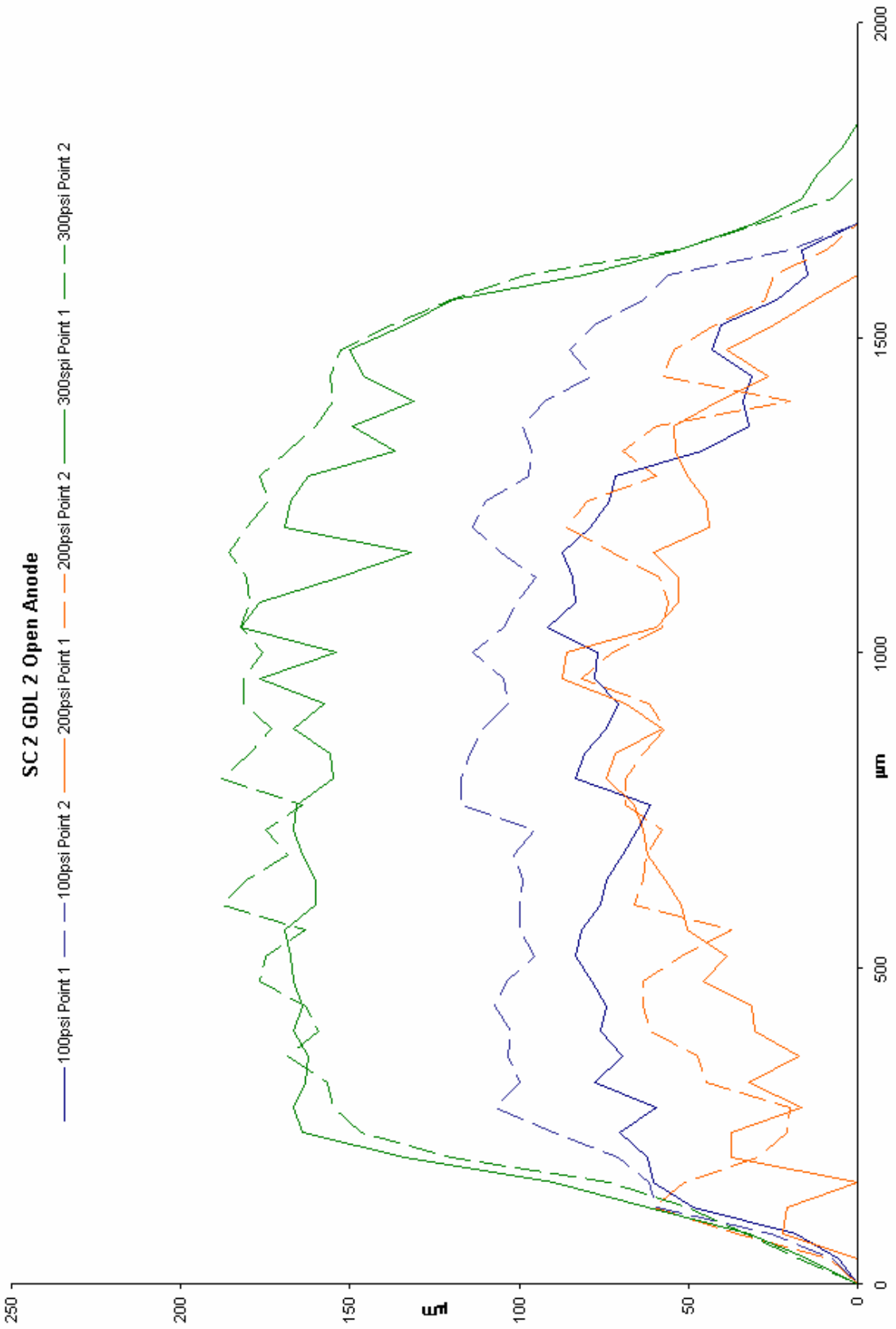

Figure 43: Impingement Data Chart 22.

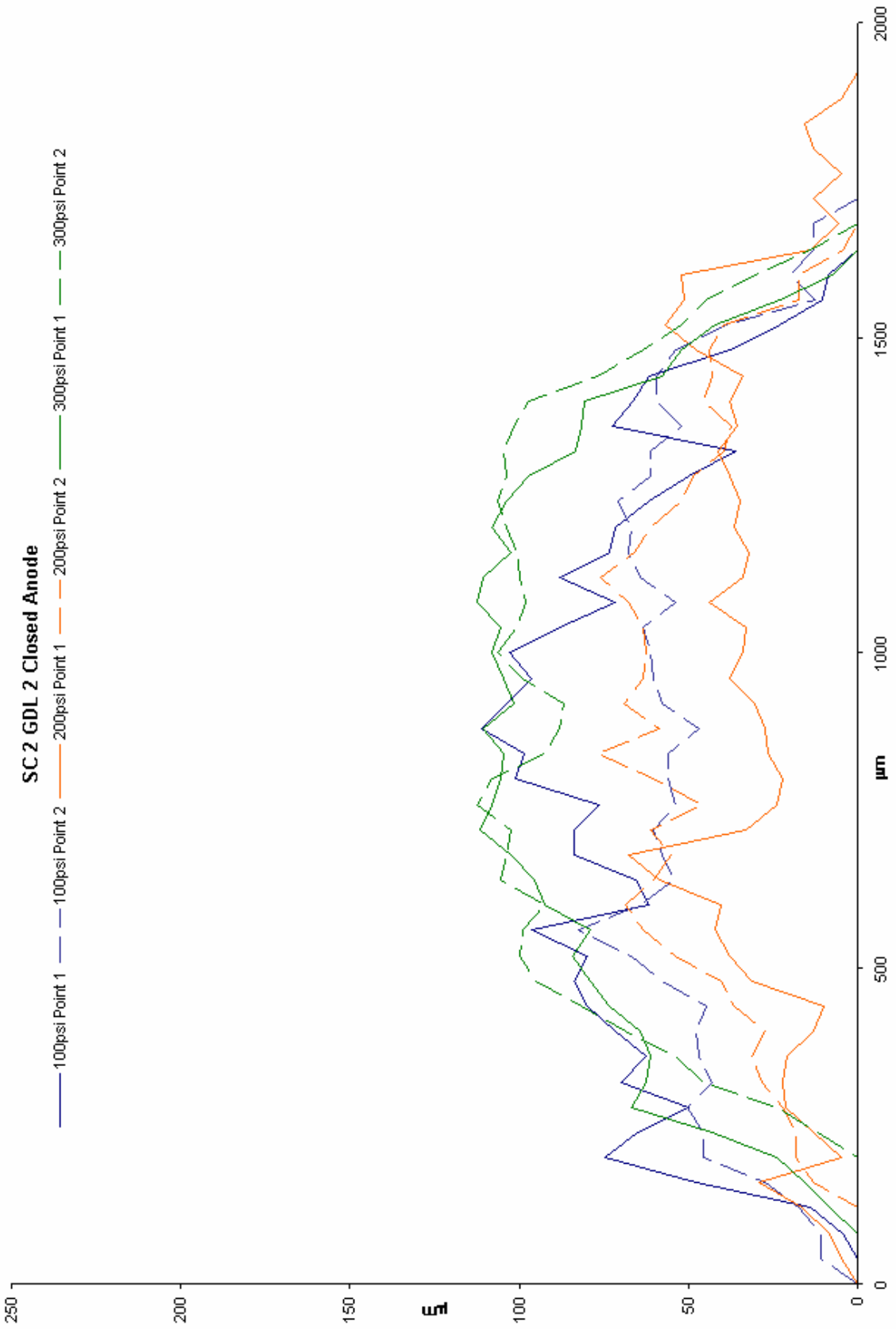

Figure 44: Impingement Data Chart 23.

Figures 45 to 48 show the differences in impingements between the two sets of GDL materials for SC 2. GDL 2 shows larger impingements than GDL 1 in both positions at low loads, at high loads there are only very small differences in impingement between the two sets of GDL material. There tends to be a larger distribution of points for GDL 1 at higher pressure levels. At lower pressure levels the point distribution for GDL 1 looks almost the same as for GDL 2. This tells us that in this sample configuration GDL 1 and GDL 2 react differently up to a certain load level, at which point they start to react in almost the same manner with only slight differences.

Figures 49 to 52 show the differences between behavior of anode sides of GDL 1 and 2 in the open and closed positions. Figures 49 and 50 show a small difference in GDL behavior between open and closed positions with a small applied pressure while Figures 51 and 52 show a large difference in GDL behavior between open and closed positions with a large applied pressure. This behavior might be due to similarities in pore volumes within the layers but differences in fiber packing.

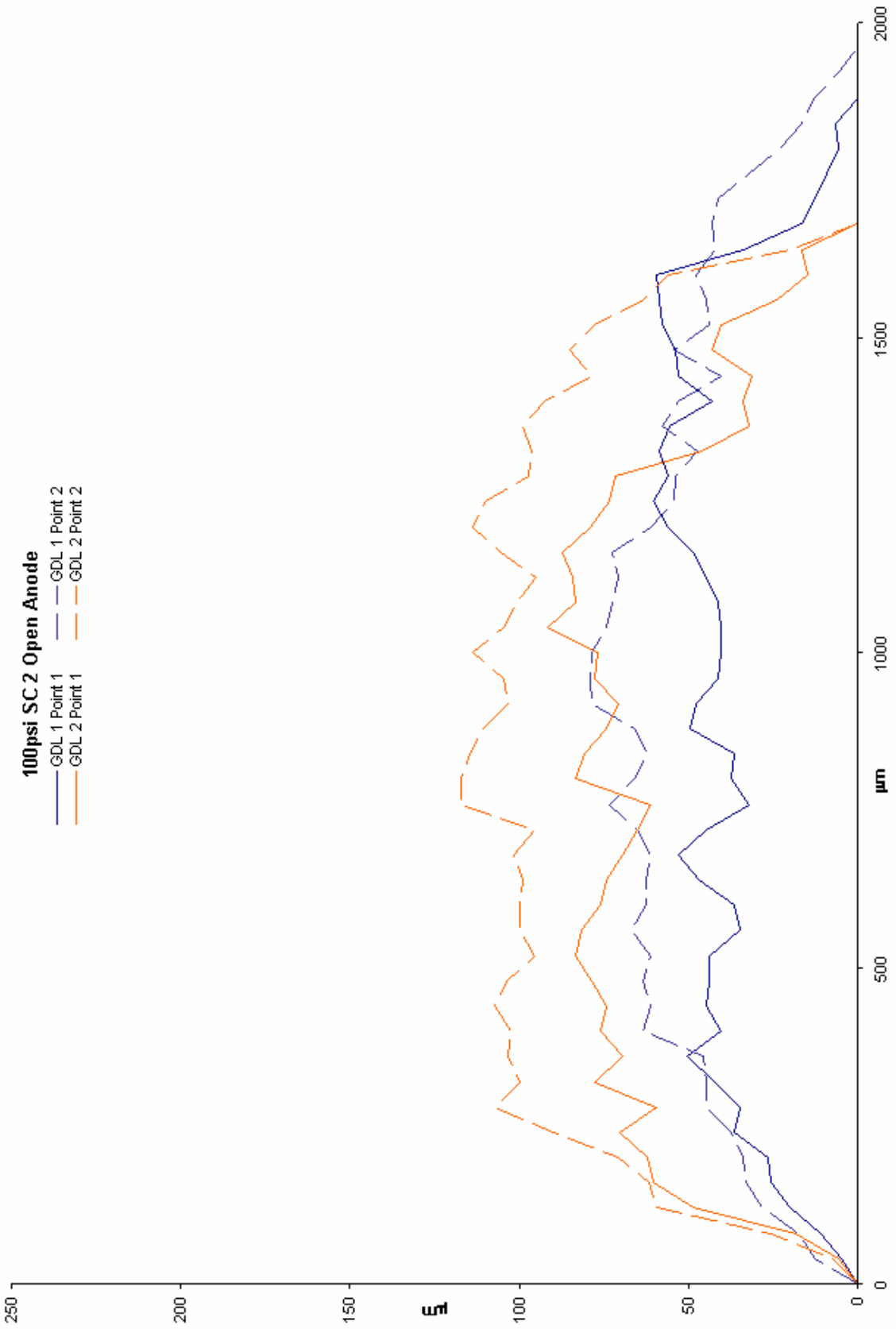

Figure 45: Impingement Data Chart 24.

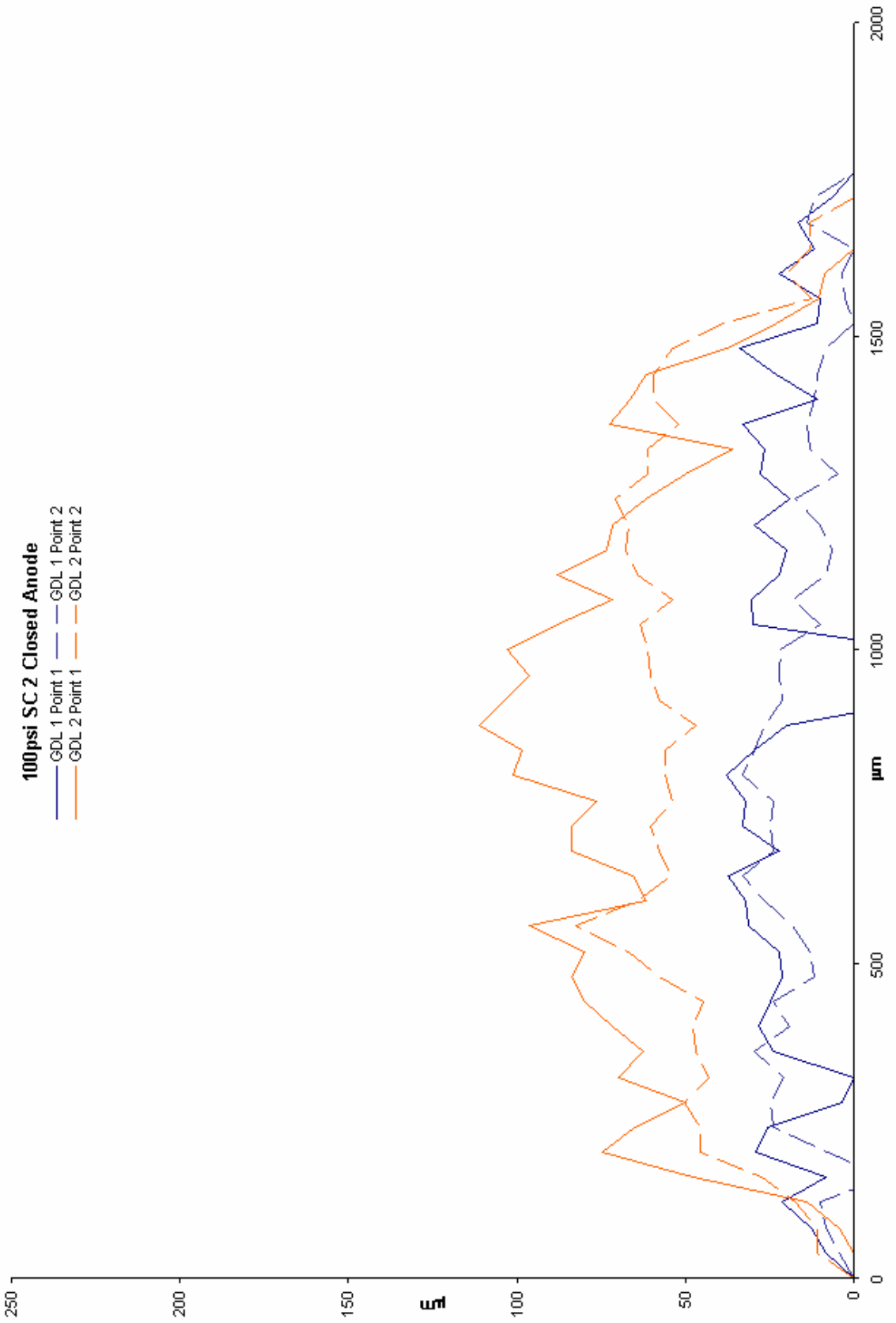

Figure 46: Impingement Data Chart 25.

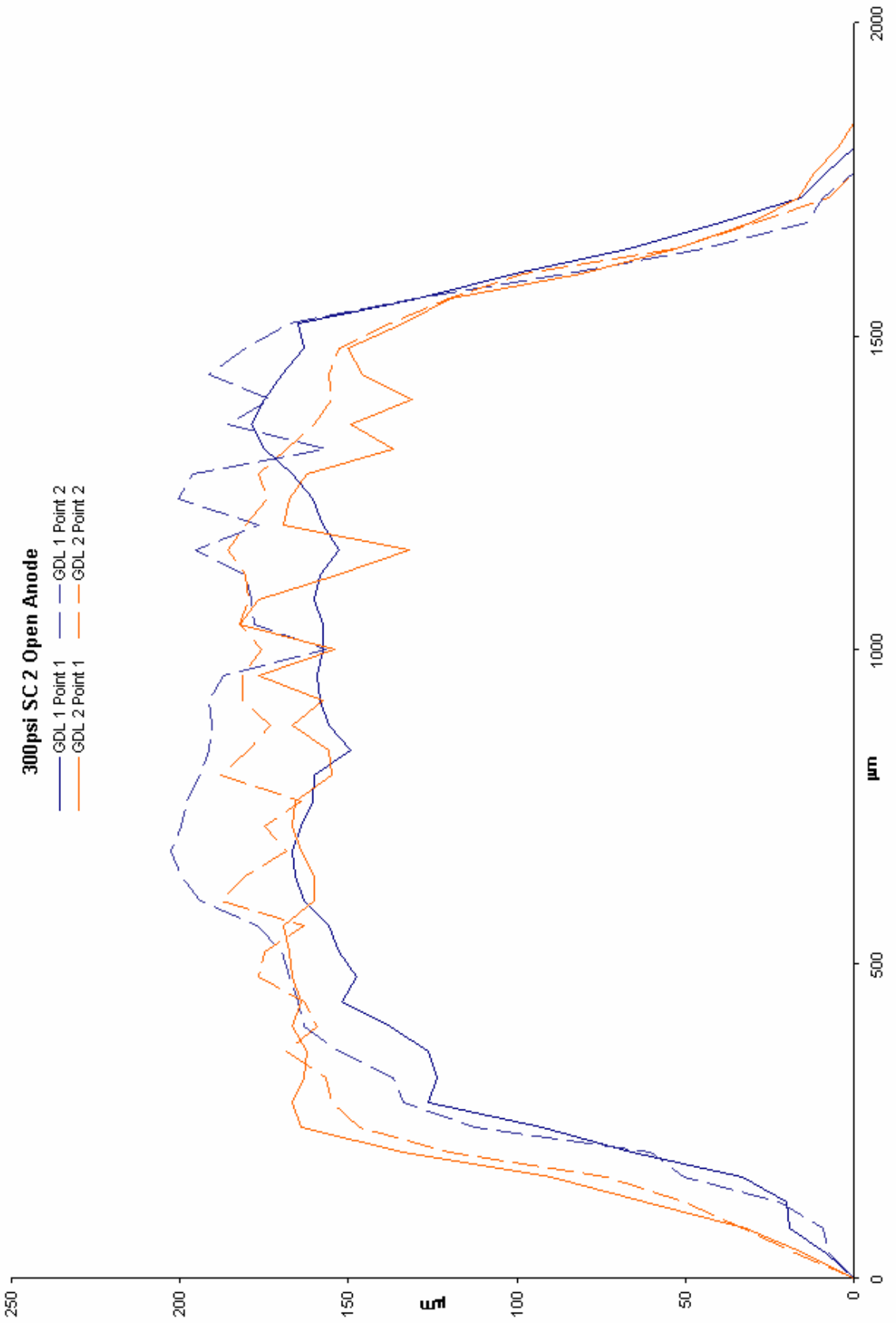

Figure 47: Impingement Data Chart 26.

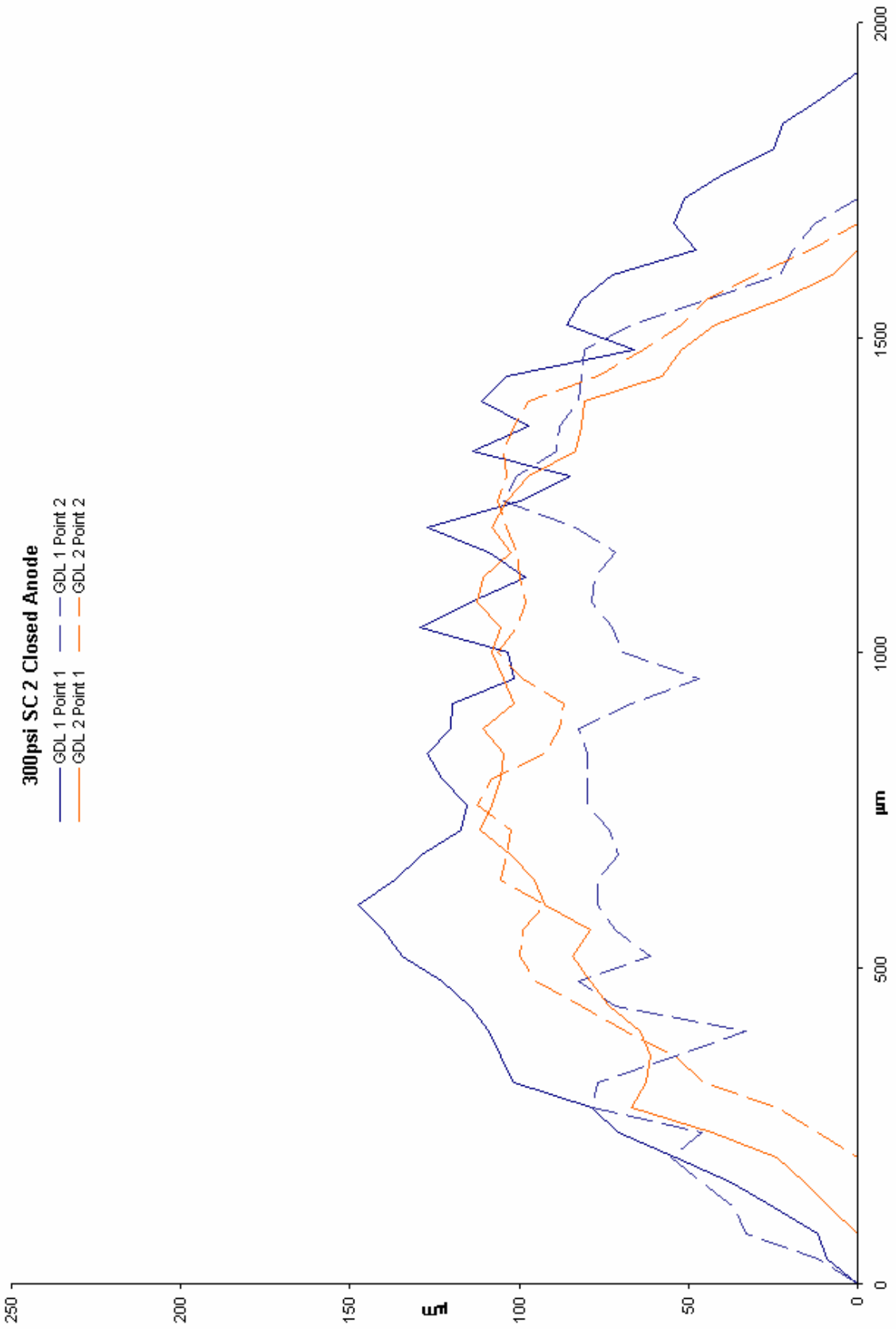

Figure 48: Impingement Data Chart 27.

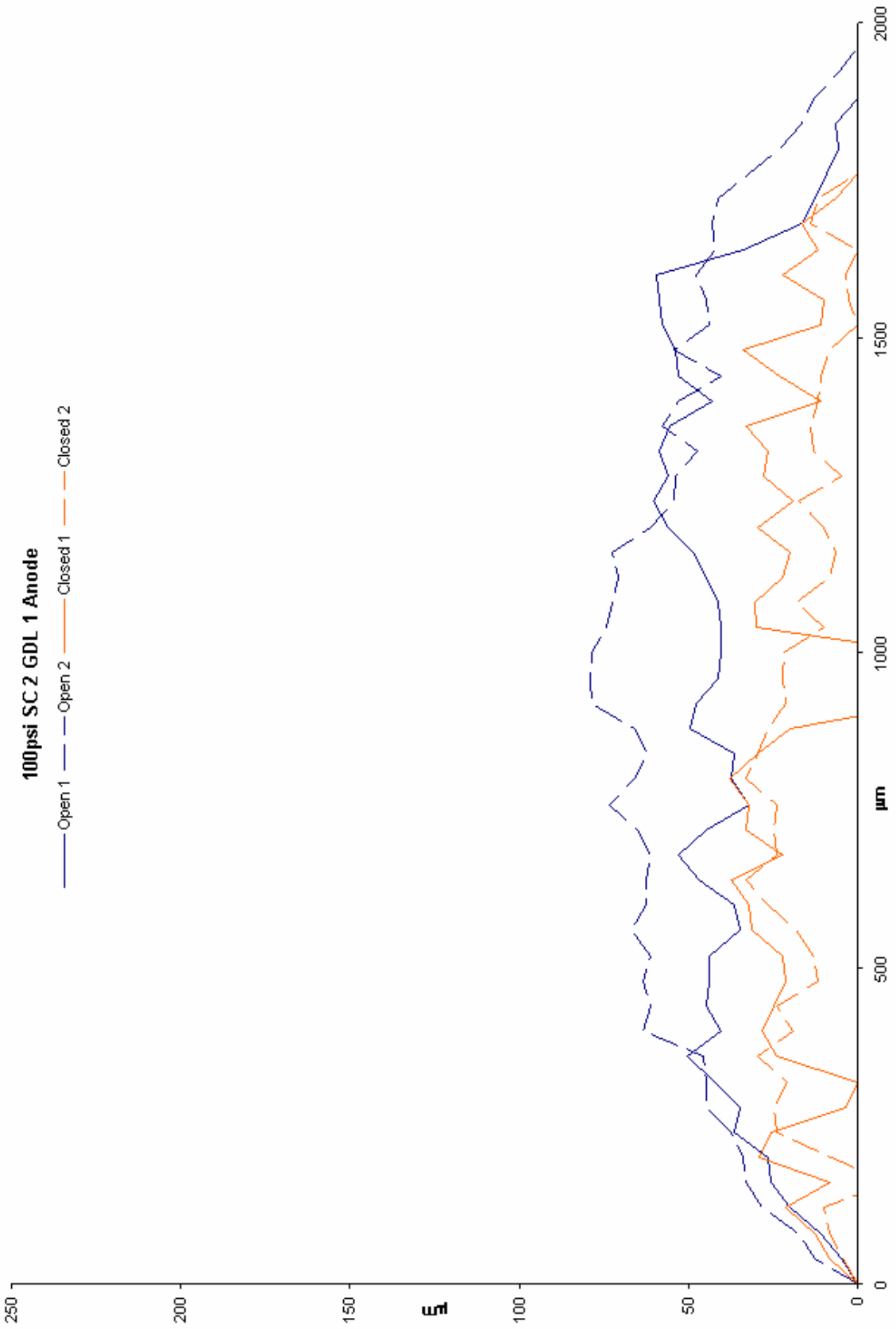

Figure 49: Impingement Data Chart 28.

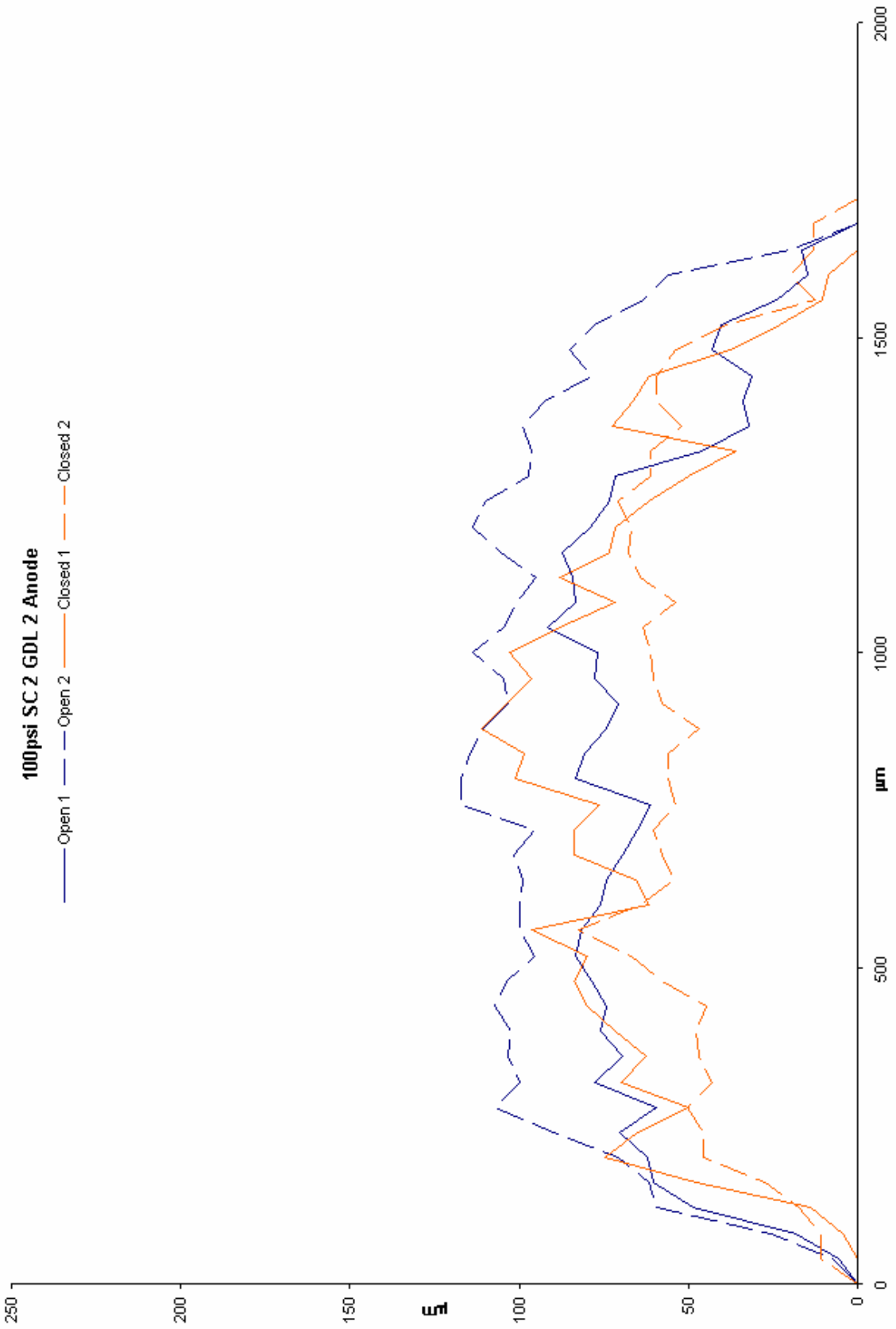

Figure 50: Impingement Data Chart 29.

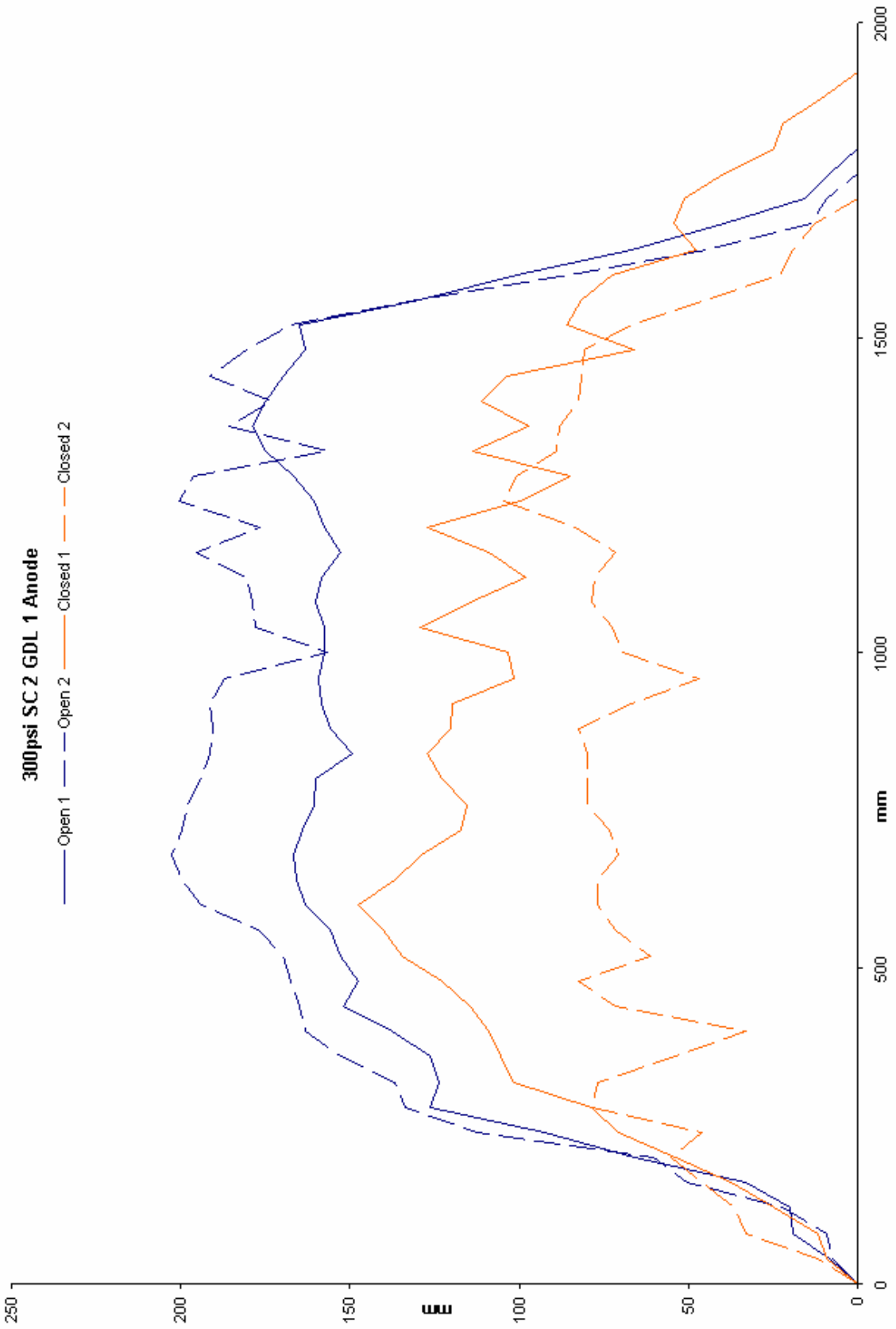

Figure 51: Impingement Data Chart 30.

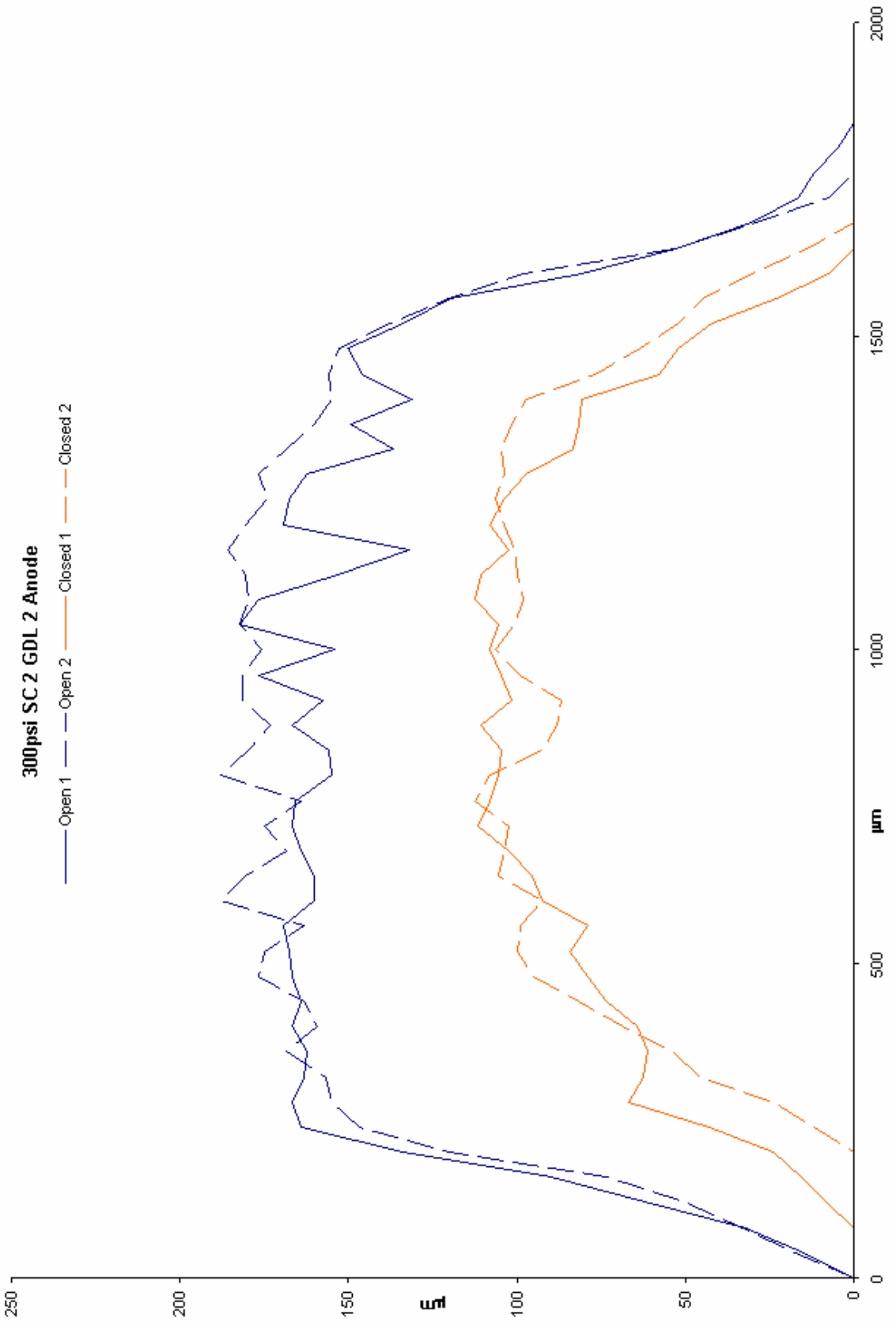

Figure 52: Impingement Data Chart 31.

Sample configuration 3 is an offset parallel channel arrangement of the bipolar plates in each sample. Misalignment of bipolar plates will occur and should be quantified, however that is beyond the scope of this project. Sample configuration 3 was analyzed qualitatively only. No reference point for measurement has been yet set for this sample configuration and thus there is no quantitative data included.

SC 3 samples demonstrate a large amount of deformation in both the bipolar plates and gas diffusion materials. Figure 53 below is a series of images taken at 100x magnification of GDL 2 at 300psi and arranged in series. Breakage has occurred in the GDL materials and there is possible breakage in the MEA layer as well. Bipolar plates on both sides of the cell have deformed drastically. When compared to Figure 56 of an SC 3 sample of GDL 2 at 200psi it is clear how much deformation has occurred in the 300psi samples.

Figures 53 and 54 show that degree of misalignment has an affect on deformation of bipolar plates. Since GDL materials tend to conform to the bipolar plates GDL deformation is also affected by degree of misalignment. Both images show breakage in both sides of GDL material but GDL 2 has deformed more due to the added misalignment of the bipolar plates. Figure 55 shows a 200x image of GDL 2 at the breakage point. It is clear that the fibers have broken from the sharp turn in the edge of the paper.

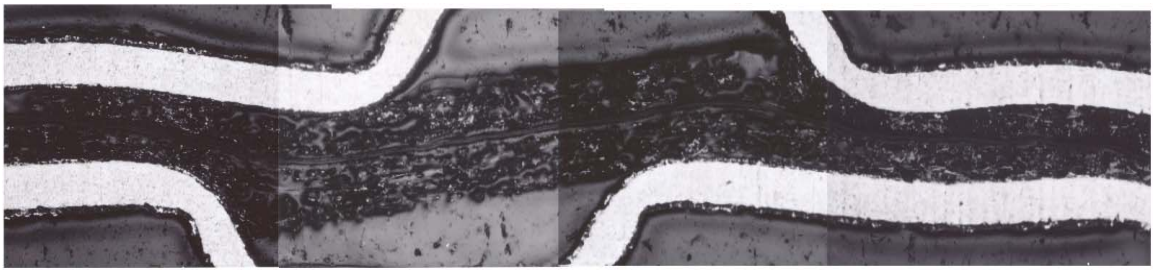

Figure 53: SC 3, GDL 1 Loaded to 300psi.

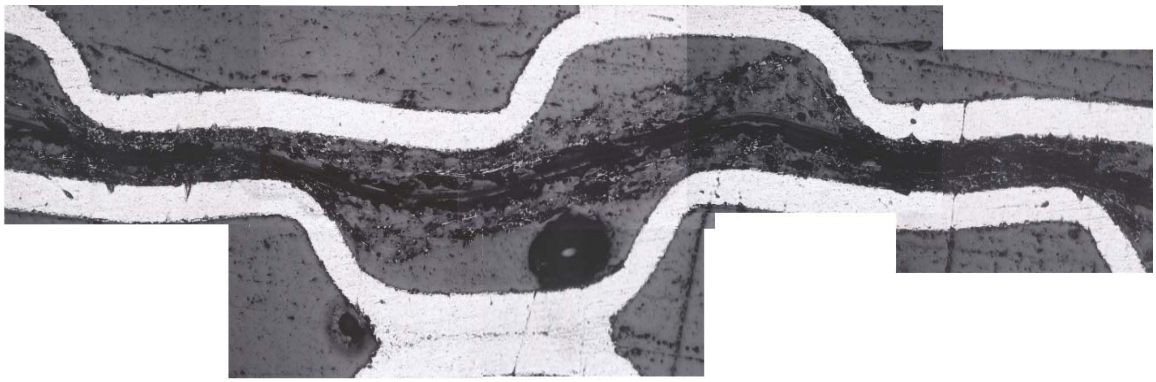

Figure 54: SC 3, GDL 2 Loaded to 300psi.

Figure 55: 200x, Broken GDL 2 at 300psi.

Figure 56: 200psi SC 3 GDL 2.

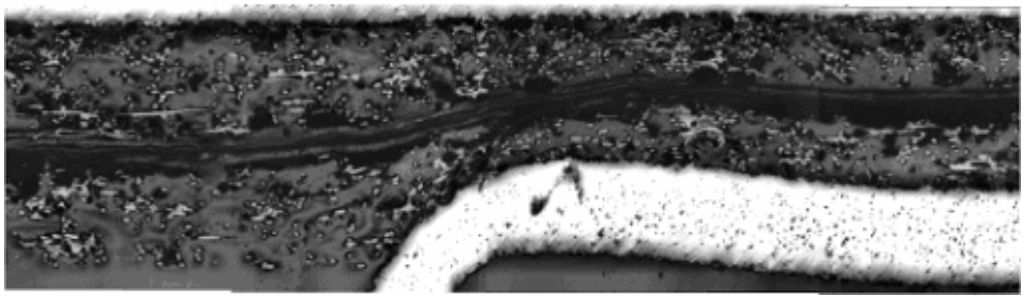

Figure 57: SC 2 300psi GDL 2.

Clearly misalignment of bipolar plates will cause more deformation under load than aligned samples. This type of deformation is seen in sample configuration 2 at 300psi in the open configuration (Figure 56) but the extent of the deformation is much less than in the misaligned samples. Here the GDL materials are not broken on both sides, only deformed. Deformation is much less in the cathode side of the GDL (the top side of the GDL). We see this because of the angle that the edge of the material makes with the bipolar plate, when compared to Figure 55 it is apparent. The anode side bipolar plate is deformed but the cathode side bipolar plate is not. The straight edge of the perpendicular plate is not deformed.

Conclusion

Gas diffusion layer material analyzed had a large volume of open pores and voids which dictated the properties of the layers themselves as well as the one cell setup. Impingement of these layers into gas flow channels increased with increasing applied pressure. Cathode side impingement tended to be larger than anode side impingement for sample configurations 1 and 2 overall. This may be due to the cathode side always being adjacent to the traveling side of the clamping system. Gas diffusion layer set 1 tended to show smaller impingement into the gas flow channels than gas diffusion layer set 2 for both sample configuration 1 and 2.

Sample configuration 3 and preliminary testing confirmed that a pressure limit to an individual cell exists and alignment is a very important factor in a cell setup. The pressure limit is characterized by failure caused by breakage of the gas diffusion layer and membrane electrode assembly and distortion of the bipolar plates. 400psi is clearly past the pressure limit while 300psi is just over the limit. Some 200psi samples showed deformation of the bipolar plates while others showed no signs of failure from the above mechanisms. Alignment is crucial to proper function of the cell and the stack. This can be seen in the images of the misaligned samples. Deformation of the bipolar plates is much more likely in misaligned samples and thus the infrastructure of the fuel cell stack is compromised. This may have damaging effects to the performance of the assembly. Misaligned samples at 300psi show breakage of the gas diffusion materials while aligned samples at the same pressure showed no signs of breakage only deformation.

Appendix A

Table 6: Clamp Plate Parallel Measurement Data.

Pressure (psi)	GDL #	Sample Configuration	Measurement (cm)		Pressure (psi)	GDL #	Sample Configuration	Measurement (cm)
100	1	parallel	1.559179		100	2	parallel	1.559179
			1.559179					1.559306
			1.559306					1.559306
			1.559179					1.559306
200	1	parallel	1.55194		200	2	parallel	1.552321
			1.55194					1.552321
			1.55194					1.552448
			1.552067					1.552321
300	1	parallel	1.544574		300	2	parallel	1.544701
			1.544701					1.544701
			1.544574					1.544701
			1.544574					1.544701
100	1	perpendicular	1.558925		100	2	perpendicular	1.561211
			1.558798					1.561211
			1.558925					1.561338
			1.558798					1.561211
200	1	perpendicular	1.552448		200	2	perpendicular	1.54459
			1.552321					1.54459
			1.552448					1.54459
			1.552194					1.54459
300	1	perpendicular	1.54432		300	2	perpendicular	1.543812
			1.544447					1.544066
			1.544447					1.544066
			1.544447					1.543939
100	1	offset	1.560576		100	2	offset	1.5621
			1.560449					1.5621
			1.560322					1.5621
			1.560449					1.5621
200	1	offset	1.552448		200	2	offset	1.551686
			1.552702					1.551813
			1.552702					1.55194
			1.552575					1.551813
300	1	offset	1.539113		300	2	offset	1.538097
			1.53924					1.53797
			1.53924					1.537335
			1.53924					1.537843

Appendix B

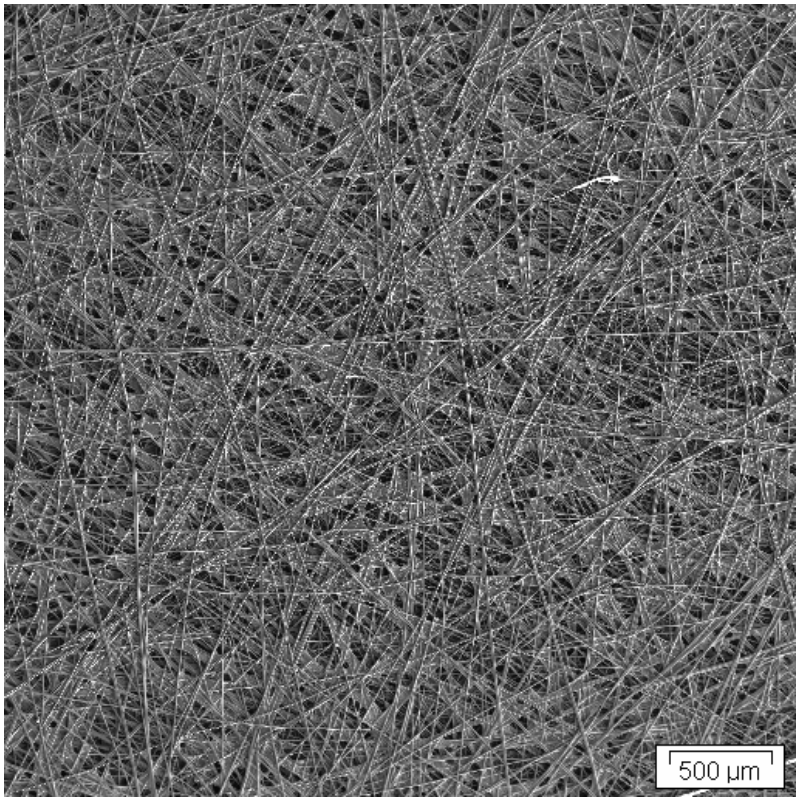

Figure 58: GDL 1 Anode Side 1 20x.

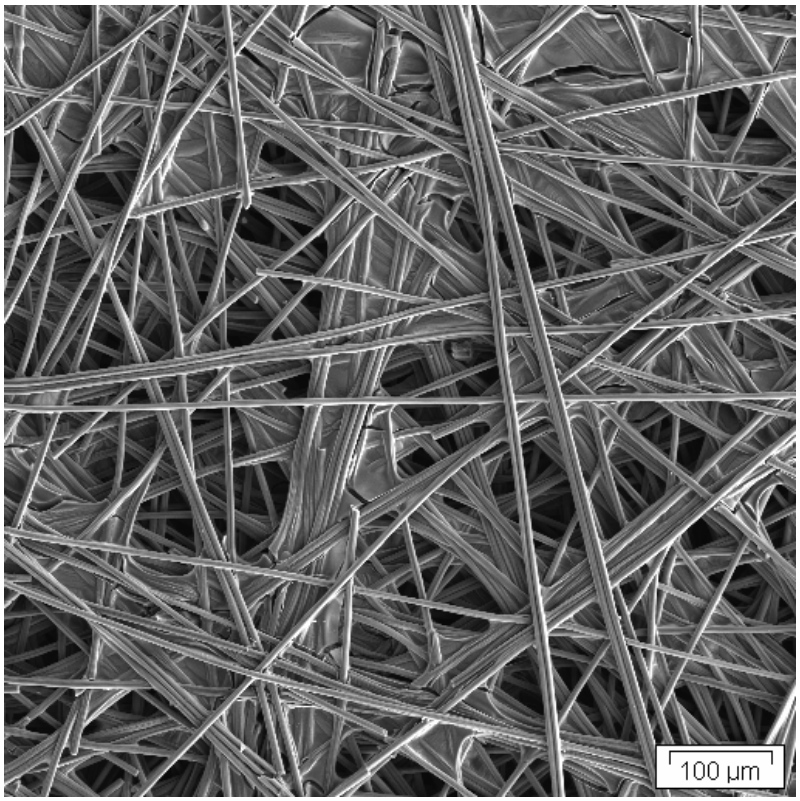

Figure 59: GDL 1 Anode Side 1 100x.

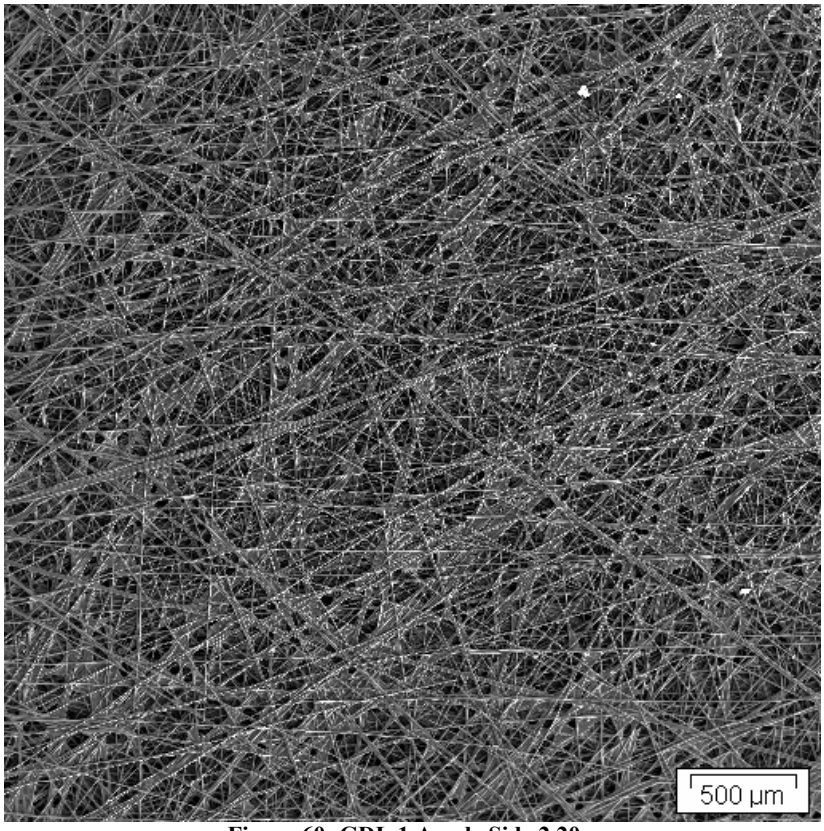

Figure 60: GDL 1 Anode Side 2 20x.

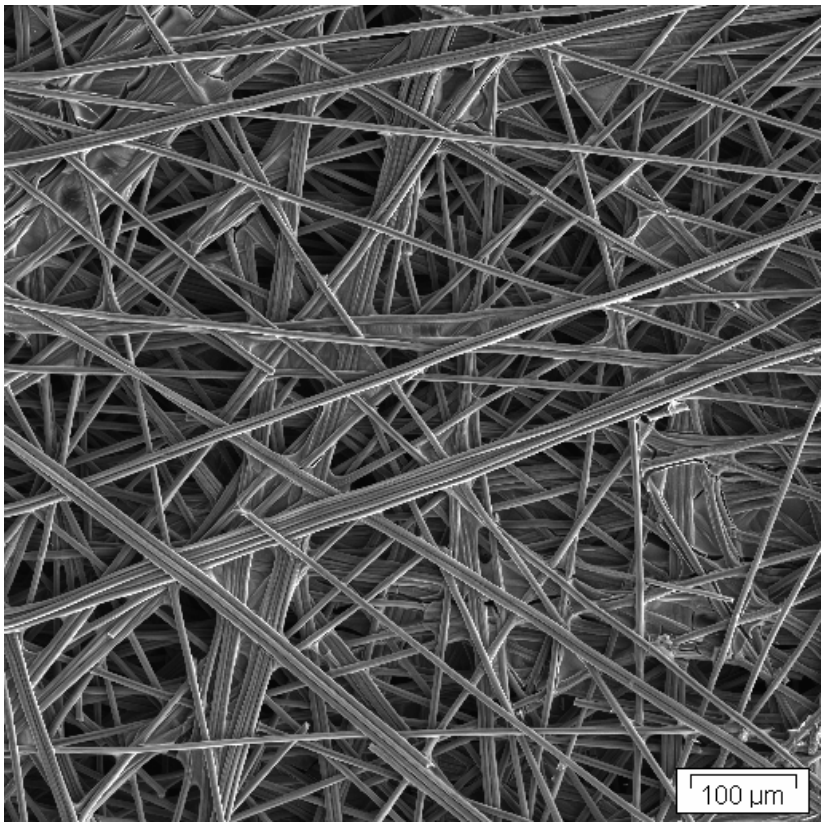

Figure 61: GDL 1 Anode Side 2 100x.

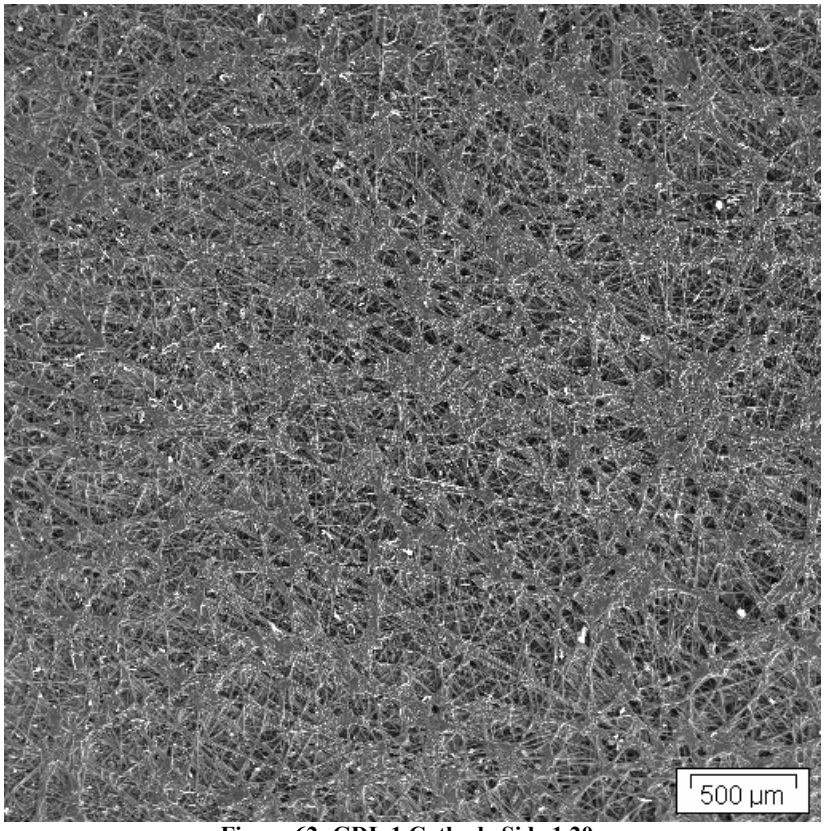

Figure 62: GDL 1 Cathode Side 1 20x

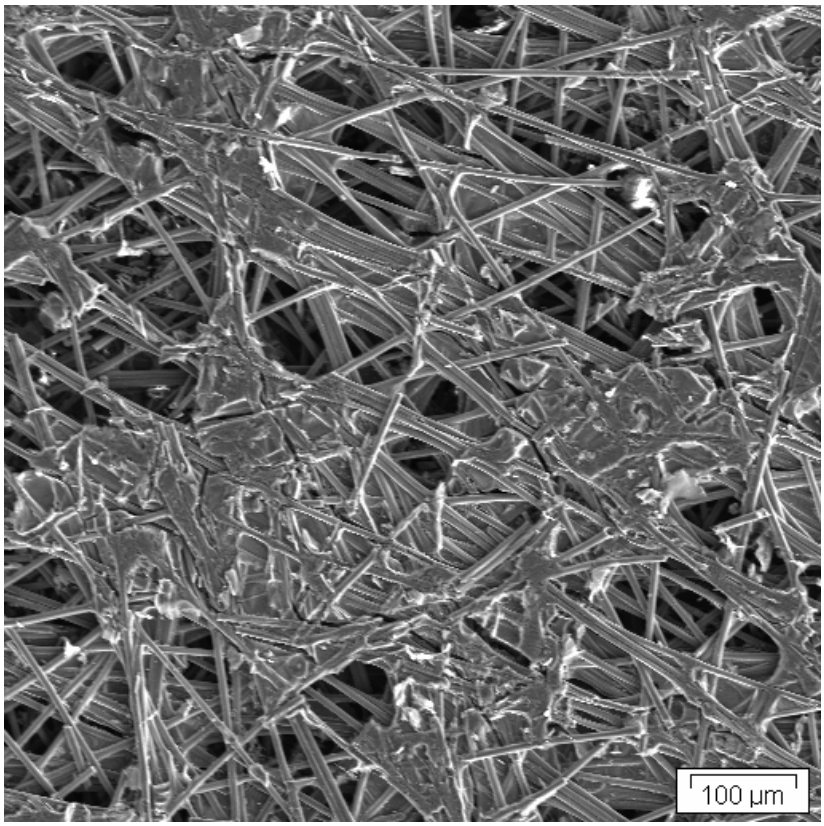

Figure 63: GDL 1 Cathode Side 1 100x.

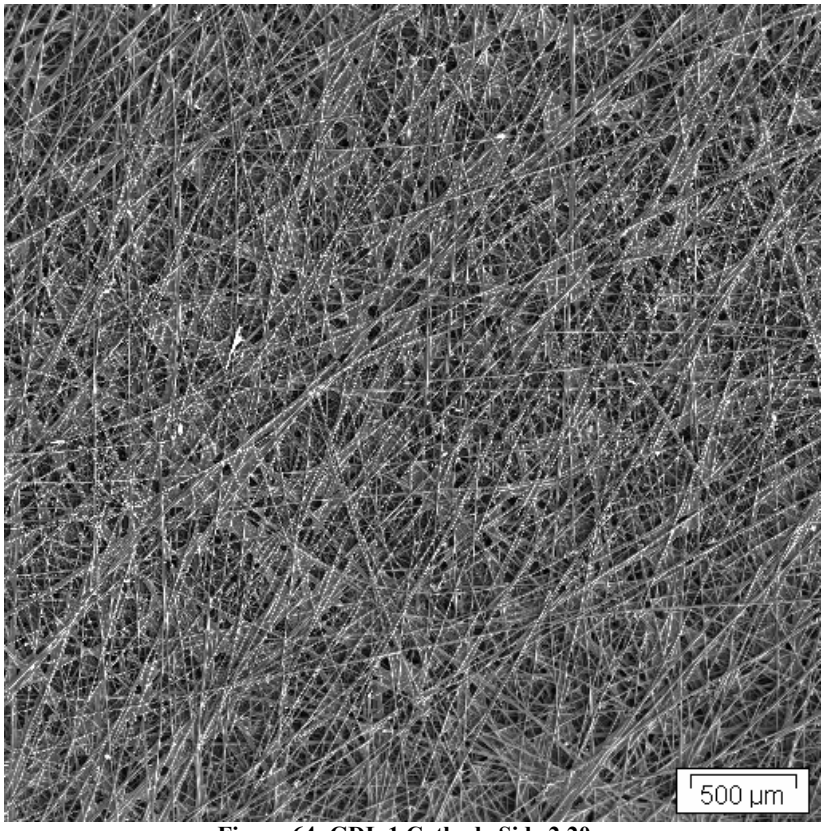

Figure 64: GDL 1 Cathode Side 2 20x.

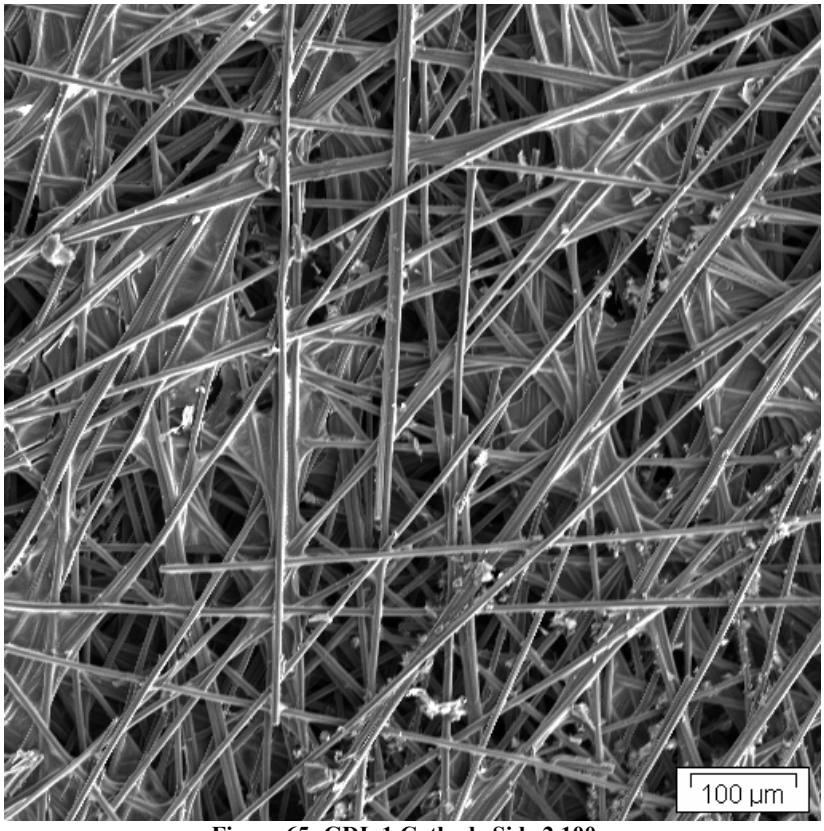

Figure 65: GDL 1 Cathode Side 2 100x.

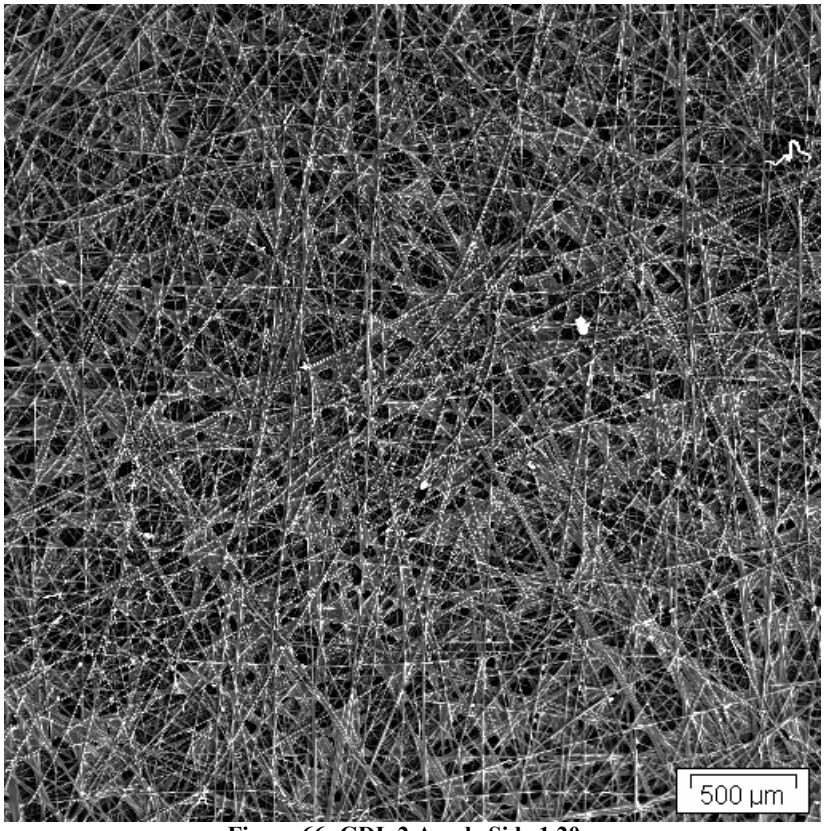

Figure 66: GDL 2 Anode Side 1 20x.

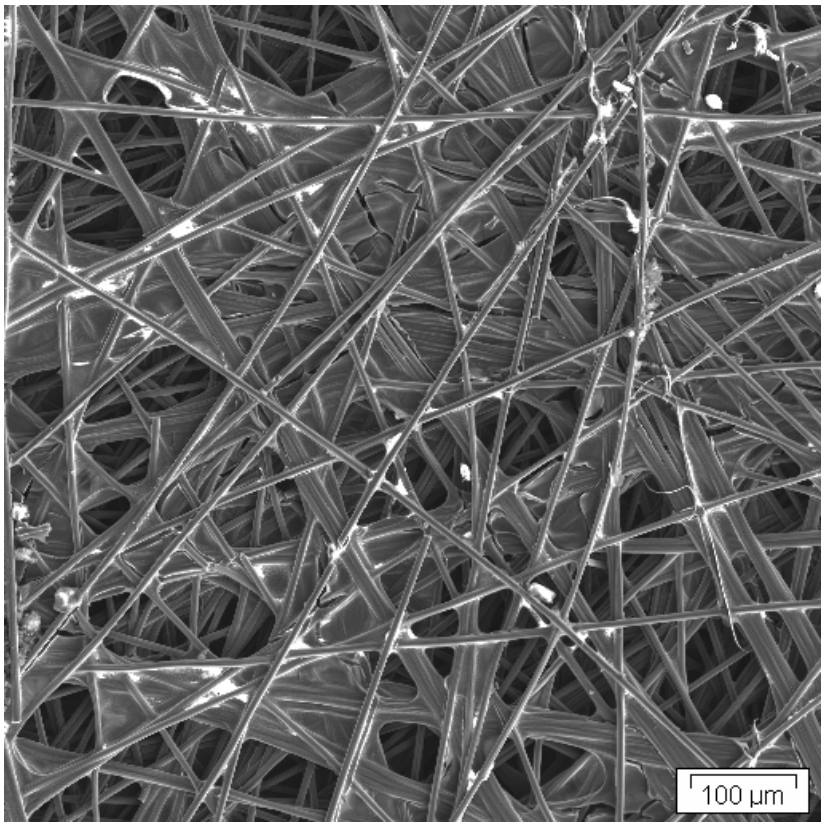

Figure 67: GDL 2 Anode Side 1 100x.

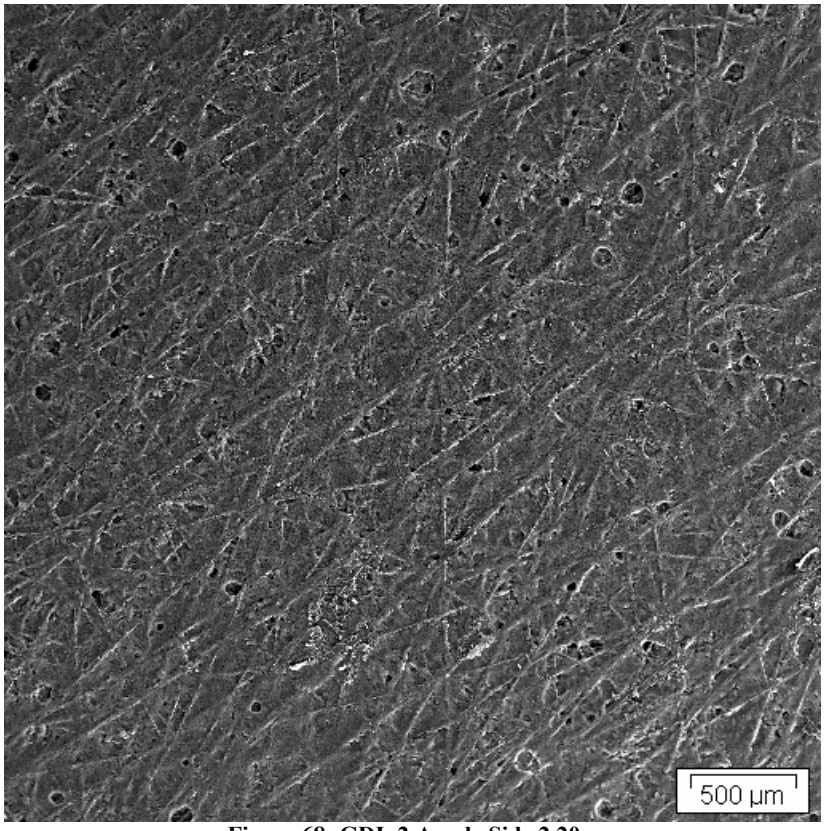

Figure 68: GDL 2 Anode Side 2 20x.

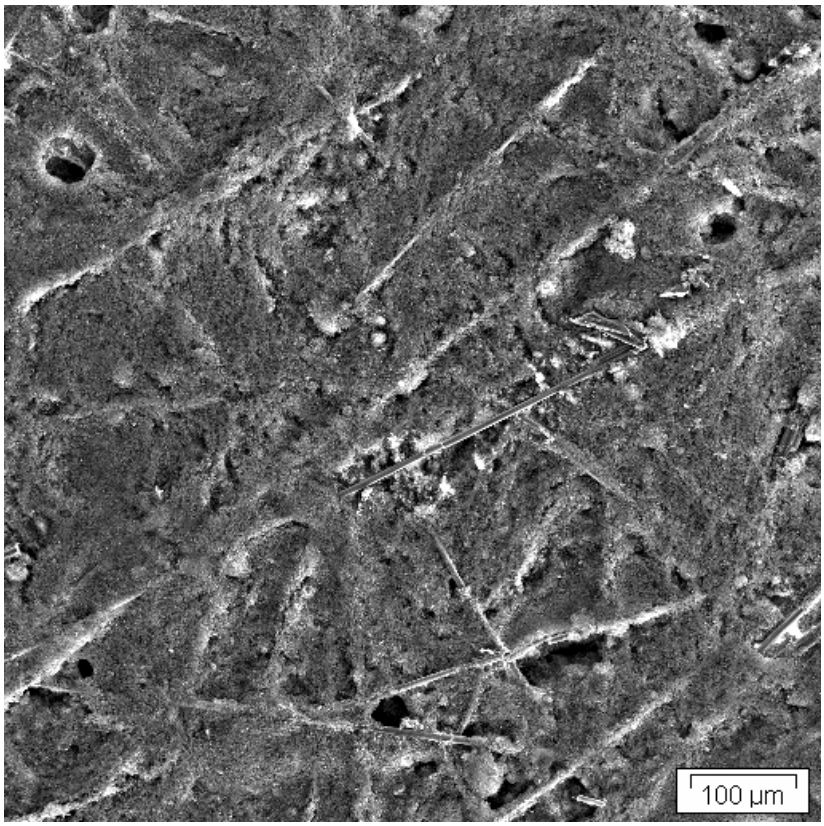

Figure 69: GDL 2 Anode Side 2 100x.

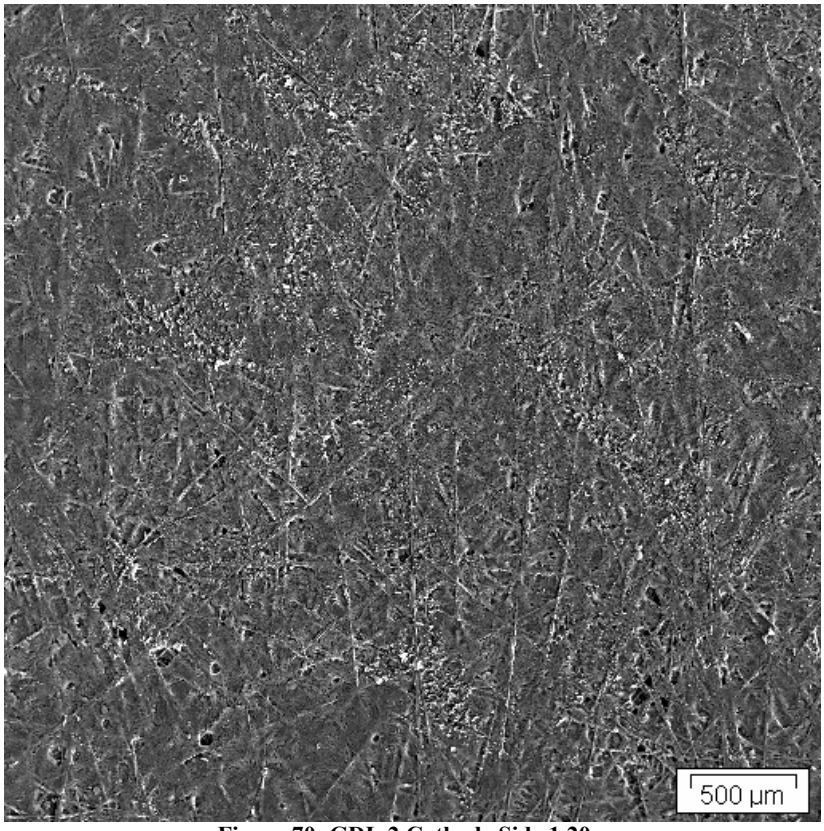

Figure 70: GDL 2 Cathode Side 1 20x.

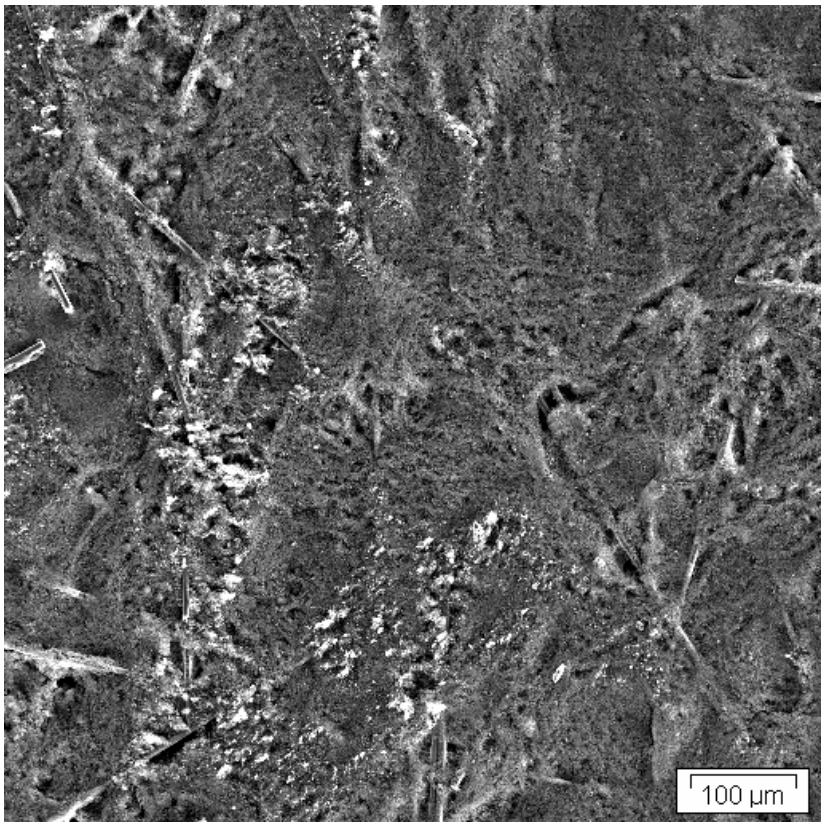

Figure 71: GDL 2 Cathode Side 1 100x.

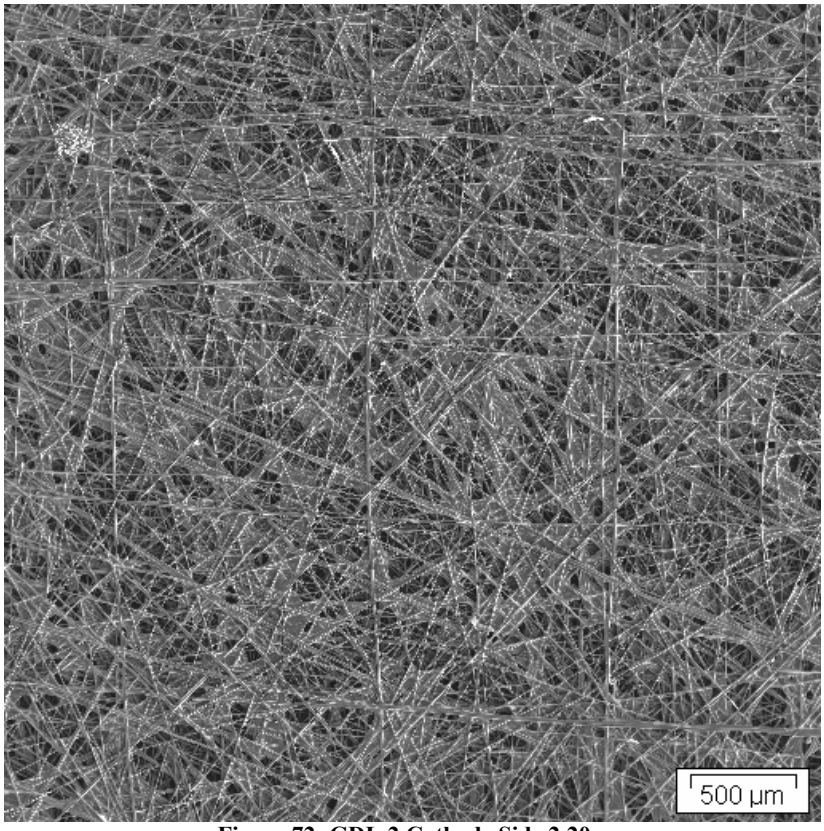

Figure 72: GDL 2 Cathode Side 2 20x.

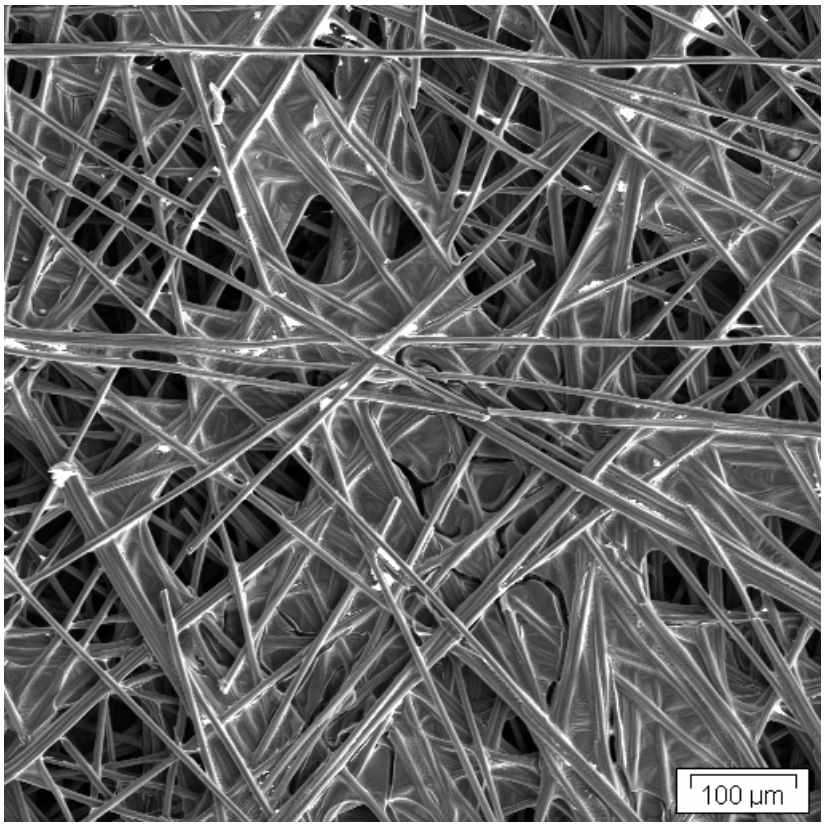

Figure 73: GDL 2 Cathode Side 2 100x.

Transverse Sections of Carbon Fiber Papers

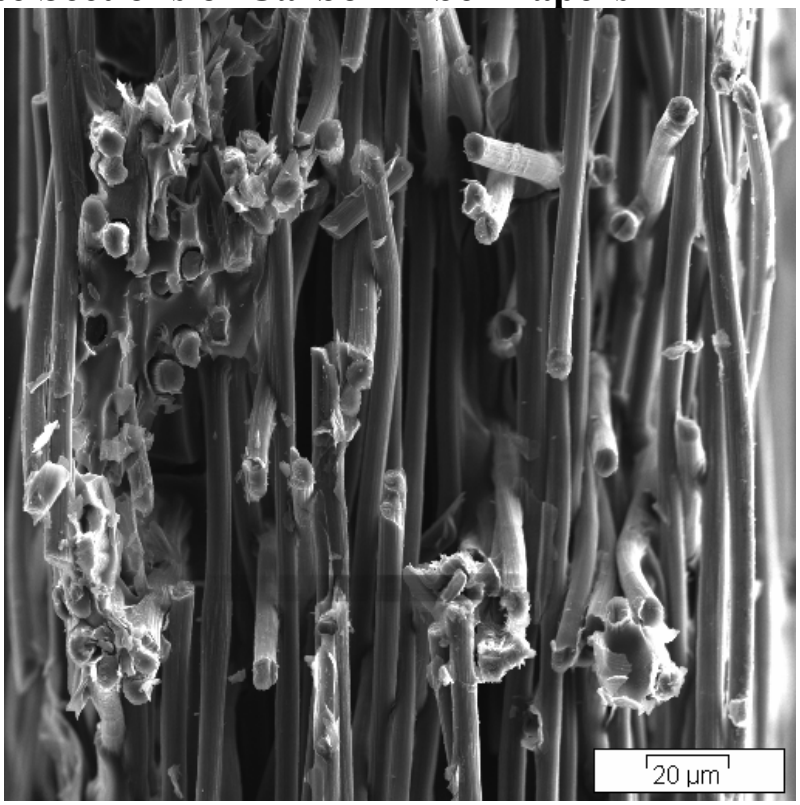

Figure 74: GDL 1 Anode Point 1 400x.

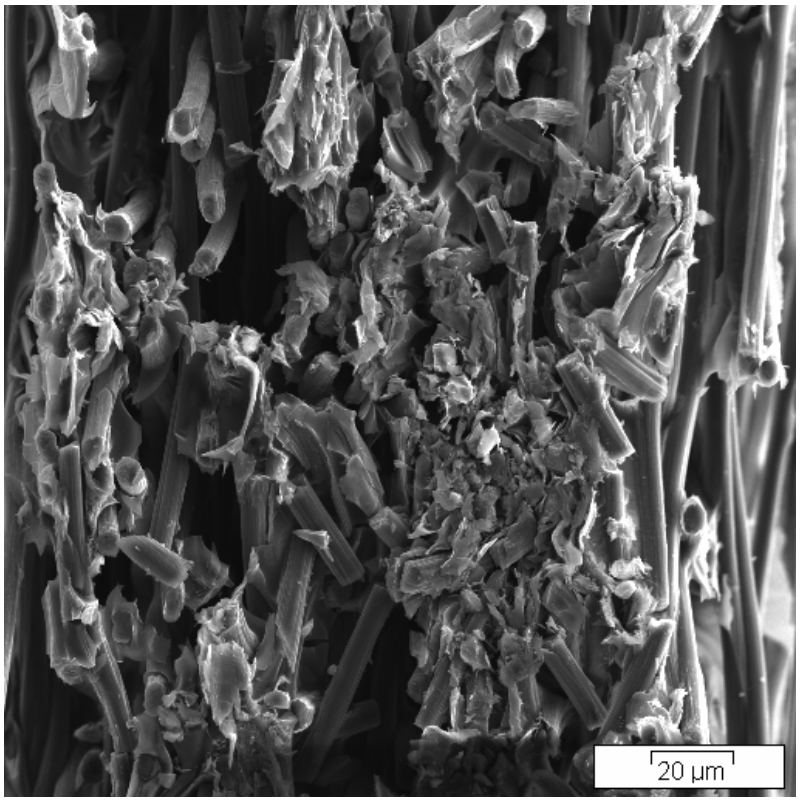

Figure 75: GDL 1 Anode Point 2 400x.

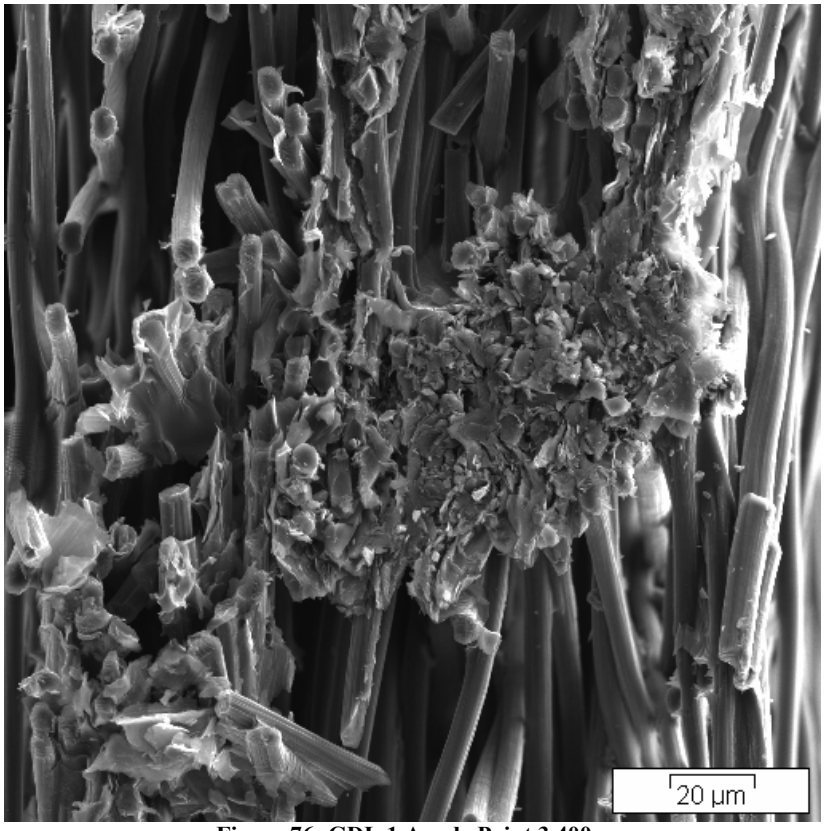

Figure 76: GDL 1 Anode Point 3 400x.

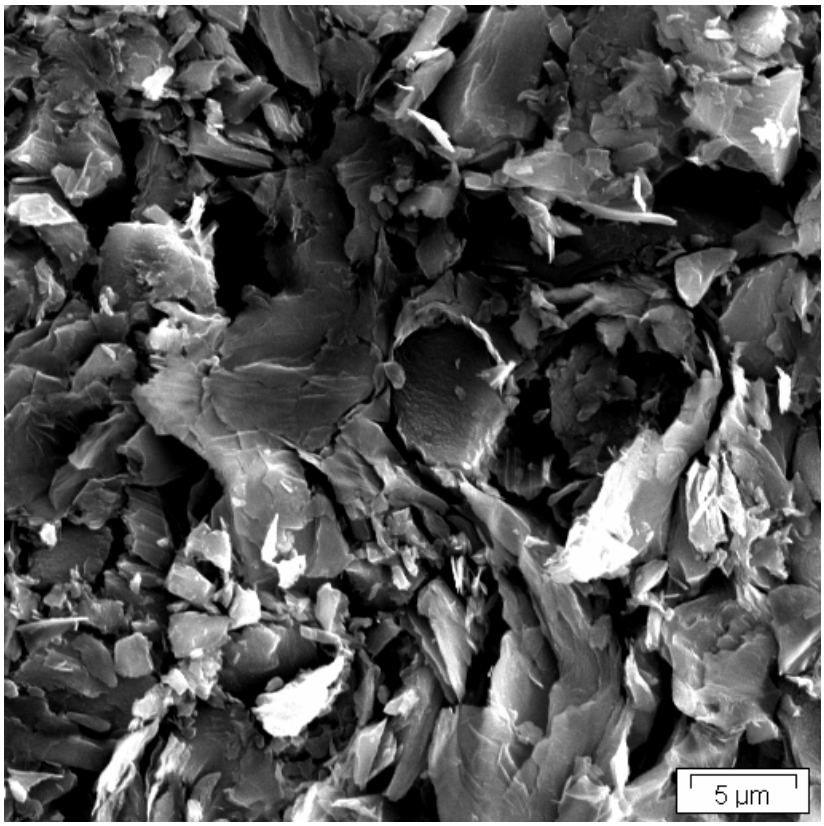

Figure 77: GDL 1 Anode Matrix Material 2000x.

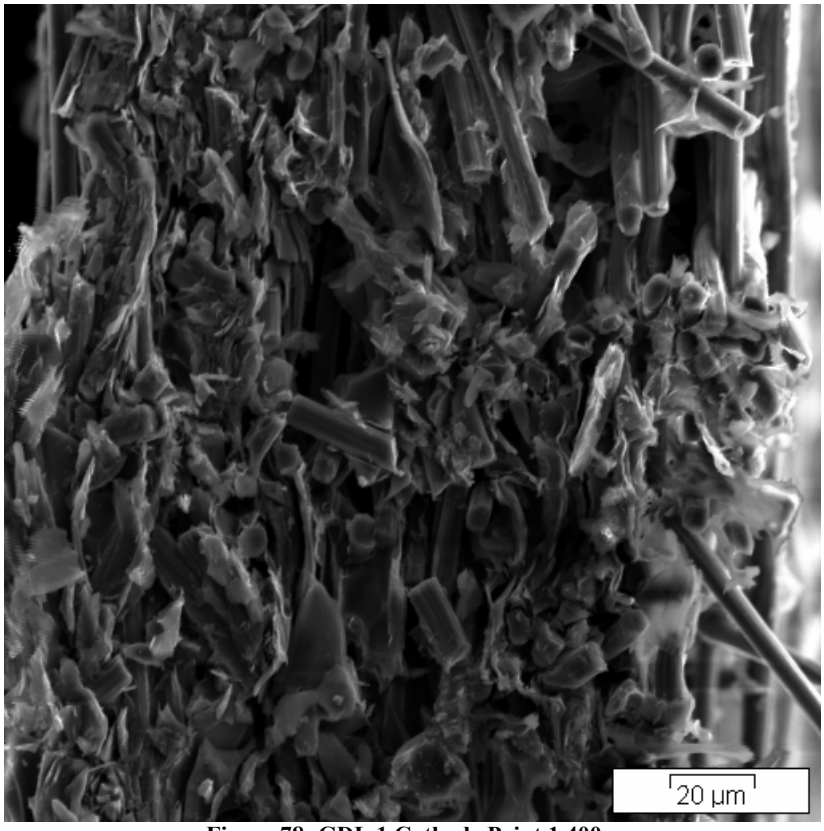

Figure 78: GDL 1 Cathode Point 1 400x.

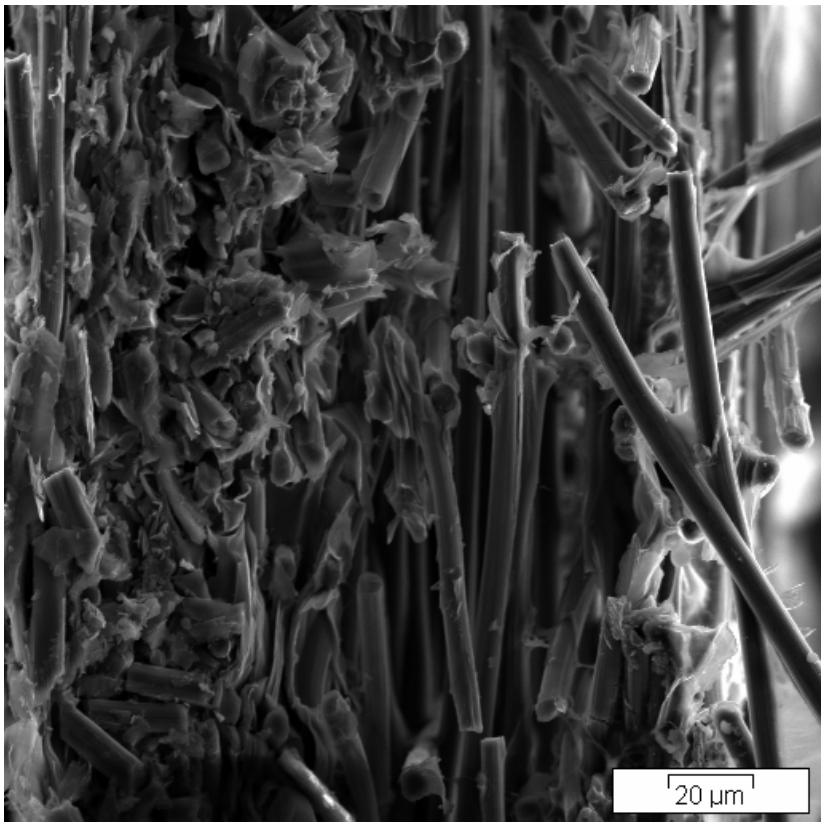

Figure 79: GDL 1 Cathode Point 2 400x.

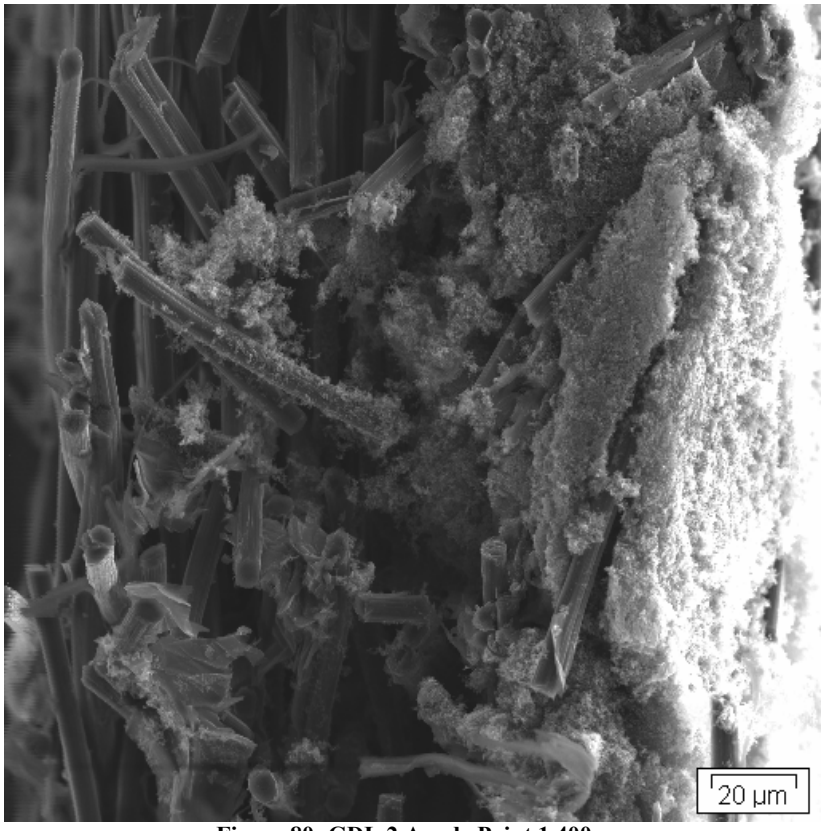

Figure 80: GDL 2 Anode Point 1 400x.

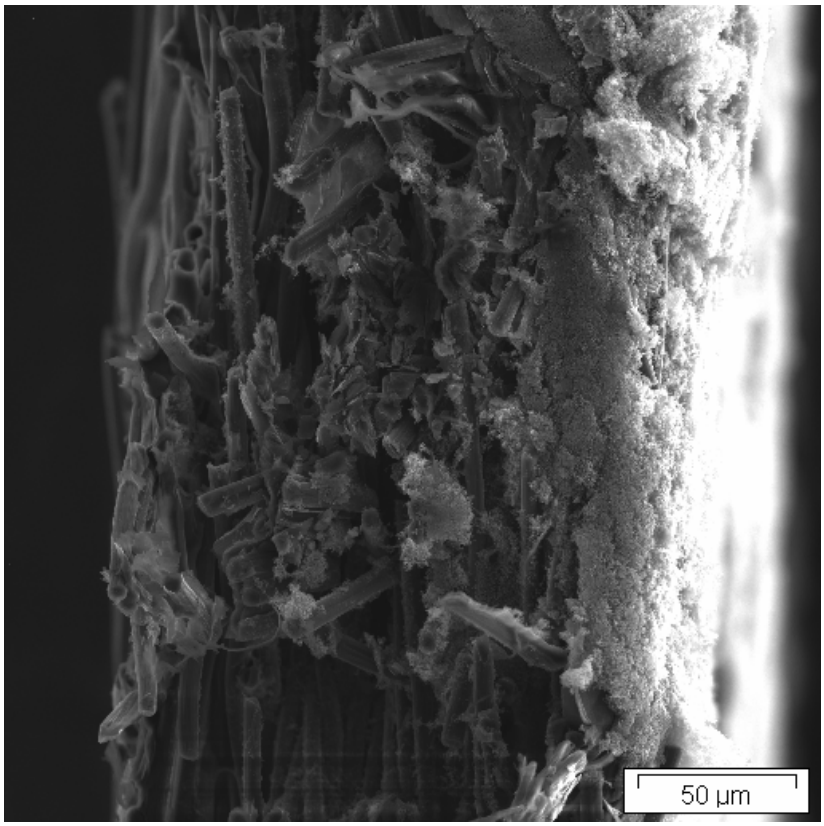

Figure 81: GDL 2 Anode Point 2 300x.

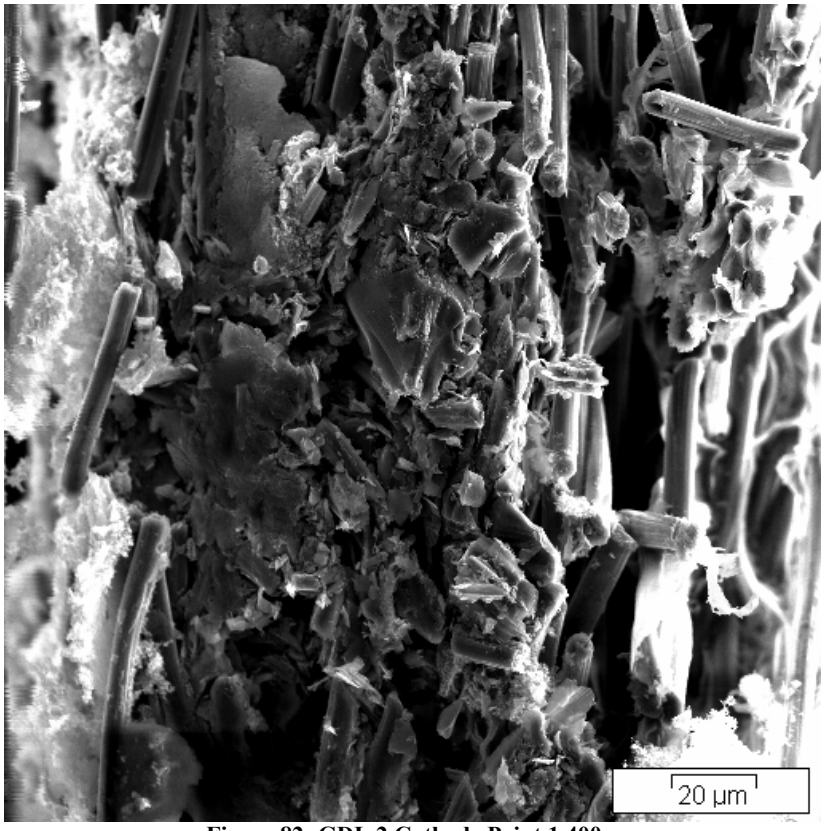

Figure 82: GDL 2 Cathode Point 1 400x.

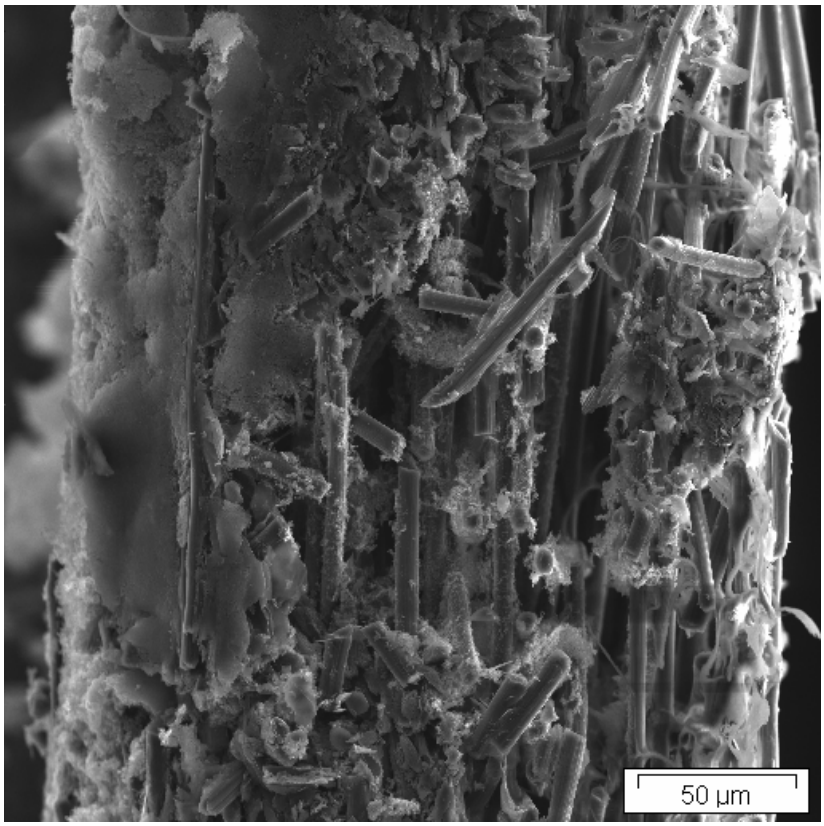

Figure 83: GDL 2 Cathode Point 2 300x.

Appendix C

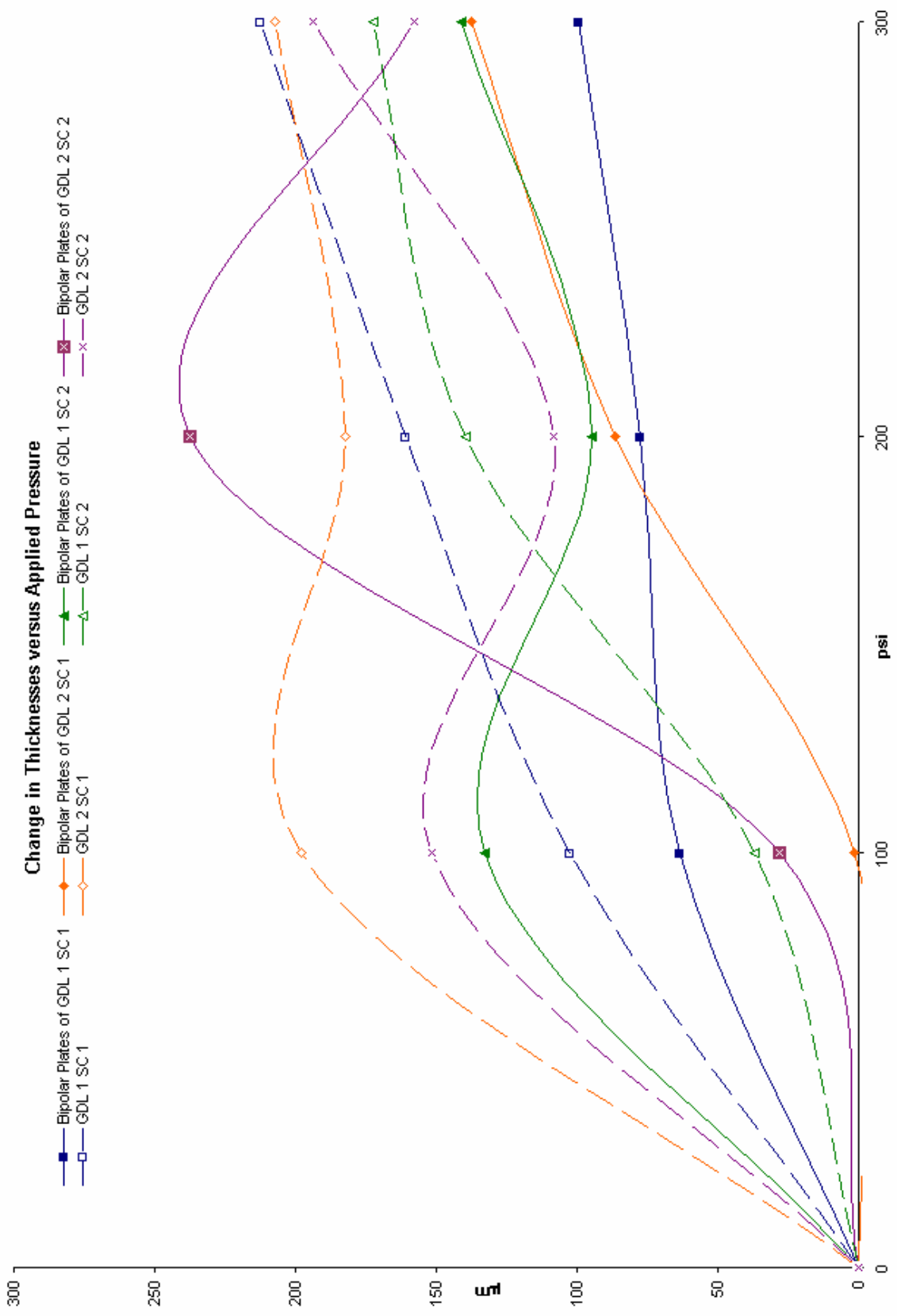

Figure 84: Impingement Data Chart 30.

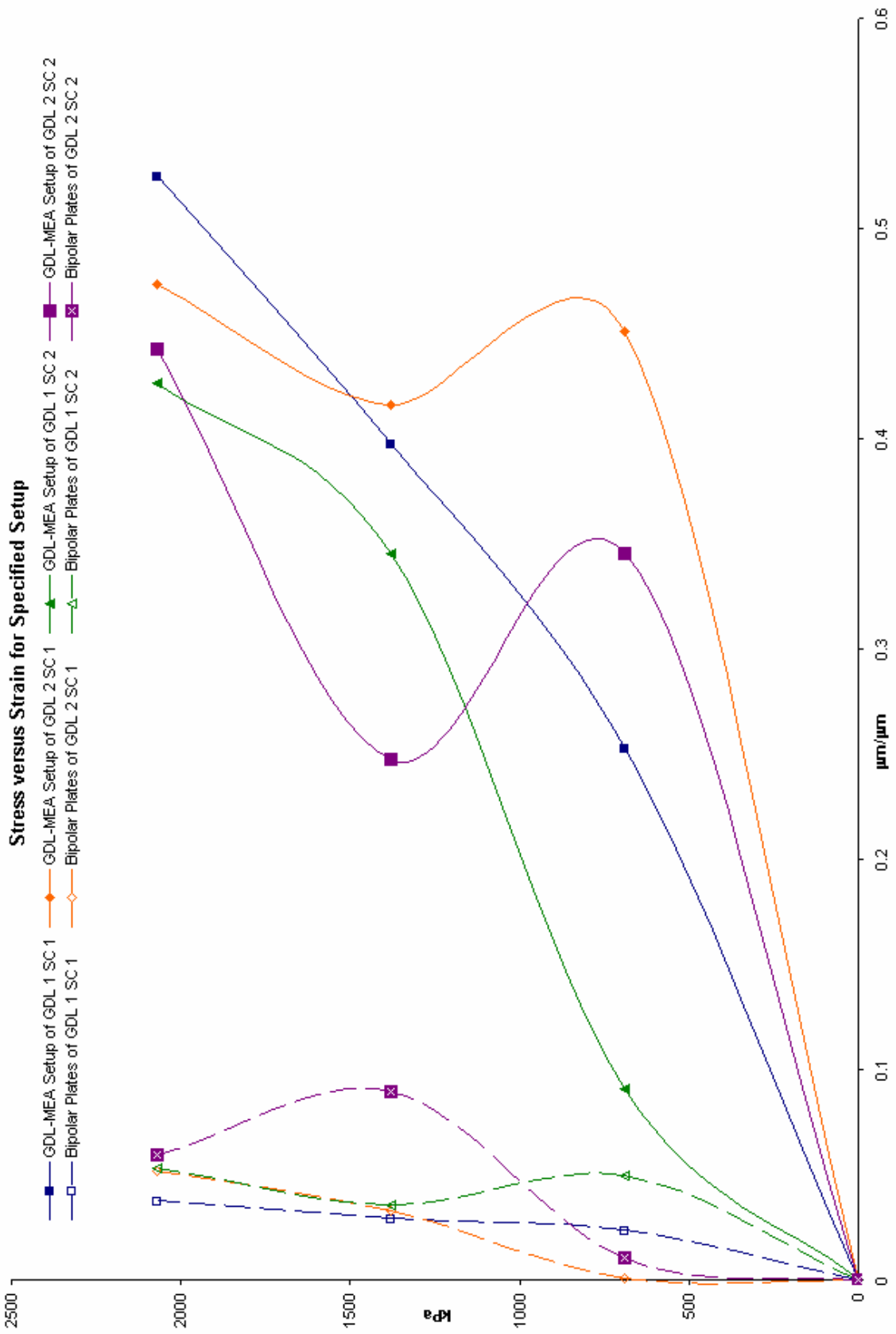

Figure 85: Impingement Data Curve 31.

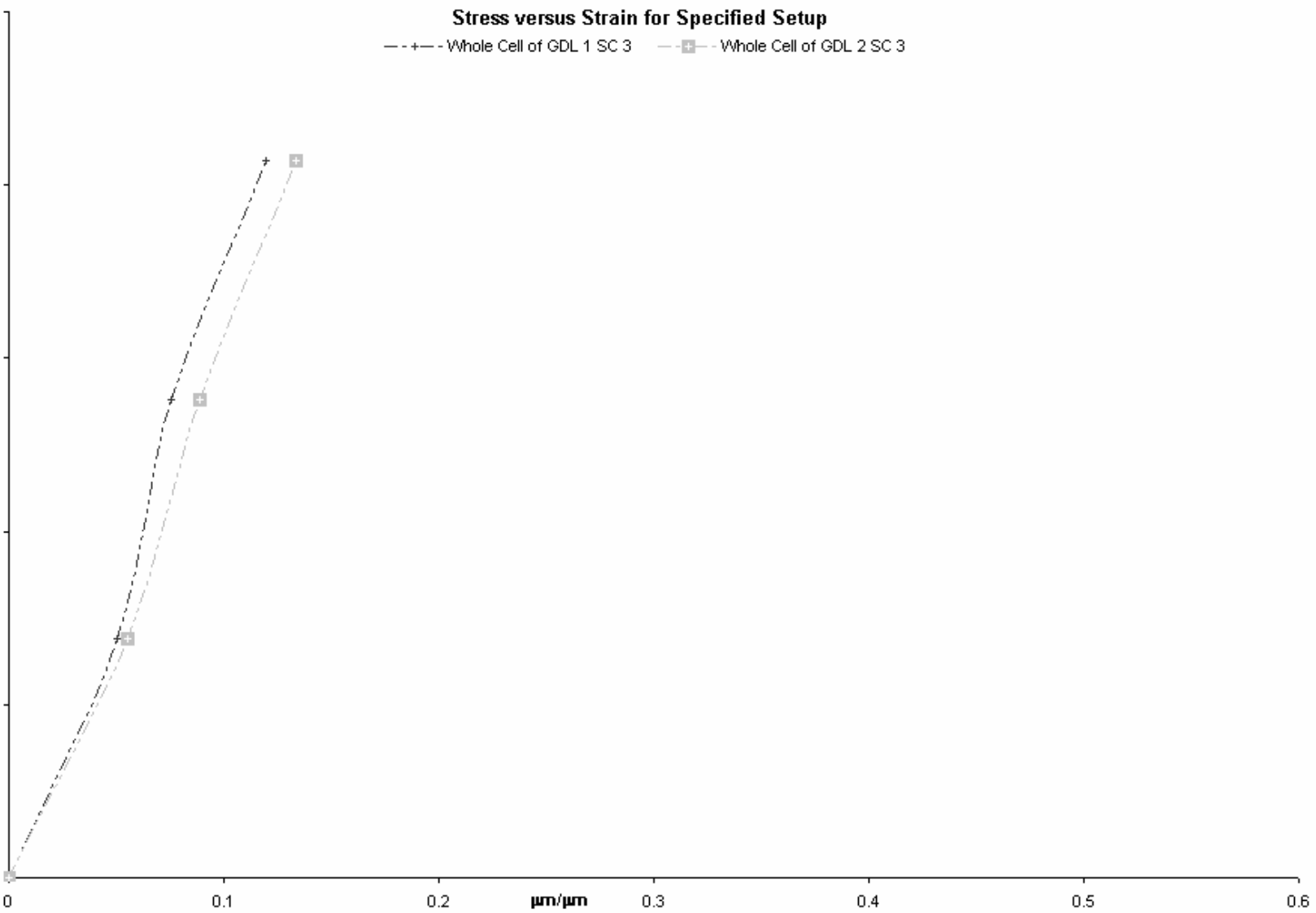

Figure 86: Impingement Data Chart 32.

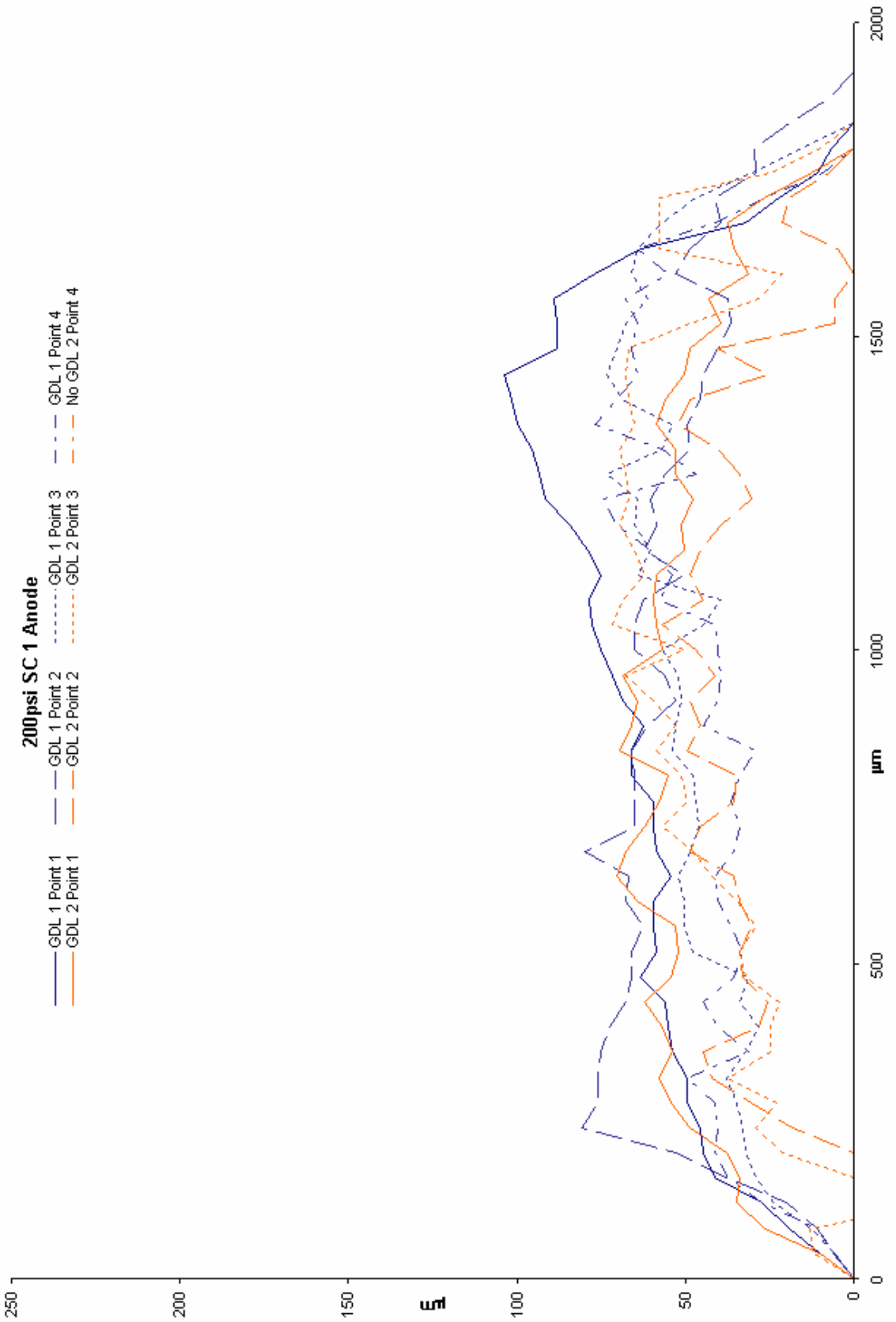

Figure 87: Impingement Data Chart 33.

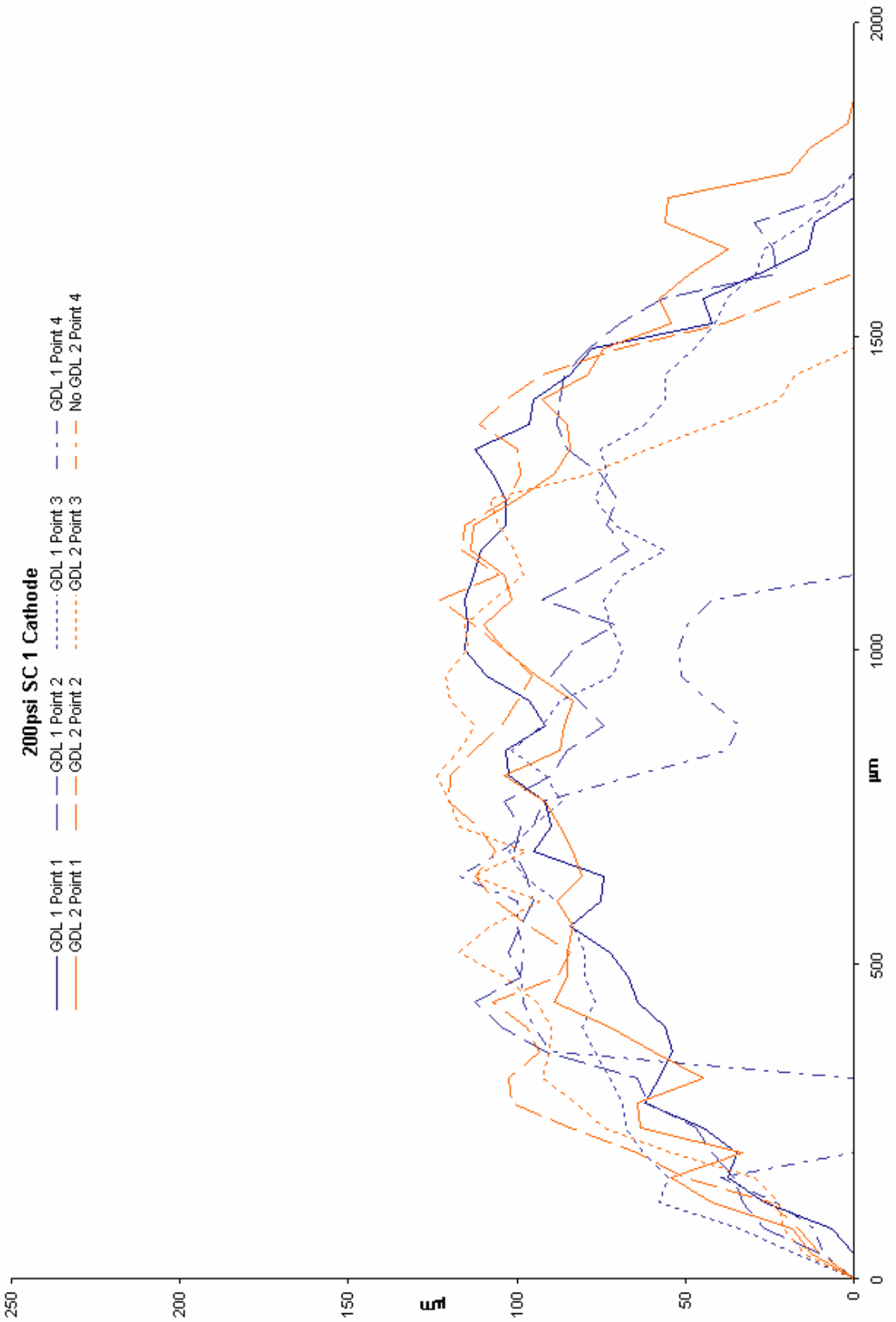

Figure 88: Impingement Data Chart 34.

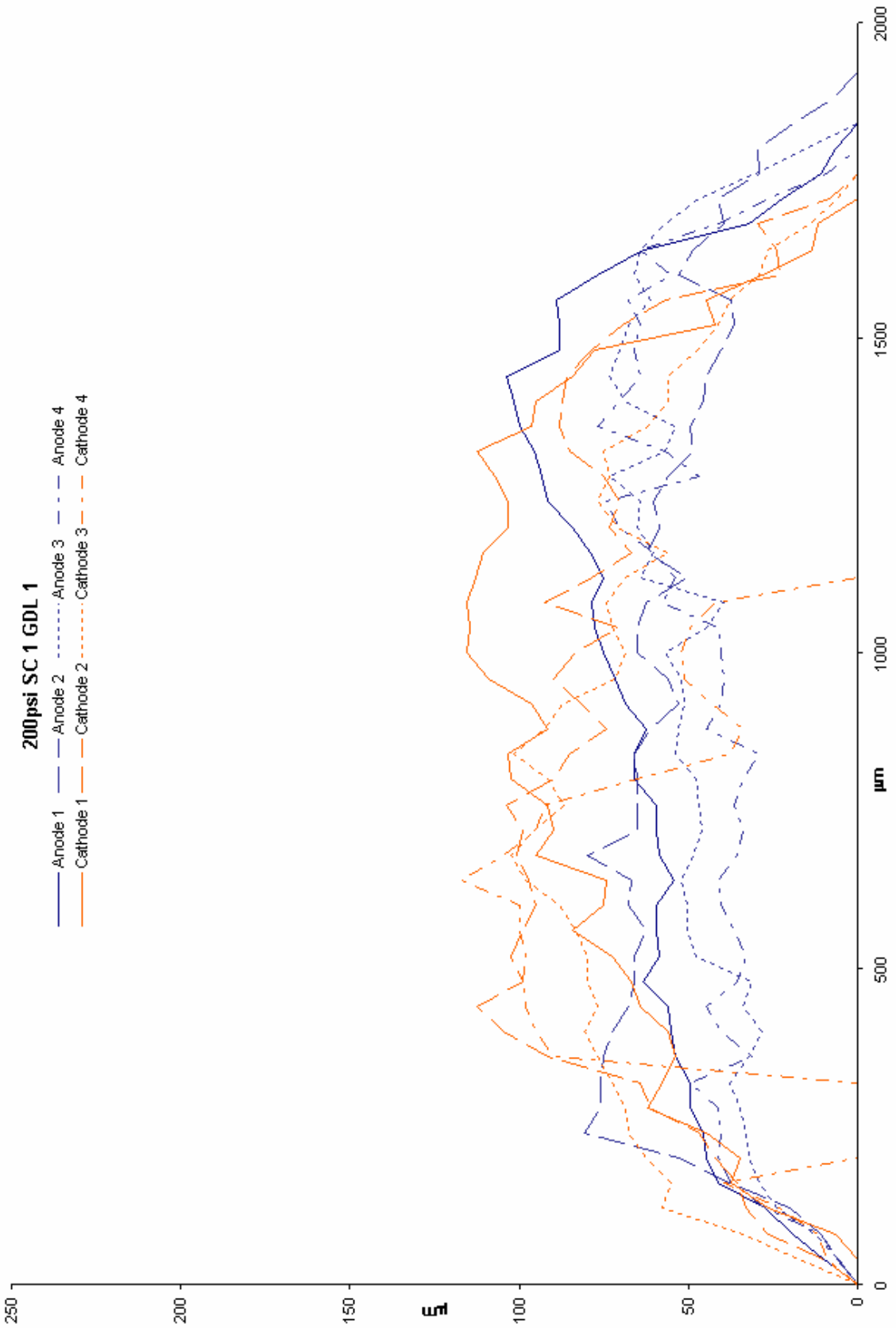

Figure 89: Impingement Data Chart 35.

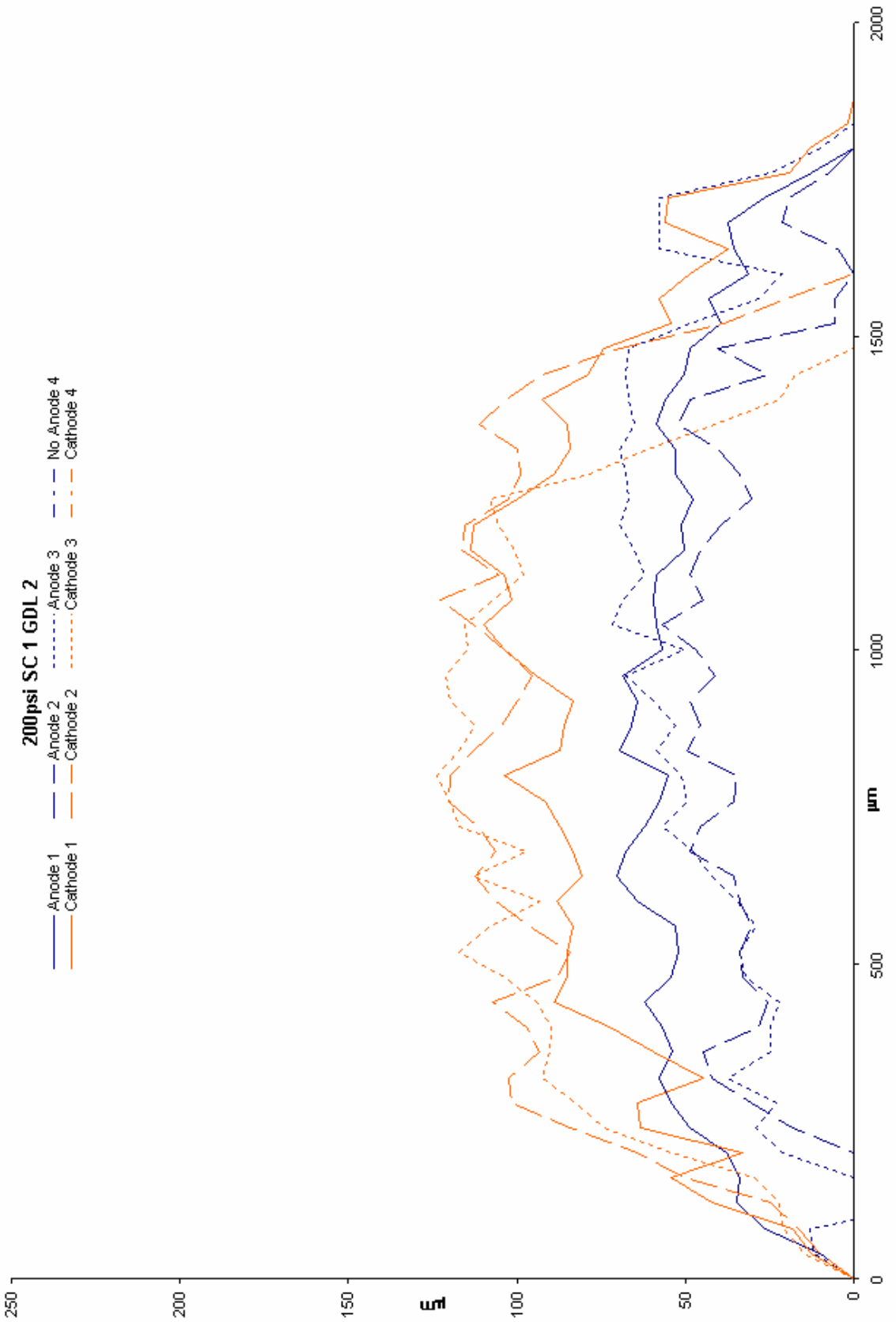

Figure 90: Impingement Data Chart 36.

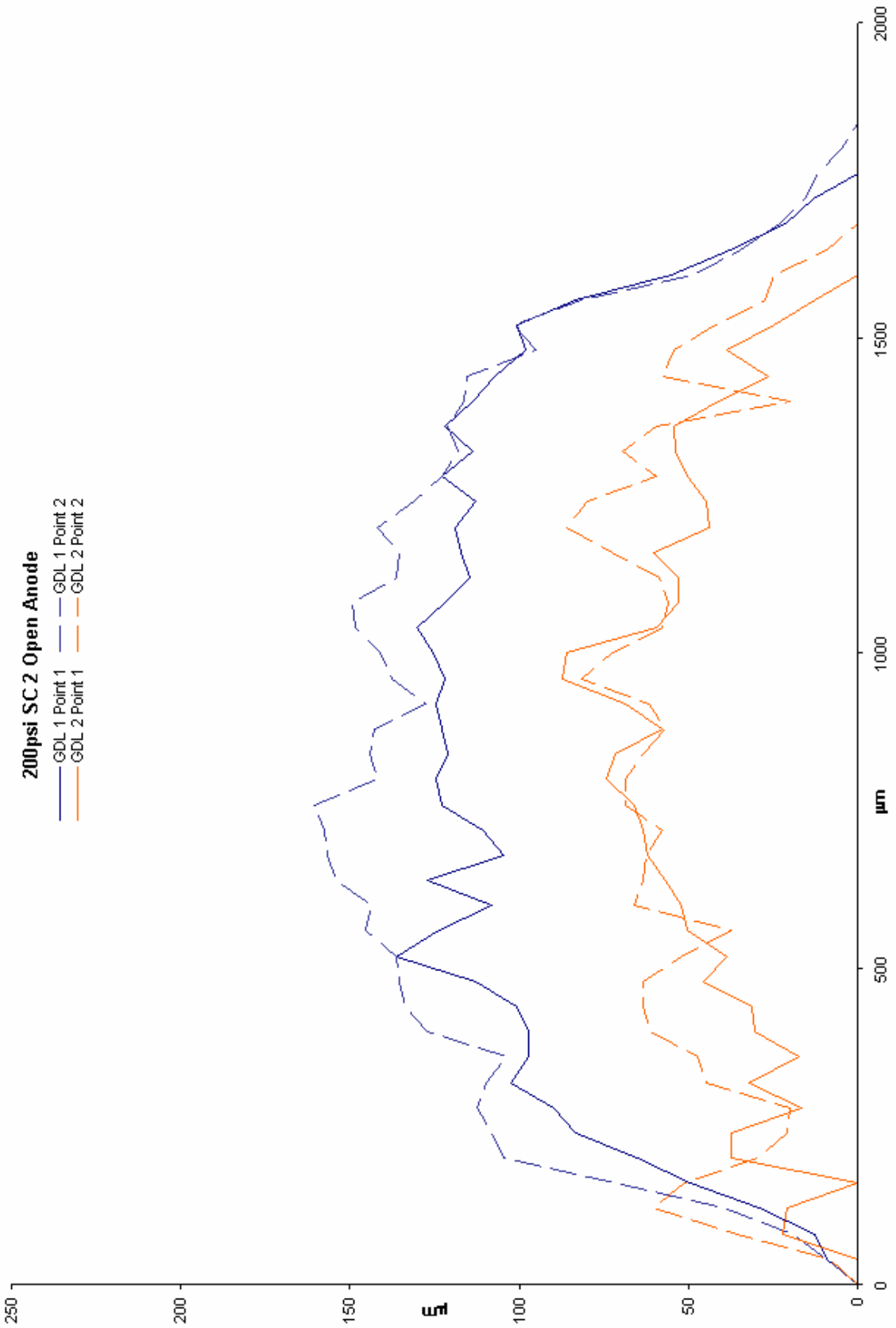

Figure 91: Impingement Data Chart 37.

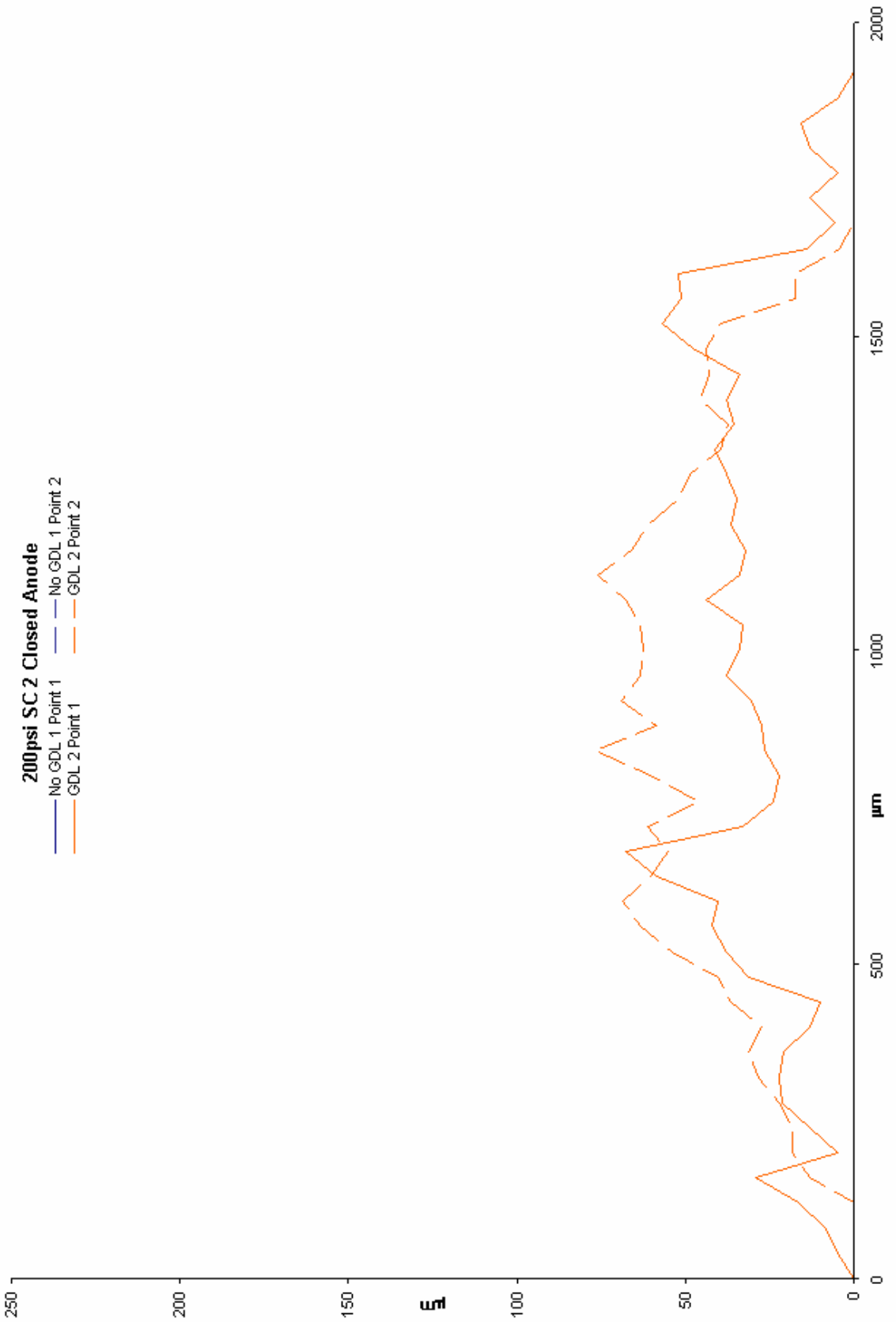

Figure 92: Impingement Data Chart 38.

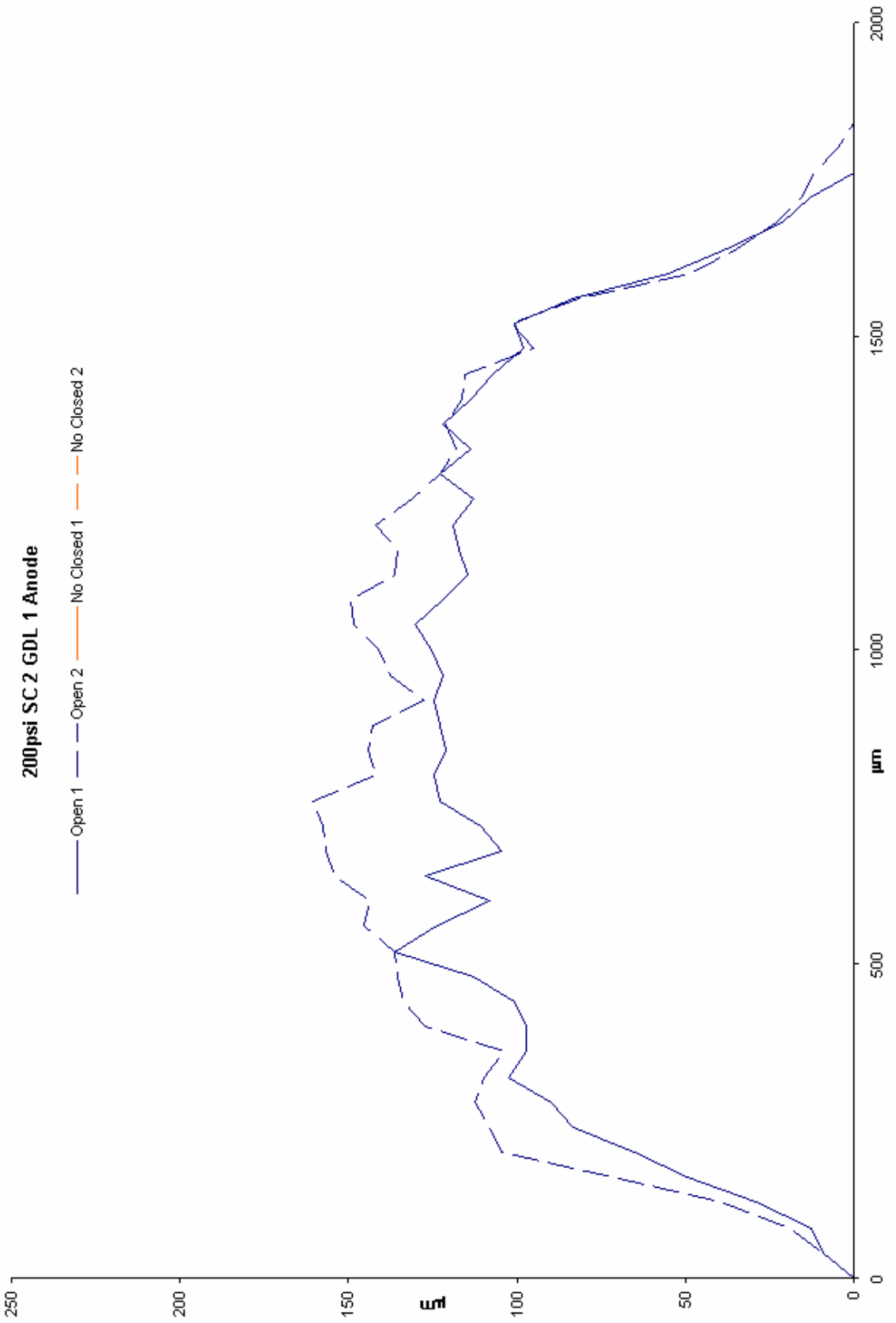

Figure 92: Impingement Data Chart 39.

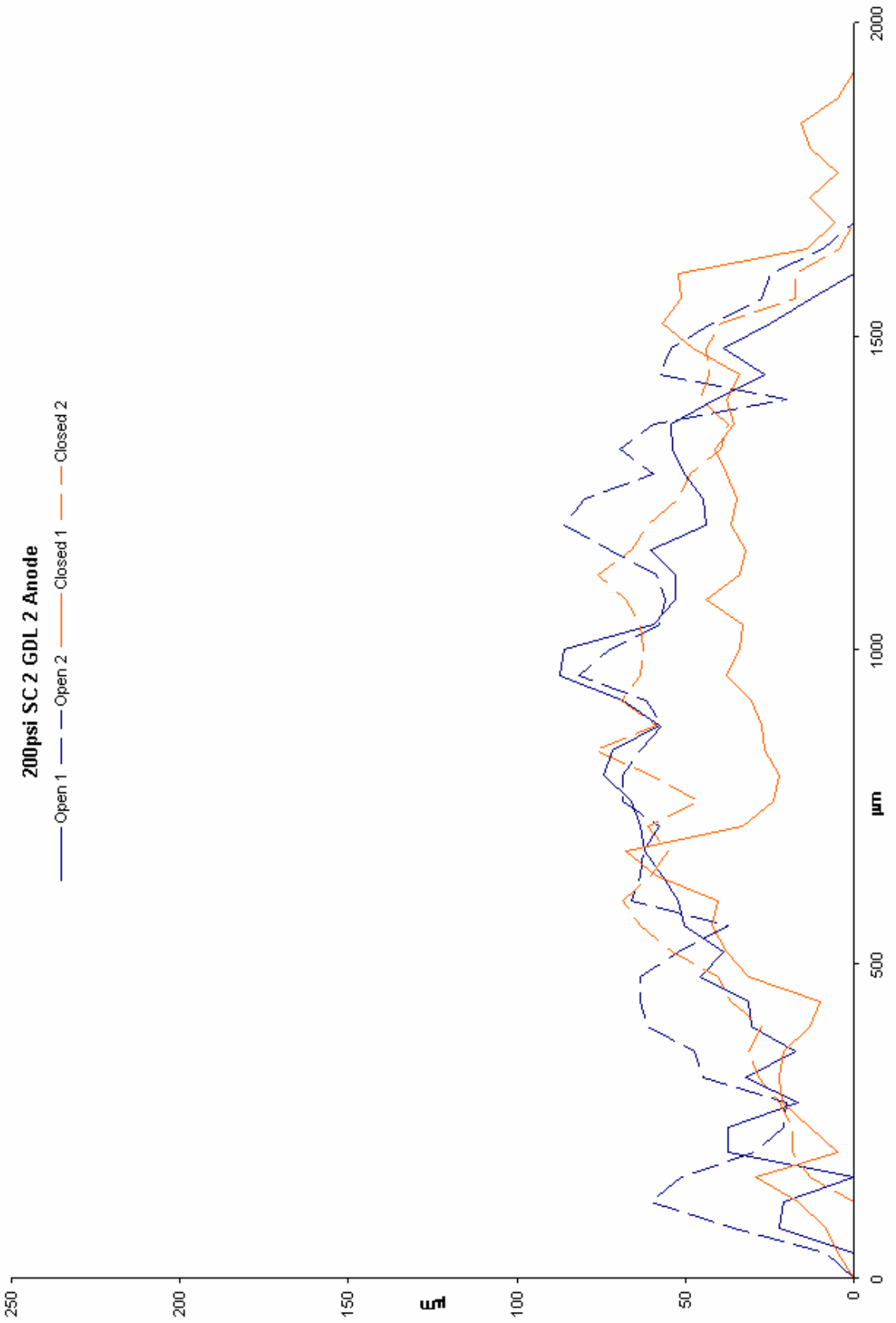

Figure 93: Impingement Data Chart 40.

References

1. Bockris J. Reddy A. Modern Electrochemistry 1: Ionics 2nd Ed. New York: Plenum Press. 1998.
2. Bruce P. ed. Solid State Electrochemistry. Great Britain: University Press. 1995.
3. Buckley J. Edie D. eds. Carbon – Carbon Materials and Composites. Park Ridge: Noyes Publications. 1993. Online book.
4. Carrette L. Friedrich K. Stimming U. "Fuel Cells – Fundamentals and Applications." Fuel Cells. Vol #1 pg 5 – 33. (27 Jun 2001). Online journal.
5. Chung D. Carbon Fiber Composites. Boston: Butterworth-Heinemann. 1994. Online book.
6. Crow D. Principles and Applications of Electrochemistry 2nd Ed. Great Britain: J. W. Arrowsmith Ltd. 1979.
7. Hertzberg R. Deformation and Fracture Mechanics of Engineering Materials 4th Ed. New York: John Wiley & Sons. 1996.
8. Hoogers G. ed. Fuel Cell Technology Handbook. Boca Raton: CRC Press. 2003.
9. Kinoshita K. Carbon: Electrochemical and Physiochemical Properties. New York: John Wiley & Sons. 1998.
10. Koryta J. Ions, Electrodes, and Membranes. New York: John Wiley & Sons Ltd. 1982.
11. Larminie J. Dicks A. Fuel Cell Systems Explained. Great Britain: John Wiley & Sons. 2000.
12. Peebles L. Carbon Fibers Formation, Structure, and Properties. Boca Raton: CRC Press, Inc. 1995.
13. Richerson D. Modern Ceramic Engineering: Properties, Processing, and Use in Design 2nd Ed. New York: Marcell Dekker, Inc. 1992.
14. Thomas C. ed. Essentials of Carbon-Carbon Composites. Great Britain: Royal Society of Chemistry. 1993.
15. Tomsic J. Dictionary of Materials and Testing 2nd Ed. Warrendale: Society of Automotive Engineers, Inc. 2000.
16. Vasiliev V. Morozov E. Mechanics and Analysis of Composite Materials. Great Britain: Elsevier Science Ltd. 2001.
17. Young G. ed. Fuel Cells. New York: Reinhold Publishing Corporation. 1960.
18. Zhang X. Shen Z. "Carbon Fiber Paper for Fuel Cell Electrode." Fuel. Vol 81 pg 2199 – 2201. 2002. Online journal.
19. Zumdahl S. Chemical Principles 3rd Ed. Boston: Houghton Mifflin Co. 1998.